MIXED TOPOGRAPHIC AND SHALLOW BATHYMETRIC MAPPING VIA MULTI-STOP SINGLE PHOTOELECTRON LASER RANGING

By

KRISTOFER Y. SHRESTHA

A DISSERTATION PRESENTED TO THE GRADUATE SCHOOL
OF THE UNIVERSITY OF FLORIDA IN PARTIAL FULFILLMENT
OF THE REQUIREMENTS FOR THE DEGREE OF
DOCTOR OF PHILOSOPHY

UNIVERSITY OF FLORIDA

2010

To my mother, for instilling in me a determination bordering on stubbornness

ACKNOWLEDGMENTS

This research was made possible only with the valued advice and support of my family, friends, fellow students and professors. I would like to thank Dr. Clint Slatton for directing me into this line of work and for exhibiting continual patience in the face of very difficult obstacles. Dr. Slatton continues to serve as my inspiration to work even harder in times of tough circumstance. I would also like to thank Dr. Bill Carter for pushing me to find the alternative solution in times where I genuinely believed success to be an impossibility. His expertise and guidance in the field of low-signal laser ranging have been critical to this work.

Next, I would like to express my appreciation for the support of my fellow Geosensing students. This small piece of text is probably all that will ever document the selfless field work of these students on my behalf, so I need to take this opportunity to thank Tristan Cossio, Juan Fernandez, Pang-Wei Liu, Kitiipat Kampa, Pravesh Kumari, Tolee Matamas, Mike Starek, Abhinav Singhania, and Bidiya Yadav. I will not forget the freezing cold nights in Citra, the struggles at Lake Wauburg, or the countless other times that they aided me in CATS testing. I would also like to thank the staff at the CE Structures Lab / Plant Science Research for use of the their facilities, William Gavert / Jacob Hwang for their support in diagnosing electronics issues, and Sidney Schofield for his invaluable help in preparing the system for airborne operation.

Finally, I would like to express my deep gratitude to my father, Ramesh, and my mother, Chew-Ying, for providing me with opportunities that few children get to have, and to my sister, Veena, for all her love. Finally, I would like to thank Cynthia Gillikin for her patience and support through this long process.

TABLE OF CONTENTS

LIST OF TABLES

LIST OF FIGURES

Abstract of Dissertation Presented to the Graduate School
of the University of Florida in Partial Fulfillment of the
Requirements for the Degree of Doctor of Philosophy

MIXED TOPOGRAPHIC AND SHALLOW BATHYMETRIC MAPPING VIA
MULTI-STOP SINGLE PHOTOELECTRON LASER RANGING

By

Kristofer Y. Shrestha

August 2010

Chair: Kirk Hatfield
Major: Civil Engineering

Airborne laser swath mapping (ALSM) systems collect thousands of range measurements per second, enabling efficient high-resolution surface mapping. Low signal-to-noise ratio (LSNR) detection techniques allow for implementation of light detection and ranging (LIDAR) instrumentation on platforms with prohibitive power, size, and weight restrictions. The viability of single-wavelength photon counting techniques applied to mixed target detection and shallow-water bathymetry has not been previously investigated in detail.

The system design process for constructing a LSNR LIDAR system is described, with emphasis on component selection as related to theoretical performance. Cost-effective microchip lasers are now commercially available that produce sub-nanosecond pulse widths and stable peak energies (>1 μJ at 10 kHz). In order to detect backscattered laser radiation at low power levels, detector elements must be capable of single photon sensitivity; a high gain (10^5), fast response (sub-250 ps rise time) detector is therefore central to photon counting operation. Micro-channel plate photomultiplier tubes (MCP-PMTs) are capable of attaining these specifications with simultaneous two-dimensional detection over an array.

The University of Florida's prototype LSNR LIDAR sensor – the Coastal Area Tactical-mapping System (CATS) – was constructed with these major components in mind. The instrument is designed to operate in a fixed-wing aircraft flying 600 m above ground level, producing 3 μJ output pulses at 8 kHz to allow for 20 cm spatial resolution by scanning a 10x10 array of laser beamlets. Ground-based field testing results yield 10 cm range accuracy and small-scale feature identification at variable scan settings.

Experimental data is presented establishing the ability to record multiple returns from the same laser pulse. Evaluation of system dead time shows that the minimum separation distance required to discriminate multiple scattering objects is 15 cm, indicating the possibility of seamless topographic / bathymetric mapping with no gap at the waterline. Data collected during tests display vertical structure in shallow water areas based on fixed threshold crossings at very low signal levels. A major concern for the binary detection strategy is dark / atmospheric / crosstalk noise producing false-positive measurements. Potential causes of image ghosting are described, and data collection / processing solutions based on local density estimation are explored. LIDAR depth estimates from airborne profiles are compared to on-site measurements, and near-shore submerged feature identification is presented.

Analysis of CATS data confirms simulation estimates of decimeter-scale spatial resolution for hybrid topographic and shallow bathymetric mapping. Dark noise production and atmospheric scattering in daylight operation at maximum signal amplification does not significantly impede feature identification procedures. In order to combat the high variability in dynamic range, modifications to the detector structure may be necessary to reduce anomalous effects.

CHAPTER 1
INTRODUCTION

Introduction to Remote Sensing

Our surrounding environment is a diverse collection of refractive and reflective media. The interaction of light with matter is of special interest for remote sensing, a branch of science concerned with the acquisition of information about an object or phenomenon without direct physical contact. Information about positions, sizes, and interrelationships between objects can be concisely conveyed through imagery. Because humans possess a high level of proficiency in deriving information from such images, we experience little difficulty in interpreting even those scenes that are visually complex. In fact, it is only when we attempt to replicate these capabilities using computer programs that we realize how powerful our abilities are to derive this kind of intricate information [1].

Photogrammetry and LIDAR

Photogrammetry is one method of obtaining reliable information about the environment through processes of recording, measuring, and interpreting images and patterns of electromagnetic radiant energy and other phenomena [2]. Recent advances in technology have given rise to parallel methods of remote sensing, one example being light detection and ranging (LIDAR). This acronym is commonly used to describe the intersection of an inertial navigation system (INS), a light amplification through stimulated emission of radiation (laser) device, and a global positioning system (GPS) [3]. Precise timing of transmitted and received light is the focus of LIDAR instruments. Given that light travels at a known velocity, time-of-flight observations allow for

measurement of propagation distances. Detailed geo-spatial information is obtained by the combination of these observations and enhanced navigation tools.

Advantages of LIDAR

LIDAR offers advantages over photogrammetry which has caused airborne LIDAR to emerge as an attractive alternative to traditional methods of large-scale geospatial data capture [3]. Photogrammetric methods for digital terrain model (DTM) generation can be labor intensive and time consuming. LIDAR allows for fast surveying of remote areas because each data coordinate is individually geo-referenced; aerial triangulation or orthorectification of data is not required. Because of a dependence on solar illumination, aerial photography systems are limited to daytime operation and are affected by weather. LIDAR systems can operate at night and through a variety of weather conditions. In addition, LIDAR offers a distinct improvement over photogrammetry in the collection of elevation data in heavily forested areas. Dense canopy cover generally prevents retrieval of accurate terrain information by photogrammetric sensors [3]. Airborne laser mapping sensors, on the other hand, can be used to acquire 3D discrete point measurements of canopy structure and the underlying surface topography with sub-meter resolution [4]. We will extend this concept to airborne bathymetry in later chapters.

Applications of LIDAR

A typical airborne LIDAR sensor provides tens to hundreds of thousands of range measurements per second, which can be used to construct a high resolution map of an area. Airborne laser swath mapping (ALSM) is a proven method for obtaining high quality three-dimensional mapping data [5], [6]. The impact of this technology is easily seen from a militaristic viewpoint; improved target detection capabilities create

advantages for surveillance and reconnaissance of enemy operations. The contributions are not necessarily limited to warfare, however—airborne mapping can provide valuable information about rural or inaccessible areas, record observations of delicate or highly sensitive terrain, and aid in hazardous environment mapping.

Improving Image Fidelity

LIDAR Point Clouds

The basic visualization of LIDAR data is a projection of three dimensional points into a "point cloud." Features within the point cloud can be identified at a number of scales. For example, large-scale topographic undulations can be mapped, while at the same time small-scale road edges, roof outlines and tree locations can be pinpointed. Analysis of post-processed data has yielded automatic methods for feature segmentation and target identification [7], [8], [9]. Point density within the cloud determines the spatial resolution at which slowly varying continuous features are monitored and sharply varying discrete features are identified. The ability to plot more points per square meter results in higher image fidelity.

Existing Methods for Improving Feature Detection

It is possible to merge LIDAR points with data from another type of sensor to improve feature detection capabilities. For example, it has been shown that the fusion of small-footprint LIDAR and multi-spectral data can help to estimate plot-level volume and biomass in deciduous forests [10]. Gaps in point cloud data over water can be filled with information from sonar, but usually at coarse intervals. It has also been shown that the addition of high-resolution hyperspectral imagery aids in classification of benthic LIDAR waveforms [11]. Data fusion and weighting of feature detection algorithms continues to be a growing area of study in the field of remote sensing.

Preferably, however, a single sensor would be able to provide all the necessary information and eliminate the need for data fusion considerations. For LIDAR alone, increasing the laser pulse repetition rate decreases the time between illuminations of ground footprints; thus subject to a static scan pattern (not dependent on laser rate) and a consistent platform velocity, spacing between ground points is reduced and horizontal resolution is improved. This approach eventually results in having more than one laser pulse in flight at the same time, which can cause difficulties when the range to the surface changes rapidly and unpredictably, as is often the case in mountainous terrain or urban settings. The two-way travel time of the laser pulses set a maximum pulse rate of 250 kHz at an average flying height of 600 m. If, however, a single laser beam is split into an array of elements and transmitted at once, the spatial resolution is limited by the number of array elements and the capability of the receiver to process returns over the array simultaneously. A moderate laser pulse rate (<10 kHz) can then theoretically provide contiguous coverage of the surface of the terrain at decimeter-scale resolution on a single pass of an airborne LIDAR system [9].

Existing Methods for Improving Data Quality

Low-level signal classification is often difficult in LIDAR systems given practical considerations for variations in surface reflectivity; diffuse reflections of laser light are not always easily detectable. Characterization of system noise is important for discrimination of true events, meaning that noise components should be kept to a minimum where possible. Superior contrast between signal and noise may generally be achieved by transmitting higher laser pulse energy. Providing large outgoing pulse energy increases the probability that weak light-matter interactions will produce a detectable response. Lasers operating at high energy can be paired with a variety of

detector components and still be able to “see” the desired target regardless of faint backscattered radiation or low amplification. An assumption for this case is that the paired photodetector can operate at an acceptable dynamic range; i.e., be able to detect the faintest and strongest measured signals with equal accuracy. Another assumption is that noise returns do not increase at the same rate as signal returns given a more energetic pulse; otherwise false events would obscure the desired response.

The LSNR Mapping Approach

Problems with High Energy / High Pulse Rate Designs

Meter-scale spatial resolution in airborne scanning laser altimeter systems can be achieved by employing high energy / high pulse rate designs. Currently deployed ALSM implementations are designed to produce a high signal-to-noise ratio (SNR); typical specifications at standard altitudes of 500 to 1500 m are transmitted energy of 100 μJ per pulse and laser repetition frequency of 50 to 170 kHz [12]. These systems are capable of generating thousands of return photons incident on the receiver for each outgoing laser pulse. High SNR ensures that a system will be able to separate true return signals from sources of spurious noise events such as atmospheric scattering and detector dark noise, but may still contain erroneous points associated with multi-path (sequential reflections from different surfaces prior to returning to the sensor).

High energy, high pulse rate systems are not always practically desirable because of the size, complexity and cost of hardware. For example, attempting to integrate a high energy LIDAR design into a small unmanned aerial vehicle (UAV) platform is problematic. This type of platform operates on a fixed power budget, so introducing a heavy payload impedes flight operations. Utilizing a high energy laser can shorten

mission duration by draining battery life; high power lasers require complex electronics and sophisticated cooling systems. Bulky equipment is unsuitable for scalability with low-power applications. UAVs are often intended for potentially “disposable” functions, and the loss of an expensive laser mapping unit can be prohibitive. Operation in populated areas also restricts maximum laser power and sensor altitude due to eye safety requirements. Designs based on a high energy requirement per illuminated area limit the size of the footprint, resulting in less than contiguous coverage of the terrain.

Motivations for a LSNR LIDAR System

Practical requirements such as those mentioned above have motivated alternate methods to detect weak light-matter interactions. Current commercial terrain mapping systems provide time-of-flight measurements for multiple reflections from each laser shot. The event timer used to determine the time of flight of the recorded returns can use various discriminator designs to analyze the photodetector voltage response, including threshold, center of gravity, maximum, zero crossing of the second derivative, and/or constant fraction [13]. Classically a constant fraction discriminator has been used to obtain first / last responses related to separate reflecting objects in complex waveforms [14]. This approach may limit the minimum distance between two distinguishable objects in the surveyed scene because lasers of relatively high energy (greater than 100 μJ per pulse) generally have pulse widths of a few nanoseconds or longer.

It has been suggested that a conventional single element detector approach operating under high SNR does not make the most efficient use of available laser photons [15]. This idea has shown merit in low-SNR (LSNR) LIDAR experiments on the Multi-kiloHertz Micro-Laser Altimeter (MMLA), developed at the NASA Goddard Space

Flight Center under the Instrument Incubator Program [16]. It is estimated that the surface sampling rate can be increased by over three orders of magnitude for a given laser power/telescope aperture product by emitting the available photons in a high frequency train of low energy pulses, as opposed to a low frequency train of high energy pulses, and by employing photon-counting detector arrays with multi-channel timing receivers [16].

In theory, surface mapping efficiency can be significantly improved by using a LSNR LIDAR paradigm based on lower energy and shorter pulse lasers [15]. Small-footprint LIDAR are intended to illuminate only a few surfaces within the footprint, yielding distinct return pulses corresponding to separate reflecting objects [17]. LSNR concept systems such as the Remote Ultra-Low Light Imaging system developed at the Los Alamos National Laboratory [18], the Jigsaw sensor created under the DARPA program at the Massachusetts Institute of Technology Lincoln Laboratory [19], and a second generation 3D imaging and polarimetric LIDAR developed by Sigma Space Corporation [20] have established LSNR LIDAR as an effective approach to terrain mapping.

Though these ventures have shown the promise of the LSNR technique, they still represent a limited number in comparison to the many HSNR parallels. In the context of modern technology advancements, this has left significant gray areas in a comprehensive understanding of LSNR signal analysis. Simulation can be a powerful tool in this case, as a modeling capability can analyze performance as a function of system specifications and mission environment. Current mathematical models support

the idea that a single-wavelength LSNR mapping instrument can provide hybrid topographic and bathymetric mapping in shallow coastal areas [21].

Research Aims

The goal of this work is to move beyond simulation and explore the viability of topographic and shallow bathymetric mapping via a single wavelength (532 nm), low altitude (500 m), low energy (3 μJ), short pulse (500 ps) laser ranging system. A prototype LSNR system has been developed by the University of Florida for this purpose, and detailed analysis of sensor data is shown here. In Chapter 2 of this work, the fundamentals of selecting an appropriate illumination source and photodetector are presented. In Chapter 3, the specifics related to the University of Florida's LSNR prototype design are listed. In Chapter 4, analyses of static experiments yield performance metrics associated with LSNR feature detection. In Chapter 5, analyses of airborne experiments explore the sensor's ability to provide shallow water bathymetry in a variety of water types. Chapter 6 presents conclusions about the viability of the technique and suggestions for improvement.

CHAPTER 2
LSNR COMPONENTS

Commercial Sector Activities and Scientific Impact

COTS Market and Costs

Prior to 1995, laser altimetry was generally conducted using custom-designed sensors operated by research groups or built by commercial survey firms to exploit niche markets. The majority of these efforts were based on single prototype designs, limiting their ability to create and service a broad, sustainable, sector-wide demand for the technology. Since 1995, however, a commercial off-the-shelf (COTS) instrument market has developed which has removed many of the constraints for incorporating laser altimetry into operations [22]. These conditions have allowed for new types of lasers and photodetectors to become available without prohibitive cost to a variety of research organizations.

LSNR Concept Systems

The Satellite Laser Ranging Station (SLR2000) [15] was one of the earliest experimental platforms to demonstrate LSNR potential. The SLR2000 employed passively Q-switched microlasers with output energies of 135 μJ and rates below 5 kHz to achieve mm-level ranging precision at satellite altitudes of 20,000 km. Using a sub-nanosecond pulse width, a laser beam divergence of 10 arcseconds, and a receive aperture of 76 cm resulted in a signal strength of less than one photoelectron per laser shot. Target discrimination was made possible by utilizing a range receiver able to identify and extract single photon laser echoes from solar background noise through Poisson statistical analysis of the received photon distribution. The Post Detection

Poisson Filtering (PDPF) technique has been extended to the MMLA sensor for signal extraction in an airborne scanning altimeter capable of daylight operations [23].

The Remote Ultra-Low Light Imaging (RULLI) system also responds to individual photons using a low power pulsed laser and Pulse Absolute Timing (PAT) channels for time discrimination in the front-end electronics [18]. Three dimensional imaging was accomplished with a vertical resolution of 5 cm. The detector is made up of a micro-channel-plate (MCP) image intensifier front end with high gain for photon counting and a wire-would cross delay line (CDL) anode. A stack of three MCPs allow for electronic gain up to 10^7. Each PAT channel is designed around a number of internal circuits in a hybrid electronics module called a time interval meter (TIM). This includes a constant fraction discriminator (CFD) front end, a dual interpolator stage, and a ten bit time to digital converter. This allows for detection of signals with amplitude variation of 40 dB while maintaining a time walk of less than 100 ps.

The Jigsaw system uses arrays of single photon sensitivity avalanche photodiodes (APD) for integration onto various surveillance platforms [19]. The sensor was also tested in an indoor environment for use in surface reconnaissance experiments. An example of raw data from the Jigsaw system is shown in Fig. 2-1. The “noisy” nature of these images illustrates the challenges associated with LSNR LIDAR detection, as most of the points originate from avalanche photodiode dark counts. These challenges can be met through post-processing techniques, as researchers have created a suite of novel algorithms to perform noise reduction, ground-plane identification, detector response deconvolution, and illumination pattern renormalization [24]. Results of these efforts are shown in Fig. 2-2.

Selection of a well-paired illumination source and photodetector can improve SNR so that data processing presents less of an obstacle. The following sections describe how to select components with appropriate characteristics to maximize photon-counting performance. A brief history of lasers is presented to introduce microchip laser design parameters. We will then transition into classic detector pairings and the photon counting concept.

Overview of Lasers

Quantum Dynamics Fundamentals

Lasing is made possible by the creation of population inversion in a group of atoms or molecules. This phenomenon is best introduced with quantum mechanics. In the simplest form, a group of N atoms can exist in two basic states or energy levels: E_1, the ground state, and E_2, the excited state, with $\mathrm{E}_2 > \mathrm{E}_1$. The number of atoms in the ground and excited states are given by N_1 and N_2, respectively. The total number of atoms in the system is N, where $\mathrm{N} = \mathrm{N}_1 + \mathrm{N}_2$. The energy difference between the two states is given by $\Delta \mathrm{E} = \mathrm{E}_2 - \mathrm{E}_1$. This difference determines the characteristic frequency f_{12} of light which will interact with the atoms, following the expression [25],

$$\Delta \mathrm{E} = h \cdot f_{12}, \tag{2-1}$$

where *h* is Planck's constant (6.6261×10^{-34} J·s). Thermodynamics shows us that for a system in thermal equilibrium, the ratio of a number of atoms in each state is given by the Boltzmann distribution,

$$\frac{\mathrm{N}_2}{\mathrm{N}_1} = e^{-\frac{(E_2 - E_1)}{kT}}, \tag{2-2}$$

where T is the thermodynamic temperature of the group of atoms and k is Boltzmann's constant (1.3807×10^{-23} J·K^{-1}). The ratio of the atom populations at room temperature (T ~ 300 K) for an energy difference delta E that corresponds to visible light (f ~ 500 Terahertz) can then be calculated; Δ E = 2.07 eV, and kT = 0.026 eV. Since this ratio forms the argument for the negative exponential and Δ E >> kT, it follows that the ratio $\frac{N_2}{N_1}$ is very small; i.e., there are very few atoms in the excited state for a system in thermal equilibrium. The Boltzmann distribution dictates that in this case, even at infinite temperature, the population N_2 will not exceed N_1. Achieving population inversion thus requires pushing the system into a non-equilibrated state.

Methods of achieving population inversion are based on precise manipulation of optical properties. Light can interact with a system of atoms in the following three ways: absorption, spontaneous emission, and stimulated emission. In the first, photons of frequency f_{12} may be absorbed by ground state atoms, causing them to transition to the higher energy level. The probability of occurrence is proportional to incident light intensity and N_1. In the second, atoms in the excited state may also relax back to the ground state, and in the process release photons of frequency f_{21}; this is called spontaneous emission.

The final interaction, stimulated emission, is the most important for the optical amplification process which makes lasing possible. An atom in the excited state may be perturbed by the passage of a photon with frequency f_{21} (exactly corresponding to the energy gap Δ E), causing a transition to the ground state and the emission of a second photon at the same frequency. Albert Einstein showed that the base probability of a

photon causing stimulated emission in a single atom is equal to the probability of a photon being absorbed by an atom in the ground state [26]. Consequently, when the number of atoms in the excited and ground states are equal, the rate of absorption is equal to the rate of stimulated emission for a given radiation density.

Coherence

The stimulated transition process is the sum of two separate processes. The lower energy level contains atoms that are stimulated by the applied signal to make upward transitions, while the upper energy level contains atoms that are stimulated by the applied signal to make downward transitions. The net flow of atoms is always from the higher population level to the lower population level. If the lower level is more populated, the signal is attenuated. If the higher level is more populated, the signal is amplified. The stimulated transition process results from a resonant response of the atomic wave function, or of the atomic charge cloud in each individual atom, to the applied signal. The internal induced oscillation or dipole response that is produced in each atom is stimulated by the applied signal [27].

Atomic oscillations follow the driving optical signal in full coherence, meaning that they follow the same amplitude and phase. An amplifying laser medium produces a linear reproduction of the input signal – and correspondingly any amplitude or phase modulation present in the signal – except that a) the output signal is increased in magnitude; b) the signal modulation may be decreased in bandwidth because of the finite bandwidth of the atomic response; and c) the signal generally has a small amount of spontaneous emission noise added to it [27].

Three- and Four-Level Laser Models

It has been shown that the ideal two-level system is not enough to achieve population inversion. A more realistic approach considers three levels: E_1, E_2, and E_3, with $E_3 < E_2 < E_1$. Initially the majority of the atoms are in the ground state E_1. These atoms transition to E_3 by absorbing radiation at a frequency $f_{13} = \frac{1}{h \cdot (E_3 - E_1)}$. This is often referred to as the "pump transition." For a medium suitable for laser operation, it is required that these excited atoms quickly decay to E_2. Spontaneous emission may occur as a result, but in practice the E_3 to E_2 transition is radiationless; energy is transferred to vibrational motion of the host material surrounding the atoms without the generation of a photon.

Correspondingly, an atom may decay from E_2 to E_1 and release a photon of frequency f_{12}. This is the intended laser transition, and it is achieved by ensuring that the lifetime of the transition t_{21} is much longer than the lifetime of the transition t_{32}; often called a favorable lifetime ratio. Over time, the population N_3 in this case will become very small, and a population of excited atoms will accumulate at E_2. Optical amplification then can be achieved with the population inversion $N_2 > N_1$.

The three-level framework was the basis for many early lasers, including the first ruby laser as implemented by Theodore Maiman in 1960 [28]. In the context of modern lasers the three-level system is inefficient because the medium must be very strongly pumped in order to achieve inversion. Most lasers now operate via a four-level process.

A four-level laser energy level diagram is shown in Fig. 2-3. The fast, radiationless transition R_a from the pump band to E_3 – the upper laser level – results in the population N_4 being rapidly depleted. The same is true for atoms at the lower laser level E_2; they will make a quick transition to the ground state E_1 via R_b. The laser medium is selected such that the transition of atoms from E_3 to E_2 is the intended laser transition. A four-level system is much more efficient than a three-level, however, because any significant population accumulating at E_3 produces a population inversion with respect to the negligible population N_2. Optical amplification is thus possible for the frequency f_{32}.

Optical Resonators

Now that laser operation has been introduced from the quantum perspective, the device characteristics behind resonance or amplification can be described. While at Columbia University in 1959, graduate student Gordon Gould introduced the idea of the open resonator [29] and its potential applications. An optical cavity or resonator is an arrangement of mirrors that forms a standing light wave. The cavity surrounds the gain medium and provides feedback for laser light. Multiple reflections of light from mirrors at either end of the resonance chamber produce standing waves for certain resonance frequencies.

Certain patterns of standing waves are sustained via constructive interference, called the modes of the laser, while others are suppressed due to destructive interference. There are two types of modes. Longitudinal modes refer to the wavelengths of the wave reinforced by constructive interference after many reflections from the cavity mirrors, and transverse modes refer to the electromagnetic field pattern

measured in a plane perpendicular to the beam propagation direction. The most basic transverse mode is the Gaussian energy distribution.

The simplest optical cavity is created by two facing plane (flat) mirrors, commonly called the Fabry-Pérot arrangement. The difficulty in using flat mirrors comes in the alignment; even a few arc-seconds of error can cause the intracavity beam to leak out the sides of the cavity. This problem becomes much less significant when dealing with short mirror separation distances (L < 1 cm) [30] however, allowing for their use in microchip and semiconductor lasers.

Q-Switching

Pulsed lasers are particularly important for laser ranging applications, as the pulse duration and energy are of prime relevance to a system's timing and detection capabilities. "Q-switching" is a technique for increasing the energy of short pulses by modulating the intracavity losses and the "Q-factor" of the laser resonator. Q-factor, or quality factor, is a term borrowed from electronic circuits (for example, describing inductive-capacitive elements in the context of a continuously operating oscillator). The term was adapted for optical resonators to measure the strength of the oscillation damping in the optical cavity [31]. Manipulation of the Q-factor allows for generation of "giant" pulses [32], referring to a large amount of energy output in a short amount of time.

Q-switching is achieved by putting a variable attenuator inside the laser's optical resonator. When the attenuator is functioning, light which leaves the gain medium does not return, and lasing cannot begin. The attenuation in the cavity corresponds to a decrease in the Q-factor of the optical resonator. A high Q-factor corresponds to low

resonator losses per round trip, and vice versa. The variable attenuator is commonly called a "Q-switch" when used for this purpose.

Initially the laser medium is pumped while the Q-switch is set to prevent feedback of light into the gain medium (producing an optical resonator with low Q). This produces a population inversion, but laser operation cannot yet occur since there is no feedback from the resonator. Since the rate of stimulated emission is dependent on the amount of light entering the medium, the amount of energy stored in the gain medium increases as the medium is pumped. Due to losses from spontaneous emission and other processes, after a certain time the stored energy will reach some maximum level; the medium is said to be "gain saturated." At this point, the Q-switch device is quickly changed from low to high Q, allowing feedback and the process of optical amplification by stimulated emission to begin. Because of the large amount of energy already stored in the gain medium, the intensity of light in the laser resonator builds up very quickly; this also causes the energy stored in the medium to be depleted almost as quickly. The net result is a short pulse of light output from the laser, known as a giant pulse, which may have very high peak intensity.

The Q-factor can be reduced via both active and passive methods; the output of an energy pulse in this manner is called Q-switching. For active Q-switching, losses in the cavity are typically modulated via acousto- or electro-optics. A pulse is formed after an electrical trigger signal is received. With a sufficiently fast trigger, pulse widths on the order of the cavity round-trip transit time can be achieved [33]. These are often referred to as "cavity-dumped lasers." Mechanical switches such as a Lummer-Gehrcke plate in conjunction with a rotating prism also been used [34], but are less

common. The idea of using a saturable absorber to achieve passive Q-switching (PQS) was presented in 1965 by Szabo and Stein [35], along with derivation of rate equations and numerical analysis.

Microchip Laser Advancements

To obtain closed-form solutions for key laser parameters such as output energy and pulsewidth in modern lasers, one can solve the three coupled differential equations which describe PQS. Optimization of the amplification system depends on the combination of characteristics related to the laser gain medium, absorber medium, and pump intensity. The Lagrange multiplier technique introduced by Degnan [36] can determine the optimum mirror reflectivites and unsaturated absorber transmissions as a function of two dimensionless variables: z, the ratio of the logarithmic round-trip small signal gain to the dissipative optical loss; and α, the saturation energy density of the amplifying medium divided by the saturation energy of the absorber. These theoretical calculations were shown to be in agreement with experimental results, and independent optimization theories for rapid PQS lasers were subsequently formed [37].

The early part of the 21st century gave rise to significant advancements in continuous wave (CW) pumped PQS microchip lasers, with emphasis on large-amplitude repetitive behavior of PQS in solid-state devices [38]. Numerical and analytic solutions were presented to describe the gain medium as an ideal four-level atom and the saturable absorber as a two level atomic system. The region of interest in this case is where the saturation intensity for the saturable absorber is larger than that for the gain, and when both decay rates are fast. Numerical bifurcation studies and asymptotic analysis show [38] that PQS is possible if these restrictions are met, and microchip laser design equations can be derived that are valid whenever the gain is depleted and the

saturable absorber is bleached. When applied to pulsing in a microchip laser with a neodymium-doped yttrium aluminum garnet (Nd:YAG) gain medium and chromium-doped yttrium aluminum garnet (Cr^{4+}:YAG) saturable absorber, theoretical results were shown to be within 10% of the experimental values [38].

Studies such as these formed the theoretical basis for microchip laser development. For the PQS Nd:YAG / Cr^{4+}:YAG laser specifically, it has been shown that the maximum repetition rate is correlated with the pulse width; specifically, it decreases as the pulse width gets shorter [39]. If the absorption cross section of the saturable absorber is large in comparison to the gain cross section of the gain medium, relatively few stimulated photons are necessary to rapidly bleach the absorber. Absorption in Cr^{4+}:YAG occurs at 808 nm – the wavelength used to pump the Nd:YAG gain medium – which can cause partial bleaching of absorption. This results in a smaller absorption coefficient at the oscillating wavelength and a smaller effective Cr^{4+}:YAG fill factor (the normalized fraction of the filled cavity) for the laser.

The fraction of the laser cavity filled with Nd:YAG decreases as the Cr^{4+} fill factor increases, meaning that the Nd:YAG must be more highly inverted to reach threshold. More heat is thus deposited per unit length of active material. The gain cross section decreases and a greater inversion is required as a result of the increase in thermal energy. Positive feedback occurs, leading to a well-defined threshold for thermal runaway [39]. The maximum pulse repetition rate is correlated with the Cr^{4+} fill factor, meaning that the maximum repetition rate and pulse width are also correlated. Experimental results for several SPMCL microchip lasers used in the Zayhowski study are shown in Fig. 2-4.

Beam Quality Measures

A common measure of beam quality is the M^2 factor. This is defined as the product of the beam radius (measured at the beam waist) and the beam divergence half-angle (measured in the far field) divided by $\frac{\lambda}{\pi}$, according to ISO Standard 11146 [40],

$$\theta = \frac{M^2 \lambda}{\pi w_0} . \tag{2-3}$$

A laser beam is often said to be diffraction-limited by M^2 times, as a diffraction-limited Gaussian beam has a M^2 factor of 1. For a given beam divergence angle, which is limited by the numerical aperture of the focusing lens, the M^2 factor limits the degree to which the beam can be focused. Together with the optical power, the beam quality factor determines the radiance of a laser beam. The degree of linear polarization is normally quantified by the polarization extinction ratio (PER). This is defined as the ratio of the optical powers in the two polarization directions.

Effects of Laser Parameters

Ideally, a LIDAR system would be built with a custom laser through which pulse outputs are directly controlled. Pulse repetition frequency (PRF), energy, and width could then be changed to suit the particular application. While this kind of direct control provides inherent operating advantages related to quality monitoring, designs driven by free-running lasers allow the use of cheaper COTS components. The tradeoff is that system operations may then be affected by small per-pulse variations (if not directly monitored). The capability to swap in cheaply available lasers operating at different PRF, however, allows for such systems to approximate the versatility of a more

expensive directly controlled laser. Additional diagnostic operations may prove critical for ensuring accuracy; without direct control of the laser, generating a time history of events related to laser fire is essential to limiting errors in point cloud generation. For example, one way to monitor PRF is to “tag” each laser pulse with GPS times. By similarly tagging certain scanner characteristics, mechanical components can be simultaneously monitored for stability.

Operating Wavelength

An imaging LIDAR is an active remote sensing instrument, meaning that it illuminates the investigated area with its own energy source (via a collimated beam of light) rather than relying on passive solar illumination. The selection of the specific wavelength and amount of output energy per laser pulse has direct relation to the sensing capabilities of the system. The propagation characteristics of electromagnetic radiation through a given medium are dependent on the incident wavelength. For example, visible green light (532 nm) exhibits low attenuation through water [41], making it the preferred wavelength for bathymetric applications. Fig. 2-5 shows the spectral dependence of typical water absorption coefficients.

Laser Pulse Width

The width of the outgoing laser pulse has particular importance for a system operating at low output energies. Bathymetry is one area where this can be demonstrated, because discrimination between sea surface and sea bottom returns is of prime concern. For this application, it is necessary that light-matter interactions produce sufficiently short return pulses to differentiate the two responses. It is possible to produce feature classification given that these requirements are met, as is illustrated in the following simulations.

MATLAB was used to convolve the Gaussian function shown in Fig. 2-6 with two discrete Dirac delta functions. This mimics two “ideal” reflections – i.e., no contributions due to roughness or slope – of a laser pulse from a sea surface and bottom. The height of the two discrete elements was set to 0.3 and 0.7 to produce more contrast in convolution operation result. The separation of the two elements was varied from 1 to 6 m to simulate different water depths. The resulting responses for convolution operations of the 10 ns FWHM (3 m in air) pulse in Fig. 2-7 shows how differentiation between surface and bottom is only possible at the larger depths, i.e. 4 m and larger.

An outgoing laser pulse width of 480 ps (Fig. 2-8) – 1/20 of the previous value – requires much less depth to produce significant differentiation between surface and bottom signals. Simulating a 1 m depth, which produced no temporal separation of signal events in the previous simulation, now shows a clear division. 480 ps corresponds to a distance of 0.144 m in air. The two signals are resolvable at twice this value, or 0.3 m (Fig. 2-9).

Pulse Energy

If we consider outgoing laser pulse energy as an accumulation of highly coherent individual photons, the ideal photodetector pairing to sense backscattered radiation would be sensitive to even a single returning photon. As will be described in the following section, detector improvements have brought this ideal closer to the realm of possibility. In order to estimate the output energy required for single photon detection, the signal strength is estimated as a function of transmitter, receiver, and environment characteristics. The uncertainty of an observation can be measured as a function of the various errors sources [42]. Even for a radiation field of constant intensity, the number of photons arriving at the photodetector for a given time interval is inherently uncertain

due to the discrete nature of the incident light, charge carriers, and the interaction of light with the photodetector [43]. The relationship between the number of photons incident on the detector and the number of emitted photoelectrons (p.e.) can be expressed via a Poisson distribution. The probability of n_t detected p.e. is therefore,

$$P(n_t, n_s) = n_s^{\,n_t} \cdot \frac{e^{-n_s}}{n_t!}, \tag{2-4}$$

where n_s is the expected number of p.e. recorded by the receiver. The probability of registering at least one signal event can then be calculated as a function of n_s [44]. For example, it is expected that for a signal level of one p.e., there is a 63.21% chance that there will be a signal event registered. The LIDAR link equation relates basic elements to estimate backscattered signal strength. A modified form of this equation yields the following expression for transmitted energy per laser pulse [15],

$$E_t = \frac{h\nu \cdot n_s}{n_h n_q n_r \cdot \rho_\lambda \cos(\alpha) \cdot \frac{A_r}{\pi R^2} \cdot \left[\exp(-\beta_{e,\lambda} R)\right]^2}, \tag{2-5}$$

where n_h is the hologram (in the case of an altered beam) efficiency, n_q is the detector quantum efficiency, n_r is the receiver optical efficiency, h is Planck's constant, ν is the photon frequency in hertz, ρ_λ is the wavelength-dependent surface coefficient, α is the local incidence angle on the surface, A_r is the collecting area of the receiver aperture, $B_{e,\lambda}$ is the atmospheric extinction coefficient per meter, and R is the range to surface.

Table 2-1 shows sample system parameters for moderate laser output power, modest telescope aperture, and average efficiencies for commercially available materials. The sample values indicate that we expect 20% transmission loss from the

hologram creating the beamlet pattern; 28% quantum efficiency in the detector; 60% loss due to spatial and spectral filters; 15% reflectivity for typical ground soil at 532 nm; a 6.5 cm diameter telescope; and 600 m flying height. To have a 63.21% chance of detecting one signal event, the transmitted energy E_t should be larger than 13.5 nJ. Goddard Space Center test flights of a scanning laser altimeter aboard a NASA P3B aircraft has shown potential for instruments operating at low pulse power and PRF [16]. Fig. 2-10 describes the test parameters and ranging results with respect to buildings, tree canopy heights, and shallow water bathymetry.

Selecting a LSNR Photodetector

Operating at low pulse energy and thereby LSNR requires a detector with high gain capabilities. There are several types of light sensors commonly used for LIDAR mapping.

Avalanche Photodiode

One type of sensor classically used to convert weak light backscatter into analog electrical signals is the avalanche photodiode (APD). APDs are high-speed (up to 250 ps rise time) photodiodes using an internal gain mechanism that functions by applying a reverse voltage. When light enters a photodiode, electron-hole pairs are generated if the incident energy is higher than the band gap energy. The drift speed of these electron-hole pairs or carriers depends on the electric field strength. As these carriers collide with the crystal lattice, ionization in which new electron-hole pairs are generated takes place. This starts a chain reaction referred to as the avalanche multiplication of photocurrent [45].

The internal gain effect of an APD is normally between 100 and 500 [Perkin-Elmer 2006]. It is possible to achieve very high gain – 10^4 to 10^6 – by operating an APD in "Geiger mode," which refers to a sensor biased above its breakdown voltage. An APD will normally conduct a large current when biased above breakdown, but if this current is limited to less than the APD latch current, there is a strong statistical probability that the current will fluctuate to zero in the multiplication region. The APD will then remain in a nonconductive state until an avalanche pulse is triggered by either a bulk (dark current) or photo-generated carrier. By keeping the number of bulk pulses low, the APD is then used to count individual current pulses from incident photons. Minimization of the dark current is a significant factor for this type of APD operation, and is reduced by cooling.

APDs are commercially available that span the spectral range from 300 to 1700 nm [46]. Silicon (Si) APDs can be used from 300 to 1100 nm, germanium (Ge) between 800 and 1600 nm, and indium gallium arsenide (InGaAs) from 900 to 1700 nm. InGasAs APDs are typically available with low noise current, extended spectral response to 1700 nm, and high frequency bandwidth for a given active area. Ge APDs are useful for applications under high electro-magnetic interference, where amplifier noise is significantly higher than APD noise [45]. APDs with high gain and fast rise times, however, often exhibit slow relative decays (10-100 ns), however, causing range tails as shown in the Jigsaw sensor [24].

Photomultiplier Tube Advantages

The photomultiplier tube (PMT) is another type of light sensor that provides very high internal gains similar to those of a Geiger mode APD. Generally PMTs are able to achieve higher internal gains – up to 10^7 – than APDs with superior recovery times. They also, however, require voltages from 1 to 3 kV, are more fragile, and more

sensitive to stray magnetic fields. For system designs intending to amplify single photoelectron events, PMTs can be attractive as long as they remain robust under normal system operation.

Combinations

A LIDAR system can use a combination of an APD and a PMT in order to compensate for varying environmental response. In the bathymetric case, for example, deep water causes rapid decay in the power of the received signal. Depending on the water depth and clarity, there can be more than six orders of magnitude dynamic range between strong water interface returns and weak bottom returns [47]. This difference must be handled by the detector without anomalous effects and compressed into the useful input range of the detector, which is typically only two or three orders of magnitude.

The use of a PMT or high-gain APD alone for bathymetric mapping can cause several problems related to the strong interface reflections that occur frequently near nadir. Even with the tube gated off, high incident light levels can cause a build-up of space charge around the photocathode [47]. This can affect output signal levels, linearity, and bandwidth. The result is a decrease in performance and may even be damaging to the tube. There is also experimental evidence of “afterpulses” at a delayed time after the impulse as a result of overly strong input signals [48]. This idea will be explored in greater depth in a subsequent chapter. Unexpectedly large surface returns may also create detector saturation, and corresponding distortion in the output waveform [49].

The U.S. Army Corps of Engineers' Scanning Hydrographic Operational Laser Survey (SHOALS) system uses an APD to measure the bottom response in depths

shallower than 14 m, and a PMT for depths deeper than 8 m. A measure of the returned power is recorded via waveform digitization. The received power and resulting waveform is a function of the transmitter and receiver characteristics, target laser cross section, and atmospheric effects, and target reflectance [11]. Fig. 2-11 shows how this information can be analyzed to produce classification of the surface return, volume backscatter, and bottom return. Analyzing responses from two types of detectors can thus improve characterization of benthic information.

Ideally, a single highly sensitive detector would be able to handle difficult classification problems such as the aforementioned issues associated with LIDAR bathymetry without negative consequences. If this were possible, the need for multiple sensors or waveform digitization could be eliminated, allowing for a more simplistic system structure with low overhead.

Photodetector Improvements

We now present an overview of recent photodetector improvements in order to estimate the capabilities of a highly sensitive detector when paired with a low energy laser.

Photon Counting

Large pulse energy lasers produce enough light backscatter from illuminated targets to generate multiple photoelectric events at the detector. For highly sensitive detectors, this is referred to the multiple photoelectron state. As shown in Fig. 2-12 [50], repeated photoelectron emission in this state creates output pulse intervals so narrow that they overlap each other. The combination of these overlapped pulses results in a signal of consistent amplitude with high-frequency components, or Fig. 2-13(a) [51]. The output signal is effectively the mean value of this waveform containing the AC

component. When the incident light level drops to a fraction of its previous level as in Fig. 2-13(b), the AC component becomes more significant. In a very low incident light state as in Fig. 2-13(c), the individual discrete pulses can be analyzed in a digital mode.

Recent advancements in PMT design have led to improved precision, sensitivity, and robustness in commercially available units. Commercial and developmental single-photon sensitivity detectors now exist which are capable of providing centimeter level ranging resolution [15]. Typical photocathode / dynode / anode configurations had previously been singular; new units are available in multi-channel arrays. These configurations allow for the receiver to angularly resolve the source of a single photon event within the receiver field of view [15]. If the time resolution of the PMT is sufficiently fast that the average time intervals between signal pulses are wide in comparison, then individual photons can be “counted” and the receiver is then capable of “photon counting,” or single photon sensitivity. It can be argued that because the generation of a photoelectron in this configuration is essentially a binary event given proper discriminators, the photon counting method is superior to analog signal measurement in terms of detection efficiency and stability.

Semiconductor Principles

Semiconductor PMTs operate on the principle of the external photoelectric effect, by which photoelectrons are emitted into a vacuum from a material called the photocathode [52]. The wavelength of maximum response and long-wavelength cutoff are determined by the combination of alkali metals used for the photocathode and its fabrication process. In a semiconductor band model, there exists a forbidden band gap or energy gap (EG) that cannot be occupied by electrons. The electron affinity (EA) is an interval between the conduction band and the vacuum level barrier (vacuum level).

The work function (ψ) is the energy difference from the Fermi level and the vacuum level. When photons strike a photocathode, electrons in the valence band absorb energy and become excited, diffusing toward the photocathode surface. If the diffused electrons have enough energy to overcome the vacuum level barrier, they are emitted into the vacuum as photoelectrons. The quantum efficiency $\eta(v)$ is the ratio of output electrons to incident photons, given by,

$$\eta(v) = (1-R)\cdot\left(\frac{P_v}{k}\right)\cdot\left(\frac{1}{1+kL}\right)\cdot P_s. \tag{2-6}$$

- R : reflection coefficient
- k : full absorption coefficient of photons
- P_v : probability that light absorption may excite electrons to a level greater than vacuum level
- L : mean escape length of excited electrons
- P_S : probability that electrons reaching the photocathode surface may be released into the vacuum
- v : frequency of light

In the above equation, if an appropriate material is chosen to determine parameters R, k, and P_v, the factors that dominate the quantum efficiency will be L (mean escape length of excited electrons) and P_S (probability that electrons may be released into the vacuum). L becomes larger by use of a better crystal and P_S greatly depends on electron affinity (EA).

If a surface layer of electropositive material such as Cs_2O is applied to a photocathode, a depletion layer is formed, causing the band structure to be bent downward. This bending can make the electron affinity negative. This state is called

NEA (negative electron affinity). The NEA effect increases the probability (P_S) that the electrons reaching the photocathode surface may be emitted into the vacuum. In particular, it enhances the quantum efficiency at long wavelengths with lower excitation energy. In addition, it lengthens the mean escape distance (L) of excited electrons due to the depletion layer [50].

Micro-channel Plate Photomultiplier Tube Concept

PMTs normally operate via a chain of dynode stages. After a photoelectric event, each dynode stage increases electron production by a certain degree; the product of these combined amplifications results in the overall gain. MCP-PMTs are different in structure and operation from conventional discrete dynodes. An MCP consists of millions of very-thin, conductive glass capillaries (4 to 25 microns in diameter) fused together and sliced into a thin plate. The two surfaces of the plate are covered with thin metal electrodes, and a voltage is applied to create an electric field in the direction of the channel axes. Electrons emitted by the photocathode of the PMT enter the capillaries. After a wall-electron collision, secondary electrons are accelerated by the electric field and travel along parabolic trajectories determined by their initial ejection velocity. As a result of repeated secondary electron emissions, the electron current increases exponentially as the electrons travel through the micro-channel-plate [51]. The schematic structure of the micro-channel plate is shown in Fig. 2-14 along with the principle of multiplication.

MCP-PMT Gain

The gain of a MCP-PMT is determined by the length-to-diameter ratio $\alpha = \frac{L}{d}$ of a channel, and the secondary emission characteristics gain factor G. The gain factor is a

product of the inherent characteristics of the channel wall material. The overall gain is approximated as,

$$\mu = \exp(G \cdot \alpha) . \tag{2-7}$$

In general, it is possible to obtain a higher gain μ by increasing α, which also moves the gain rising point to the higher voltage side. This is not without upper bound, however, because at some point the noise begins to increase significantly due to ion feedback events. An upper threshold for α =40 is usually selected so that a single MCP provides a gain of 10^4 at 1 kV supply voltage [51]. A two-stage MCP-PMT can then provide high enough gain to enable photon counting measurements, i.e. from 10^5 to 10^6.

Employing thousands of independent amplifying micro-channels allows for a MCP-PMT to avoid geometric saturation effects that can hinder more conventional high gain, segmented anode, metal dynode chain photomultipliers. In the latter, any noise photons that hit a particular portion of the photocathode can uniformly deplete the gain in the corresponding anode. In an MCP-PMT, however, a noise photon can drain a particular micro-channel (or set of micro-channels) without affecting the others in a given anode.

When a single photon enters a MCP-PMT, the photocathode converts it into an electron which travels to the anode while being multiplied. The transit time of the resulting electron bunch differs depending on the input photon. The distribution of this transit time is referred to as the transit time spread (TTS). In most photomultiplier tubes, the electron transit time is dependent on the position of photocathode illumination. When the entire photocathode is uniformly illuminated, the difference in transit time with respect to position is referred to as the cathode transit time difference

(CTTD). The TTS is usually affected by the CTTD, but in the case of proximity-focused MCP-PMTs, it has little effect [51].

During the multiplication process from cathode to anode in a metal dynode chain PMT, the signal pulse can be broadened due to the emission-angle distribution and initial-velocity distribution of photoelectrons and secondary electrons, as well as the effect of the focusing lens. MCP-PMTs can largely ignore this effect because a strong electric field is applied nearly parallel from the photocathode to MCPin and MCPout to anode. Since the plate takes the place of a conventional dynode structure, the electron transit time in the secondary electron multiplication process is also very short, allowing for TTS up to 25 ps in Hamamatsu MCP-PMTs [51].

MCP-PMTs are available in small packages, with 100 anode configurations less than 6 x 6 x 3.5 cm. In magnetic fields parallel to the tube axis, the tube can be stably operated for fields up to 2.0 T. For fields perpendicular to the axis, the output drops drastically if fields exceed 0.07 T. Current micro-channel plate implementations are able to offer compact size, fast time response, and two-dimensional detection with high spatial resolution, and stable operation in high magnetic fields [51].

Detection Efficiency and Pulse Height Distribution

The effective capability of a PMT to collect photoelectrons emitted from the photocathode is called the collection efficiency (ε). This value, combined with the photocathode quantum efficiency (η), directly affects the measured signal. The ratio of the number of output pulses (N_d) to the number of incident photons (N_p) is called the detection efficiency [51],

$$\gamma = \frac{N_d}{N_p} = \varepsilon \cdot \eta \ . \tag{2-8}$$

The output pulse height can vary depending on fluctuations in the secondary electron emission ratio. In order to gauge the time-varying response of a PMT, it is useful to consider a pulse height distribution (PHD) plot. This plot is a histogram of accumulated pulse heights given a series of test data, shown in Fig. 2-15(A) [51]. A typical PHD signal-to-noise comparison is shown in Fig. 2-15(B). Note that the noise line exists even with no illumination of the photocathode; these events result from thermionic emissions (thermal or dark noise events).

When the incident light level is increased, the amplitude of the signal + noise increases as shown in Fig. 2-16(A). Increasing the supply voltage causes the PHD curve to be stretched and flattened as shown in Fig. 2-16(B). These images illustrate how detection efficiency is affected by threshold level. For example, the first valley in the PHD waveform is usually selected as the lower level discriminator (LLD), and a point midway down the falling edge of the waveform is selected for the upper level discriminator (ULD) [50]. Since a large portion of the noise often occurs at lower pulse heights, an appropriate setting can allow for filtering of thermal (dark noise) events. If, for instance, the LLD is selected far to the right of the waveform peak, the majority of signal events may not be passed once the output pulses are brought into a binary signal.

Experimenting with LLD settings other than the initial valley is not without merit, however, depending on the application. If a large amount of noise is causing signal classification problems in data post-processing, one solution may be to increase the LLD to a point where only multi-photon events have a high probability of being detected.

Re-collecting the data within a multi-photon state rather than a single-photon state can have advantages for cleaning up very noisy signal as long as the signal provides a strong response. Decreasing the PMT supply voltage can have the same effect; both values have significant impact on the overall detection efficiency.

Variation in PMT Gain and Output Instability

The effect of changing the supply voltage can be seen by counting the number of pulses with the LLD fixed. Although the analog gain increases exponentially with supply voltage, the number of counted pulses remains fairly constant for a certain range. This range is referred to as the plateau characteristic, and analyzing the associated plot indicates an appropriate region for setting the supply voltage. An example of a plateau characteristic is shown in Fig. 2-17, which also illustrates why the photon counting method is relatively insensitive to small-scale supply voltage fluctuations. The signal to noise ratio remains flat throughout the plateau range. Even when the gain changes significantly as a result of supply voltage instability (Fig. 2-18), the photon counting mode remains stable with respect to count rate [50].

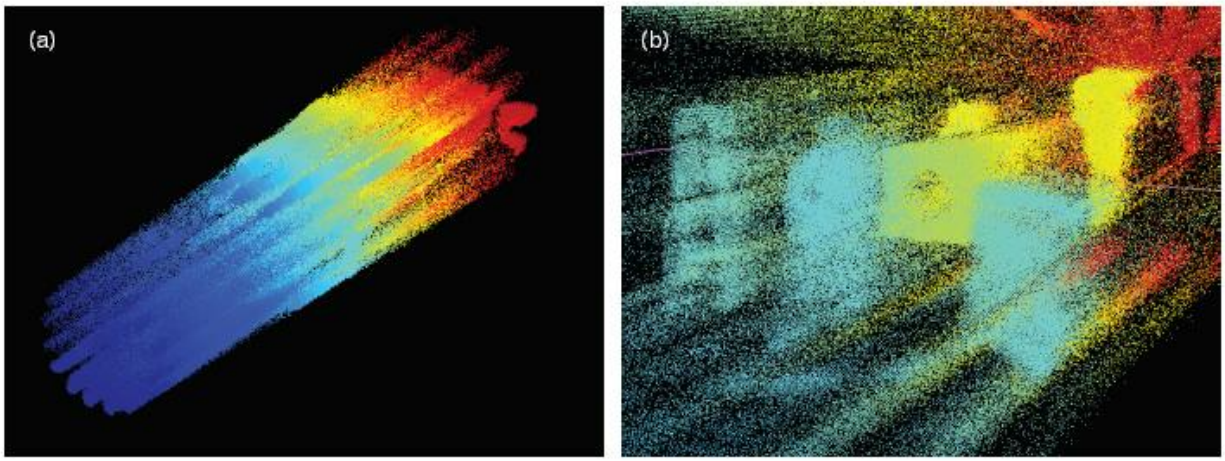

A B

Figure 2-1. Point clouds resulting from data collected by the DARPA Jigsaw program sensor at MIT Lincoln Laboratory. A) Raw Jigsaw data colored according to range relative to the sensor. B) View from inside the raw point cloud of genuine signal and background noise [24].

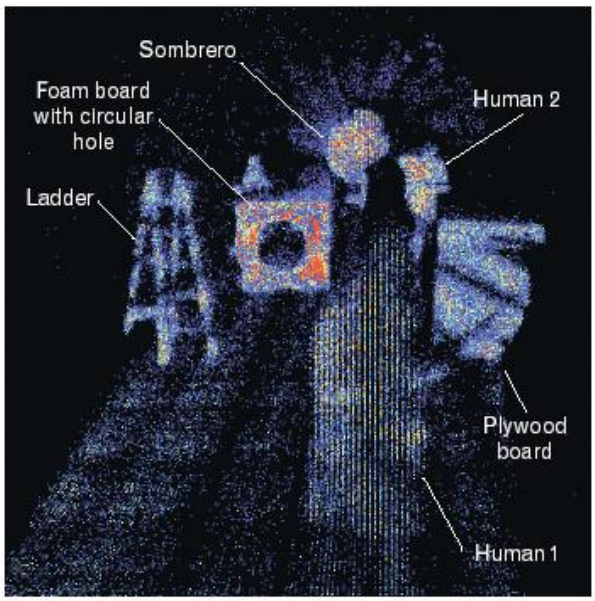

Figure 2-2. Point clouds resulting from Jigsaw sensor data after filtering algorithms are applied. Following preliminary cleaning of the 3D image, human subjects and test-range objects are much more apparent than in the raw input [24].

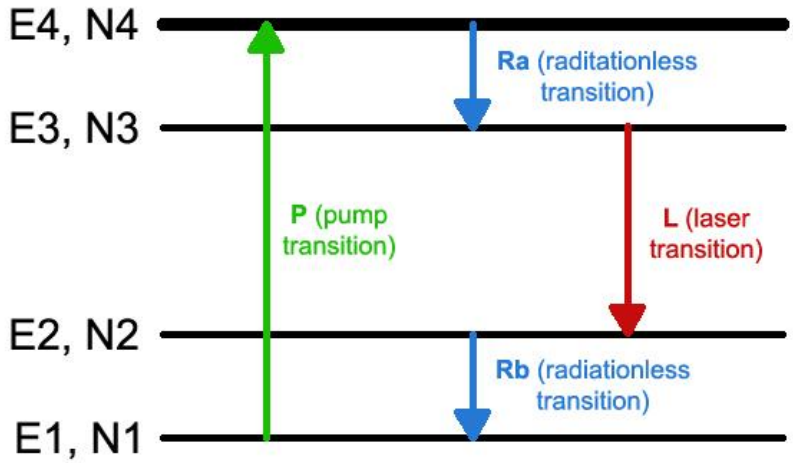

Figure 2-3. Diagram of energy level transitions in four-level laser.

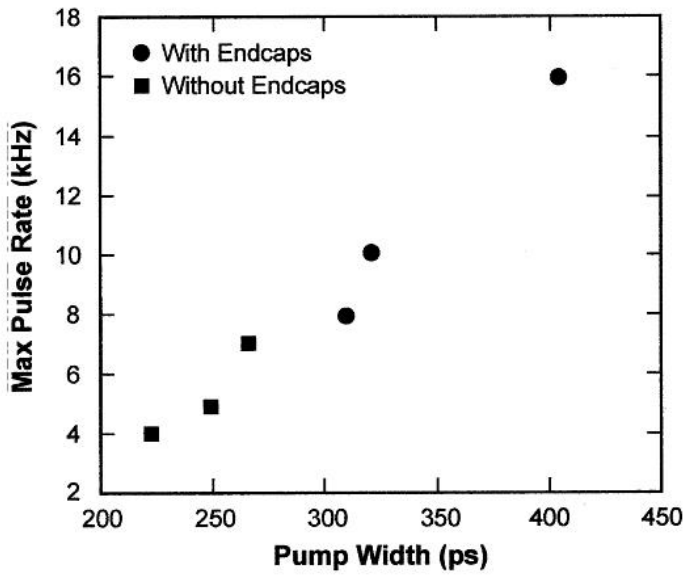

Figure 2-4. Maximum pulse repetition rate versus pulsewidth in SPMCL PQS microchip laser [39].

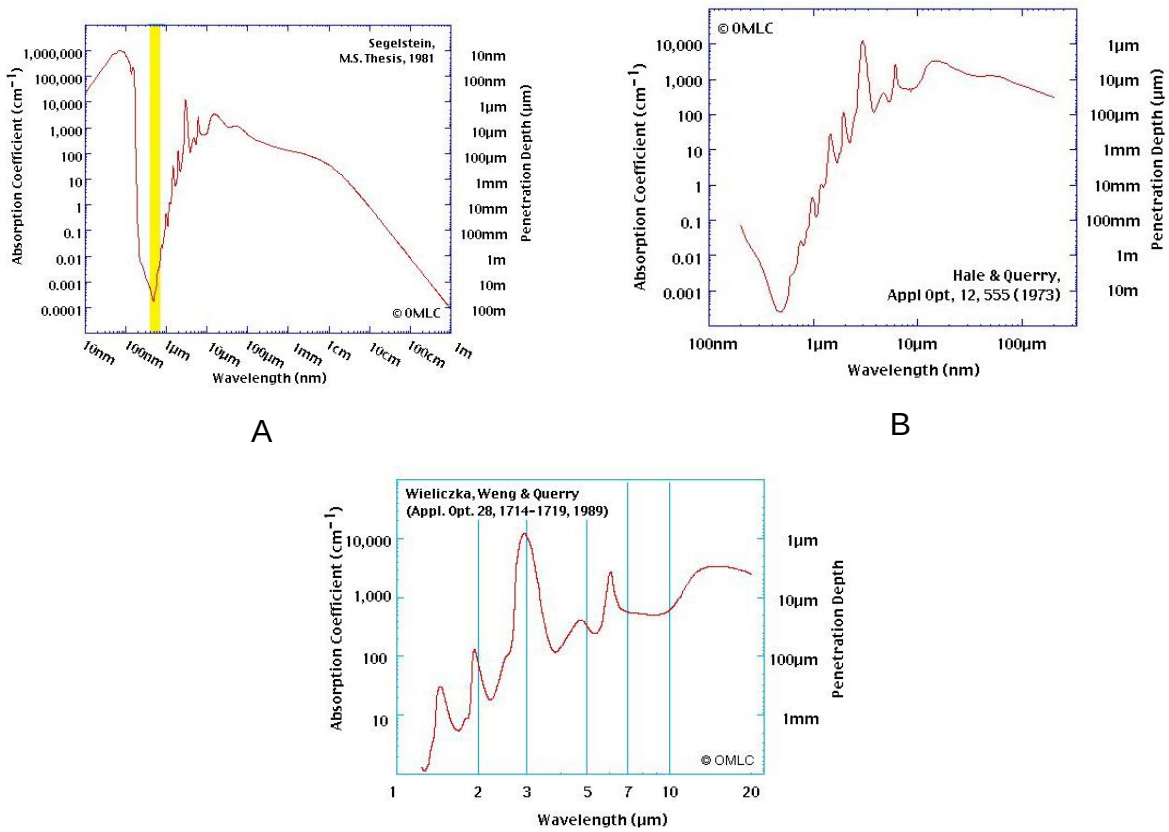

Figure 2-5. Typical absorption coefficients of water as a function of wavelength [41]. A) Segelstein, 1981; B) Hale and Querry, 1973; and C) Wieliczka, Weng and Querry, 1989.

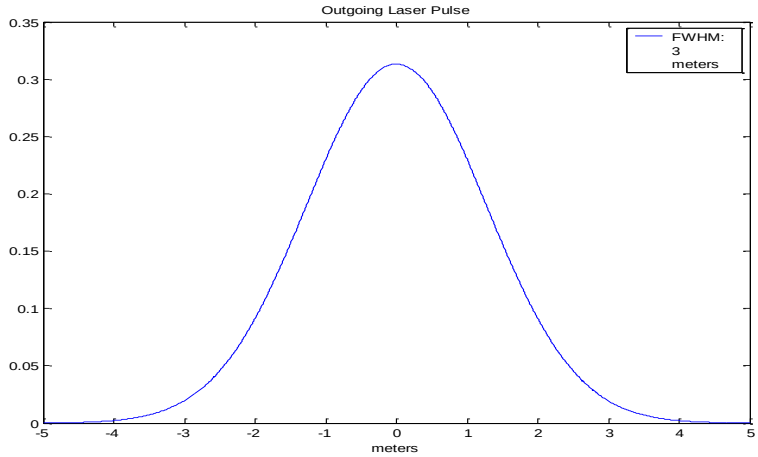

Figure 2-6. Gaussian-shaped function generated in MATLAB to simulate a “long” outgoing laser pulse. This plot corresponds to a “long” system pulse width of 10 ns at full width half maximum (FWHM), or 3 m (in air).

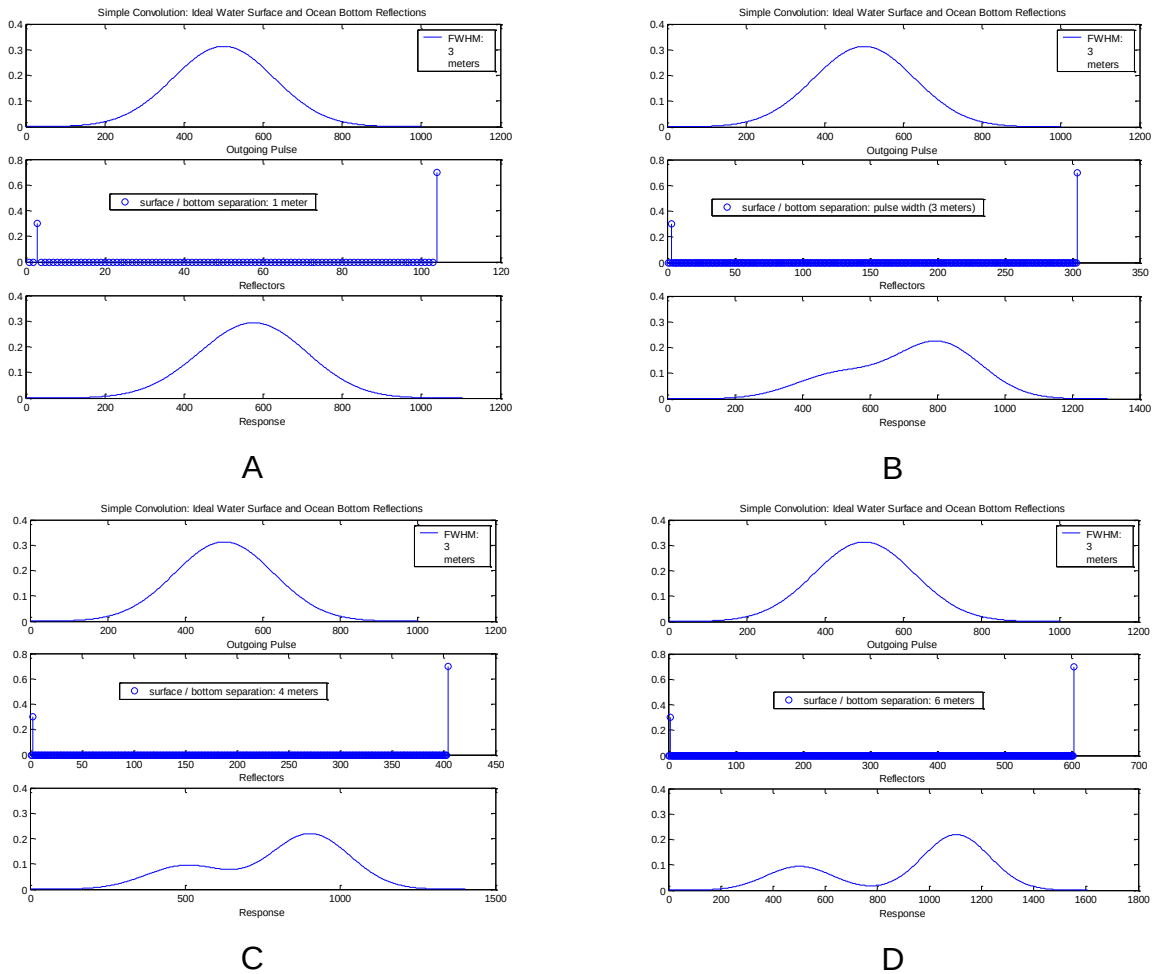

Figure 2-7. Simulation of ideal water surface and ocean bottom reflections for a “long” pulse width (10 ns). Three subplots are shown for the outgoing pulse, “ideal” reflectors, and resulting response. Depth is varied for four plots. A) Depth of 1 m. B) Depth of 3 m. C) Depth of 4 m. D) Depth of 6 m.

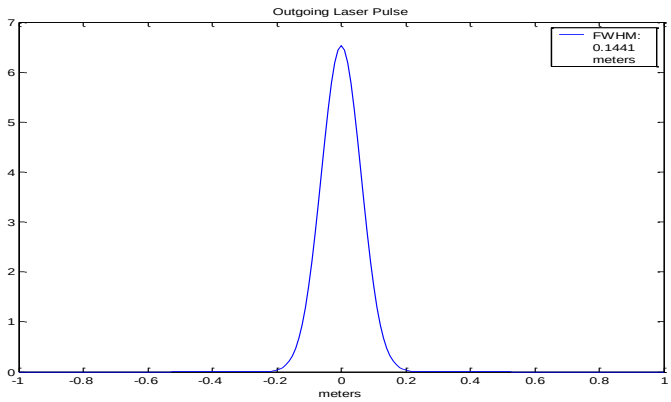

Figure 2-8. Gaussian-shaped function generated in MATLAB to simulate a “short” outgoing laser pulse width. This plot corresponds to 480 ps at FWHM, or 0.1441 m (in air).

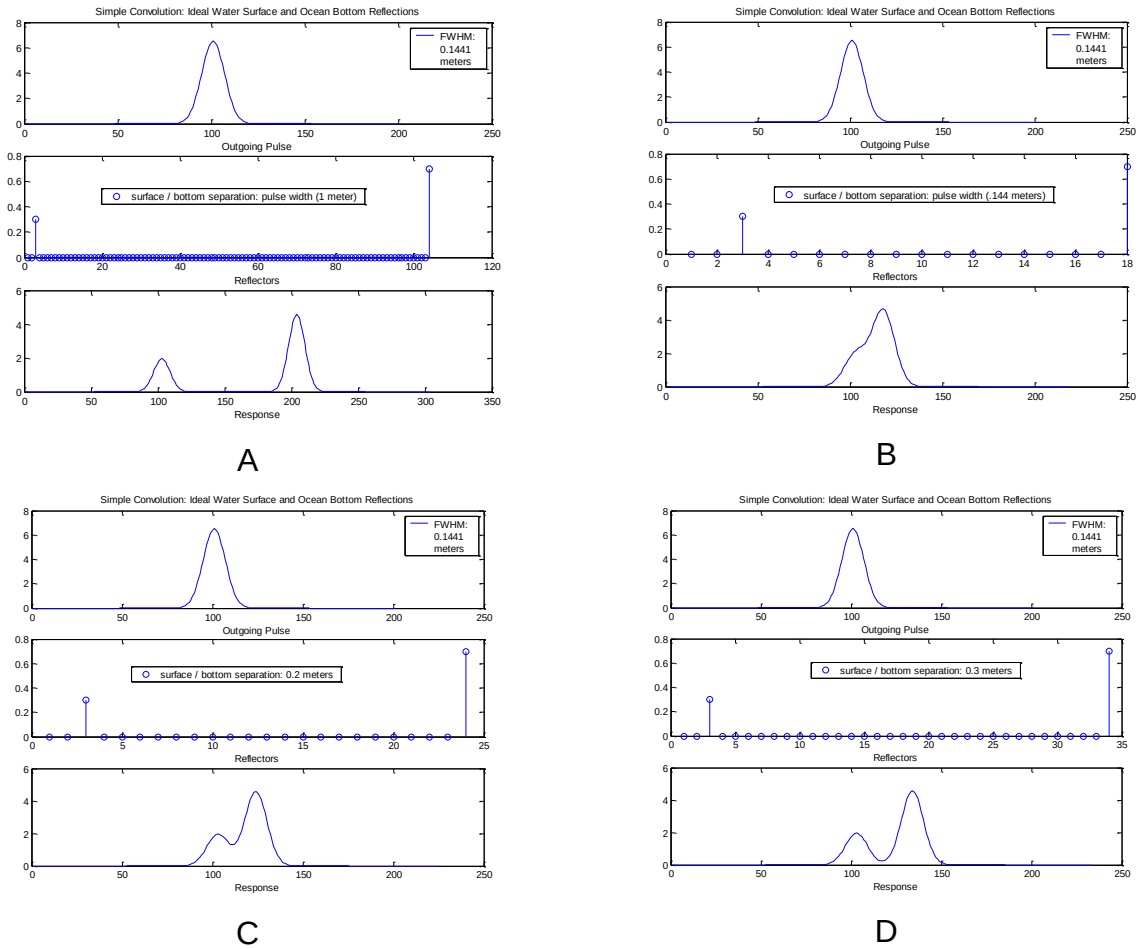

Figure 2-9. Simulation of ideal water surface and ocean bottom reflections for a “short” outgoing pulse width (480 ps). Three subplots are shown for the outgoing pulse, reflectors, and response. Depth is varied for four plots. A) Depth of 1 m. B) Depth of 0.144 m. C) Depth of 0.2 m. D) Depth of 0.3 m.

Table 2-1. Sample system parameters for use in LIDAR link equation.

n_h	n_q	n_r	h	v	ρ_λ	α	A_r	$B_{e,\lambda}$	R
0.8	0.28	0.4	$6.63 \cdot 10^{-34}$ J·S	$5.64 \cdot 10^{14}$ HZ	0.15	5º	$3.3 \cdot 10^{-3}$ M^2	$0.297 \cdot 10^{-3}$ M^{-1}	600 M

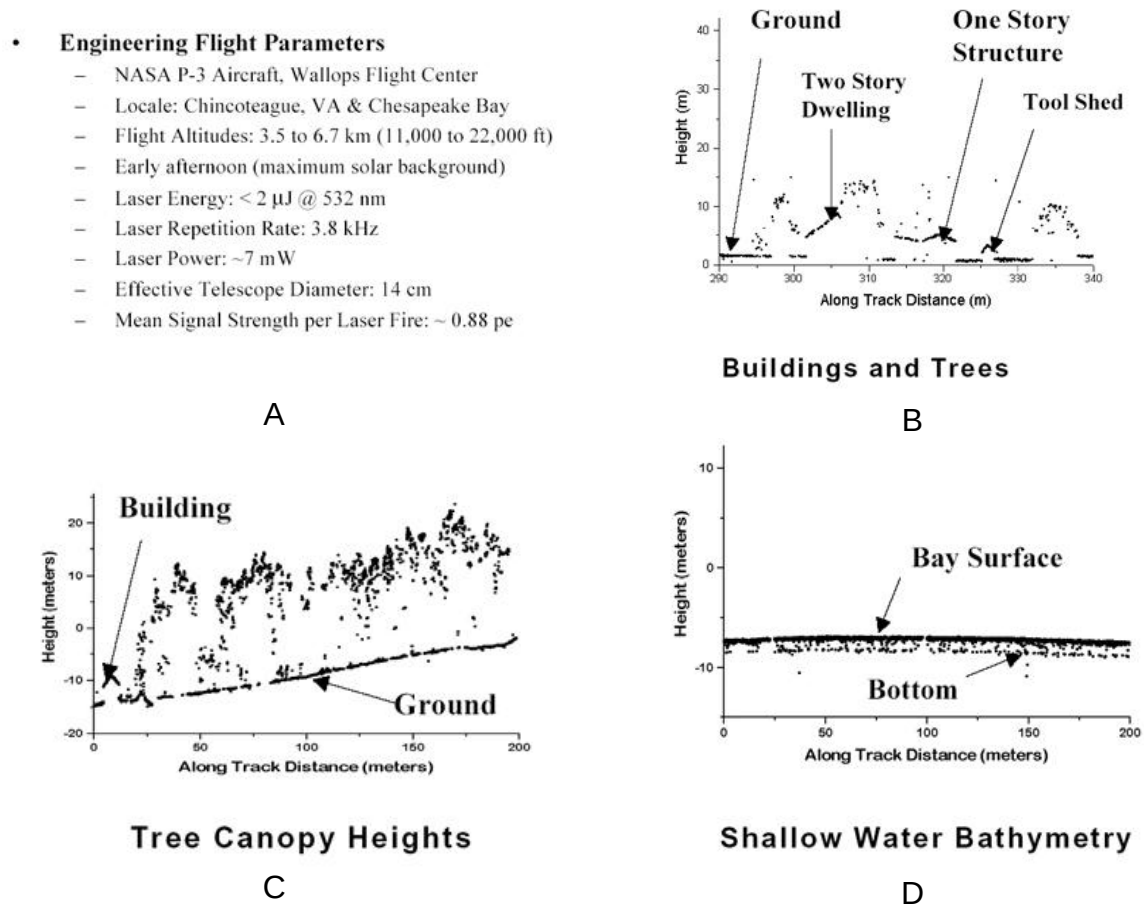

Figure 2-10. Data from NASA Goddard Space Center's microaltimeter instrument. A) Engineering flight parameters. Sample profiling data is shown from B) small buildings and trees in the town of Chincoteague, VA, from 6.7 km altitude, C) tree lines and underlying terrain from 3.4 km altitude; and D) shallow water bathymetry over the Chesapeake Bay from 3.4 km altitude [23].

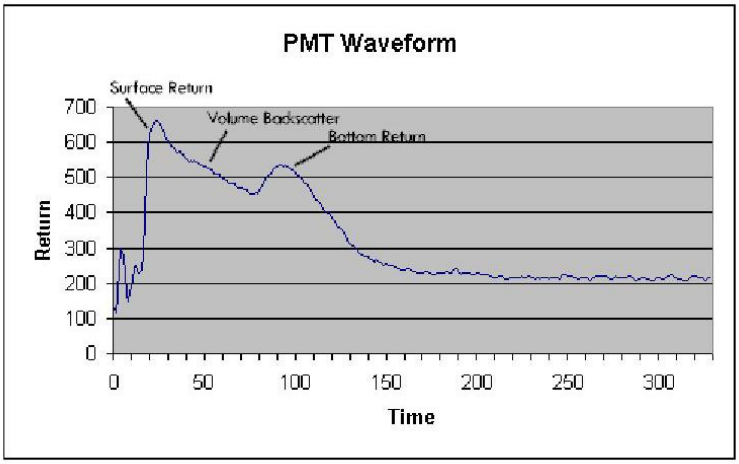

Figure 2-11. A typical return waveform from the Optech SHOALS bathymetric mapping system, measured by a PMT detector [11].

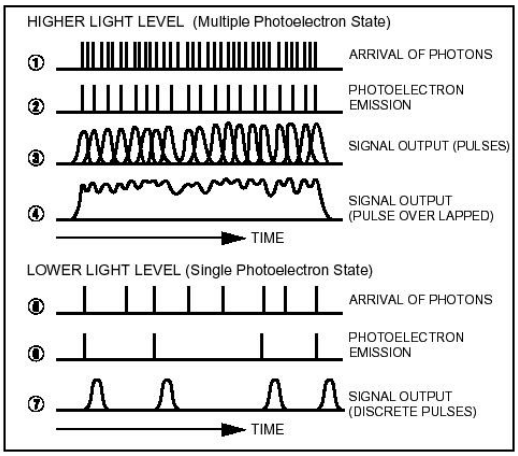

Figure 2-12. Output pulses from a PMT at different light levels.

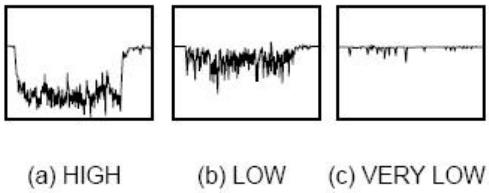

Figure 2-13. PMT signal under varying light intensities.

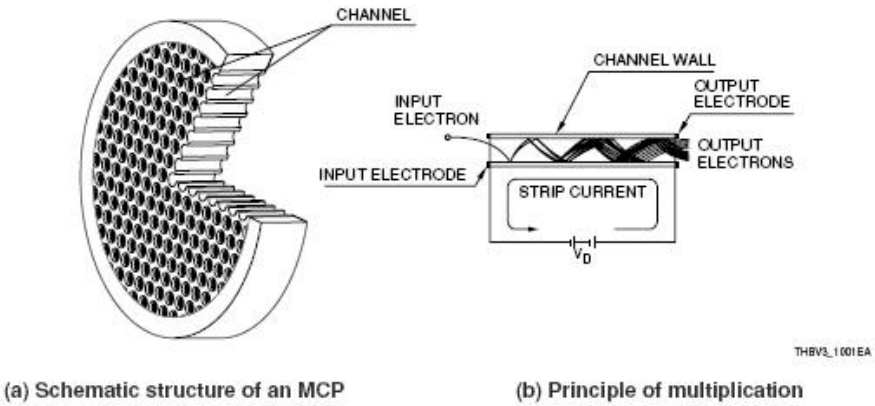

Figure 2-14. Schematic structure of a MCP-PMT and the principle of multiplication [50].

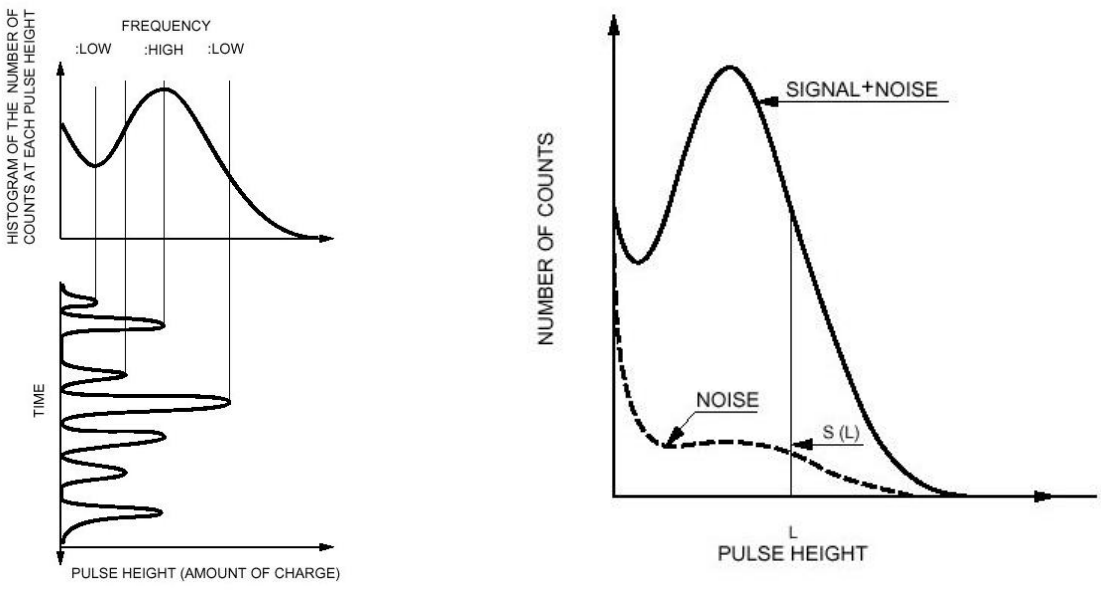

A B

Figure 2-15. Typical pulse height distribution plot (PHD) [50]. A) The histogram variation is shown mapped to pulse heights from a train of incoming pulses. B) Noise and signal are compared in a PHD plot.

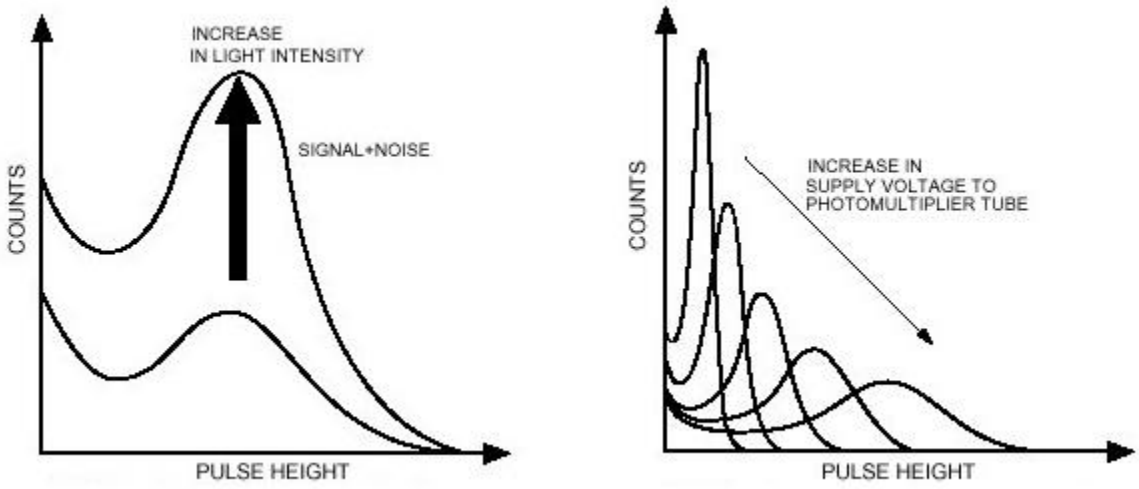

A B

Figure 2-16. PHD plots depicting an increase in incident light level (A) and supply voltage (B).

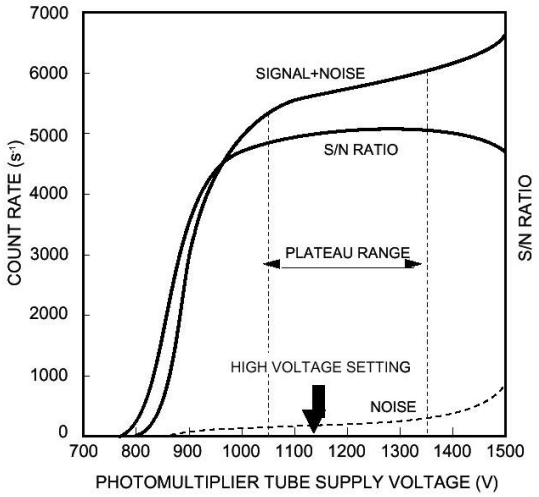

Figure 2-17. Typical PMT plateau characteristics.

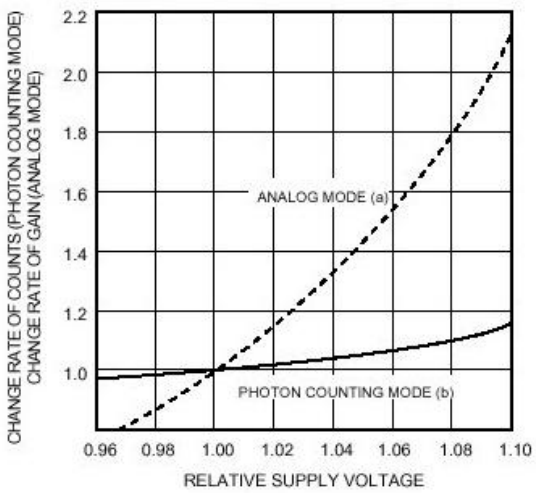

Figure 2-18. Typical PMT output variation versus supply voltage.

CHAPTER 3
LSNR PROTOTYPE DESIGN

Photon Counting System Prototype: CATS

Building upon the major concepts of Chapter 2, we now present a design for the optical framework and receiver package to enable single-photon laser ranging.

General Scanning Principles

Laser mapping systems typically employ a scanning mechanism to direct the path of outgoing laser pulses. The repetition rates (5 to 10 kHz) of commercially available micro-lasers combined with the flight speeds of commercial aircraft (60 m/s) make it necessary to illuminate a “patch” of terrain a few meters on a side to achieve contiguous coverage of the terrain on a single pass. Expanding the size of the ground footprint can be achieved by using a multi-element design. Instead of transmitting a single high energy beam, the outgoing laser pulse can be separated into many low-energy beamlets via holographic expansion to sustain coverage requirements. The result is nearly overlapping footprints with small (decimeter) inter-footprint pixel spacing.

System Proposal

The availability of a cost-effective microchip laser and high gain MCP-PMT served as a basis for the initial design of the University of Florida’s Coastal Area Tactical-mapping System (CATS). The CATS was built through a partnership with Fibertek, Inc. and Sigma Space Corporation. This LSNR prototype instrument operates at low power and low laser pulse rate while attempting to achieve contiguous ground coverage at a spatial resolution of a few decimeters. In order to meet these goals, a receiver processes returns at the single photoelectron level resulting from an array of outgoing light pixels. While the main application is the mapping of coastal areas, including the

shallow depth shore, single photoelectron laser altimetry has demonstrated that CATS could have advantages in developing high resolution digital topographic databases, monitoring biomass and vegetation heights, sea and lake levels, ice sheet thickness, etc. [23].

Optics

Fig. 3-1 shows a block diagram of the CATS optical path elements as they relate to the transmit and receive paths. Fig. 3-2 shows a more detailed image with the turning mirrors, mechanical shutter, receiver electronics, and fiber optic detector. Several tip-tilt mirrors deflect the beam at right angles in order to reduce the overall extent of the optical path. The chosen mirror coatings have 99.5% reflectivity at a wavelength of 532 nm.

Microchip Laser

In the CATS, a NanoPulse class IIIB microchip laser manufactured by JDS Uniphase produces high repetition rates, high peak power, and short pulses. The laser cavity consists of a Nd:YAG gain medium bonded to a YAG-saturable absorber. Pulsing is achieved through PQS. The cavity mirrors are vapor-deposited directly on each side of the crystal to form a monolithic oscillator that is end pumped by a CW diode laser. The NanoPulse laser product line shown in Fig. 3-3 generates 1064 nm output and can be optimized for either 50 mW of average power or 8 µJ pulse energy. In either case, the output is a pulse train of high peak power, sub-1 ns, near-diffraction limited pulses. The beam diameter is 0.2 mm with ± 2 mrad divergence. These lasers are capable operating at temperatures from 0° to 50° C at the base plate, and can be stored at temperatures from -20° to 60° C. The power stability over 6 hours was

measured to be ± 3%, the ellipticity ratio is 1.1:1, and the warm-up time is approximately 10 minutes.

A variation of the NanoPulse laser, called the NanoGreen, utilizes a potassium-titanyl-phosphate (KTP) frequency doubler at the same output as the crystal that is used for the NanoPulse to produce 532 nm pulses. An IR blocking filter is added to remove residual 1064 nm light. The PER is greater than 100:1 and the M^2 mode approximately 1.2 for a Gaussian beam profile. Field tests for beam polarization are shown in Fig. 3-4. The NanoGreen can be specified for up to 15 mW of average power or 3 μJ of pulse energy. The entire laser assembly is contained within a compact 15 x 4 x 4 cm package. Each manufactured laser has slightly different output characteristics. For the operational CATS laser, a thermal head sensor has measured 27 mW at the direct laser output (7.76 kHz), which corresponds to 3.48 μJ / pulse.

Beam Expander

Pulsed light passes through a beam expander, decreasing the beam spot size at large distances. There are two main types of beam expanders: Keplerian and Galilean. In the latter, the combination of a positive and negative focal length lens provide magnification of the beam diameter and then reduction of the divergence. Keplerian types achieve the same effect of producing a larger but highly collimated beam size, but with two positive focal length lenses. Contrasting the two, a Galilean design contains no internal focus point and the overall length of the Galilean as compared to a similar power Keplerian is smaller. In the CATS, a plano-concave and achromatic lens produce 10x total magnification; this reduces the beam divergence to 0.2 mrad.

BK-7 lens material with magnesium fluoride (MgF_2) coating is chosen for its compatibility with visible light applications, along with an anti-reflection coating. After

the beam expander, each pulse is passed through a holographic diffraction element that separates the beam into a 10x10 square array of beamlets rotated 45°. The efficiency of the hologram is approximately 80%. A lens in the transmit path is shimmed to increase the amount of defocus and resulting angular divergence of laser spots in the far field. The spot sizes then have 77% linear fill factor at the $\frac{1}{e^2}$ beam contour, or 46% area fill factor for 95% of the total energy. Outgoing laser beamlets pass through a shared afocal element resulting in a total magnification of 4x.

Risley Prisms

Laser light is deflected out of the shared afocal element through two Risley prisms, shown as cross-hatched elements in Fig. 3-5. Each Risley prism is simply an optical wedge V-coated for 99.5% light transmission. The refractive properties of this material combined with the wedge surface angle deflect the beam through a predicted path. BK7 material is selected with a refractive index of 1.52, wedge angle of 13.58°, diameter of 88 mm, and central thickness of 22.5 mm. Each incremental wedge rotation is slaved directly to the leading edge of a synchronization pulse associated with the fire of the laser. The wedges are set to rotate a constant angular amount between synchronization pulses, and can be independently controlled to move at varying speeds in either direction. Software routines created prior to system operation determine the frequency of the two rotations.

This allows for the array of laser beamlets to be deflected in a variety of repeatable patterns. The line scan in Fig. 3-6(A) closely approximates the familiar raster or sawtooth scan, with platform motion responsible for creating the along-track displacement. Raster scans are estimated to produce a maximum 225 m swath width

at an altitude of 600 m. An example of a different scan pattern available with the Risley prism design is shown in Fig. 3-6(B). By slightly offsetting the rotation speed of one of the prisms, the line scan can be made to rotate over time. This type of scan results in much denser coverage of points near nadir. Different types of patterns can provide enhanced coverage for specific applications. A test of time deviation of the nearest laser synchronization pulse from the wedge reference pulse indicates that the pulse position on the ground deviates by approximately 0.07 pixels from scan to scan; an acceptable margin.

Range Gate

The system is operated with a range gate of 100 to 150 m. The supply voltage on the tube provides full amplification only after a set amount of time has passed (related to the range gate setting); meaning that the power is temporally stepped in relation to the laser pulse train. This allows for the outgoing laser pulse to be sufficiently far away from the output window as to minimize electronic noise variables associated with laser fire. It also eliminates atmospheric backscatter immediately outside the aircraft and ensures that strongly reflective targets near the output window (atmospheric reflections, birds) do not produce a response. This helps to prolong the life of the photomultiplier tube.

Spatial and Spectral Filters

Resulting backscattered radiation passes back through the shared afocal element. Dust particles residing on optical surfaces may produce scattered laser light resulting in interference patterns. These patterns can produce contrasting background light that interferes with desired signal information. A simple way to deal with this interference is through a tight spatial filter. The idea here is to reduce the receiver field of view to the minimum value which encompasses the transmit beam divergence and potential

pointing variations and/or co-alignment errors with the receiver [15]. Scattered light can be blocked by centering a small aperture at the focal spot of the direct beam, while allowing the direct beam to pass through. The resulting cone of light has a smooth irradiance distribution and can be refocused to form a collimated beam that is almost equally smooth.

The laser returns are also passed through a spectral filter to further improve return signal quality before reaching the timing electronics. For systems operating at low signal to noise ratios, it is necessary that filtering operations be precise. In the CATS, an interference filter accepting wavelengths centered at 532.1 (+/- 0.05) nm with FWHM 0.25 (+/- 0.05) nm is used. The filter has a temperature coefficient of 0.002 nm / ºC. To further reduce scattered light reaching the active area of the PMT, a central mask is placed on the spectral filter to block out on-axis backscatter.

Dove Prism

The pattern of filtered beamlets is rotated 45° by a Dove prism. This optical element is made from truncated right-angle prisms such that a beam of light entering one of the sloped prism faces undergoes total internal reflection (TIR) from inside of the bottom face and emerges from the opposite sloped face in flipped image orientation [53]. By rotating the prism about its longitudinal axis, the transmitted image rotates at twice the rate of the prisms; meaning that they can rotate a beam of light by an arbitrary angle (45° in this case). The losses occurring as a result of the entrance and exit faces are reduced to a small fraction of a percent by using a dielectric V-coating for both surfaces.

Telephoto Lens and Mechanical Shutter

The resulting pixels are refocused by a telephoto lens before being imaged onto separate cathodes of a 10x10 segmented anode photomultiplier tube. Detected signals are sent to a 100 channel multi-stop ranging receiver. A mechanical shutter before the telephoto lens ensures that the photosensitive material is not subject to stray light during system transport and setup. The scanner window is also tilted relative to the optical axis to minimize reflection of photon back into the receiver. The receiver field of view (FOV) is a 3.5 m square. This is a larger aperture than the diameter of the transmitted bundle of beamlets.

MCP-PMT

Because a very low amount of reflected radiation is expected from each laser beamlet, a detector must be employed with high enough gain to amplify single photon events. In order to achieve 10^5 gains with 200 ps rise time, 25 ps transit time spread (TTS), and 200 ps dead time specifications, a micro-channel plate photomultiplier tube (MCP-PMT) was selected. This device is capable of simultaneously detecting independent events from a 10x10 pixel array, allowing for two-dimensional resolution. The MCP-PMT provides exceptional gain while maintaining compact size.

In the CATS, a 10x10 segmented anode array built by Hamamatsu Electronics Inc (model number R4110U-74-M100D), shown in Fig. 3-7(A), is capable of sensing single photon events. The aluminum housing of the MCP-PMT measures 5.330 x 5.330 x 3.175 cm. Three pins on the narrow end of the housing fit into a PCB that controls the high voltage applied to the tube. Detector signals are routed through a PCB attached to the back of the housing. Taking into account the aluminum mounts for these components, the combined volume of the detector module is less than 1000 cm^3. A

GaAsP (gallium-arsenide-phosphide) crystal activated with cesium is used as a transmission type photocathode, meaning that photoelectrons are emitted in the same direction as the incident light. This type of photocathode has high quantum efficiency (QE) in the visible region [51], with a plateau curve from 300 to 850 nm. The QE plot for the R4110U is shown in Fig. 3-7(B). The nominal photocathode uniformity, MCP gain uniformity, and crosstalk values are 76%, 70%, and 3.8% respectively. The dark noise is expected to be less than 270 counts per second at $4.5 \cdot 10^5$ gain.

Multi-stop Event Timer

Accurately detecting scattered light returns using single photon events can be complex. The negative impact of reduced signal levels relative to conventional altimeters is largely offset by the corresponding reduction in the detection threshold to about one photoelectron. Instrument sensitivity in this case is maintained or even enhanced [15]. The caveat to higher sensitivity is the increased presence of noise effects. Reduction of the detection threshold to approximately one photoelectron allows for robust detection at lower light levels. However, even with a range gate, narrow spectral filter, and tight spatial filter, typically there are sufficient noise events from atmospheric backscattering (especially in areas with atmospheric haze or fog) to warrant the use of a multiple stop event timer.

Noise events can be separated from terrain or vegetation returns because they are expected to be randomly distributed in time, or "temporally incoherent," in comparison to "temporally coherent" signals which rise above the noise floor [15]. This permits single photon detection in daylight with wide range gates as well as multiple returns per pixel per laser fire from volumetric scatterers such as tree canopies or turbid water columns.

More information on the processing electronics associated with multiple-stop event timing is found in the Appendices.

Multi-stop LIDAR sensors are capable of providing information about biomass in forest understories related to sunlight distribution [11], surveying the sea surface / floor in navigation channels, ports and harbors, coral reefs, beaches, and shorelines [11], [47], and classification between spatially mixed topographic features in urban and suburban areas [5]. Man-made objects that would be obscured to pilots in mission fly-overs such as tanks concealed in heavy brush or camouflage netting are able to be identified via observations of spatial structure in LIDAR point clouds [54].

Assembly and Footprint Dimensions

Fig. 3-8(A) shows the CATS sensor mounted on a tripod with laptop and power supply connections supported by an equipment rack. A close-up of the optics, enclosed scanner, and electronics cube contained within the black-colored metal assembly is shown in Fig. 3-8(B). Fig. 3-8(C) shows a zoom-in on the communications ports for laser and scanner operations. Fig. 3-8(D) shows communications ports for laser, timetag outputs, and range data throughput. Fig. 3-8(E) / (F) show the front / back of the scanner interface module.

Flying at nominal altitude (600 m), the system is expected to produce a horizontal spatial resolution of 20 cm at nadir. Fig. 3-9 shows a photo of several buildings in Lanham, MD. These structures were used to verify footprint dimensions. The diamond-shaped footprint is projected onto a brick wall in Fig. 3-10.

Manual measurements of the footprint projected onto the brick surface at night produced a side length of 0.99 to 1.01 m, an average of 1.00 m. The center-to-center spot spacing was 9.52 to 10.16 cm, an average of 9.84 cm. The spot size diameter was

4.45 to 5.08 cm, an average of 4.77 cm. In addition to a CATS distance measurement, the range to the wall was measured using an Optech ILRIS laser mapping sensor, and by Google Earth satellite photography. The average distance to the brick wall by these three independent measures was 303.76 m. Extrapolating these results to 600 m, the average side length would be 1.97 m, the center-to-center spot spacing would be 19.44 cm, and the spot size diameter would be 9.42 cm.

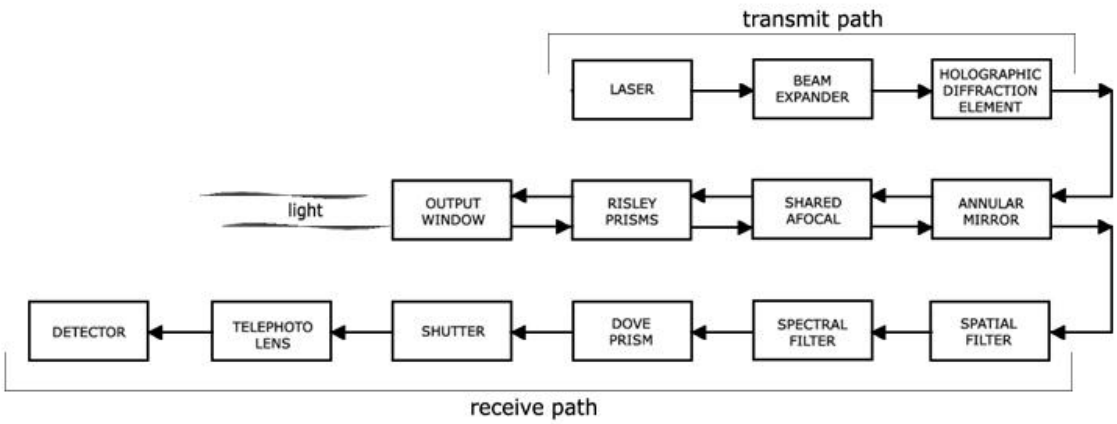

Figure 3-1. Block diagram of optical path layout.

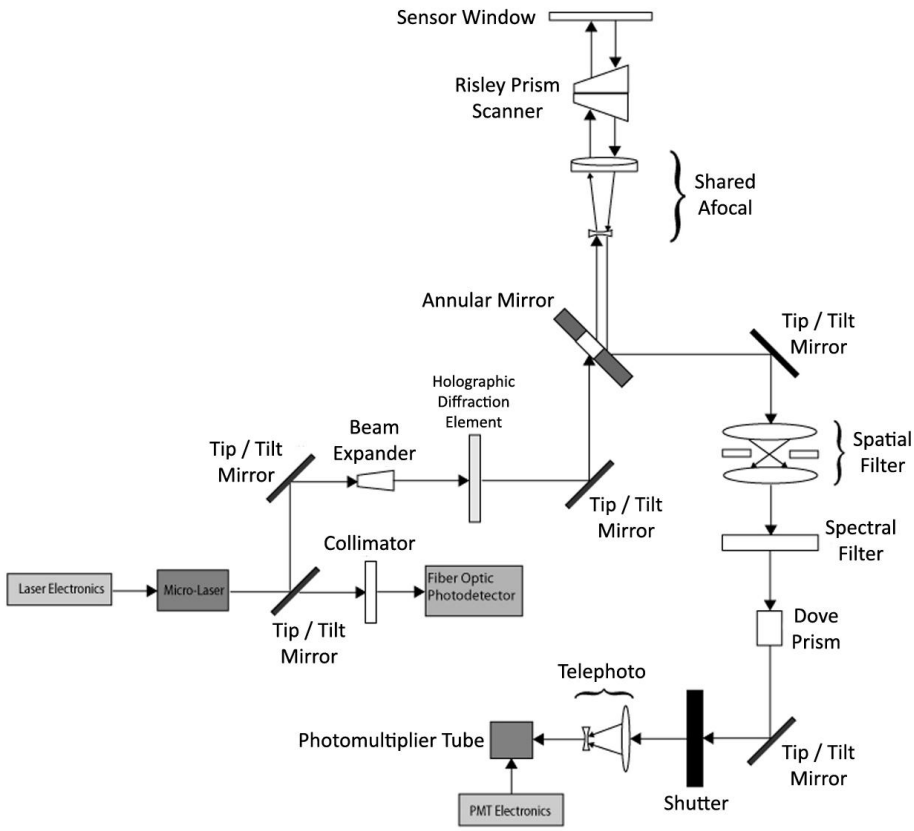

Figure 3-2. Detailed optical path with turning mirrors, mechanical shutter, receiver electronics, and fiber optic detector.

Figure 3-3. Photo of JDS Uniphase NanoPulse lasers.

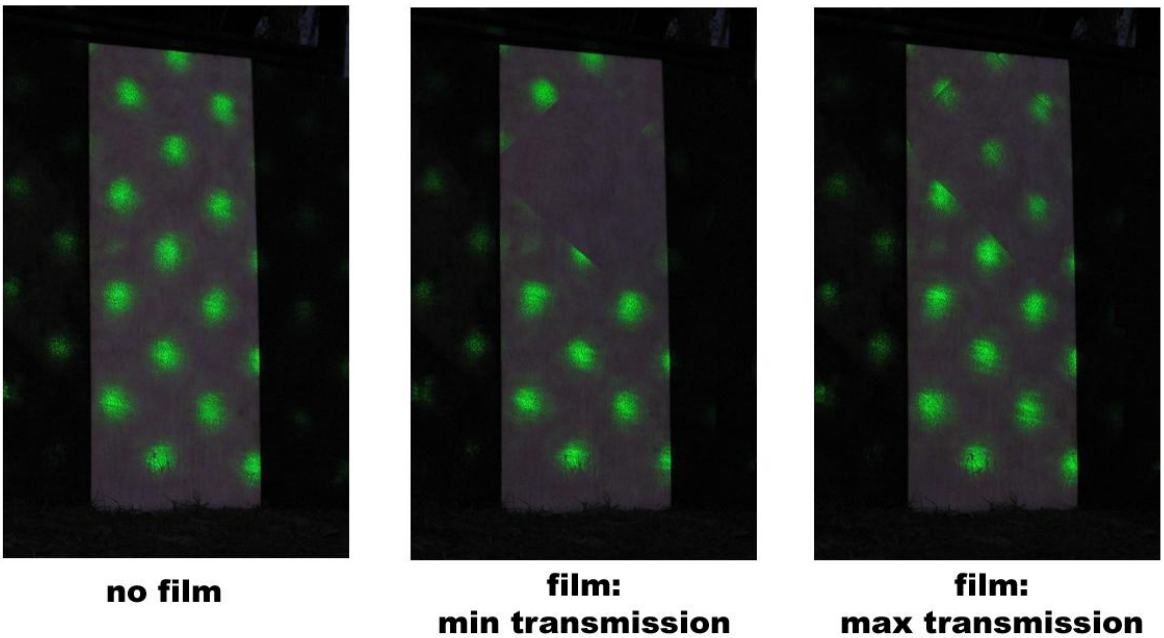

A B C

Figure 3-4. CATS beam polarization test. A) Effect of rotating linear polarizing film square is shown without attenuation, B) perpendicular to polarization axis and C) parallel to polarization axis.

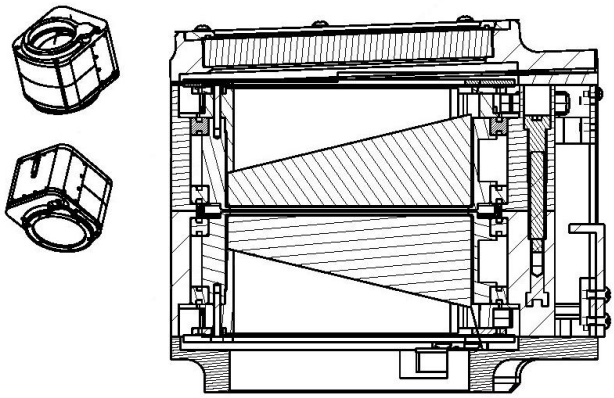

Figure 3-5. Isometric and cutout views of scanner head. The scanner window is tilted relative to the optical axis to minimize reflection of photon back into the receiver.

A B

Figure 3-6. Lab trials of scanner, showing A) line and B) rotating line scans.

A

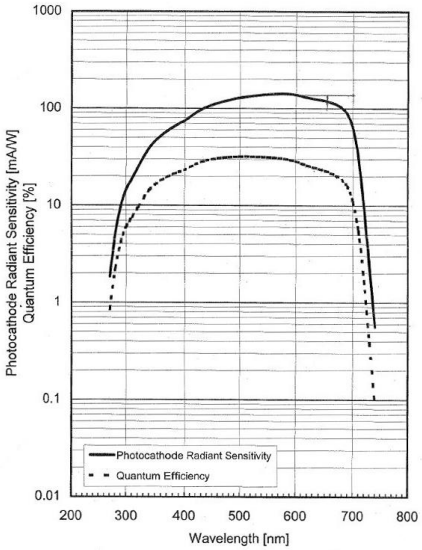

B

Figure 3-7. A) Photo of Hamamatsu Electronics Inc. model R4110U-74-M100D MCP-PMT and B) quantum efficiency curve.

Figure 3-8. Photos of the CATS and related components. A) View of sensor mounted on tripod with laptop and power supply components. B) Output window, enclosed scanner, electronics cube, enclosed optical components. C) Communications ports for laser and scanner operations. D) Communications ports for laser, timetag outputs, range data throughput. E) Front and F) back of scanner interface module.

Figure 3-9. Photo of several building structures in Lanham MD, where tests were conducted to observe the footprint of the CATS sensor. A brick wall and bank overhang are indicated.

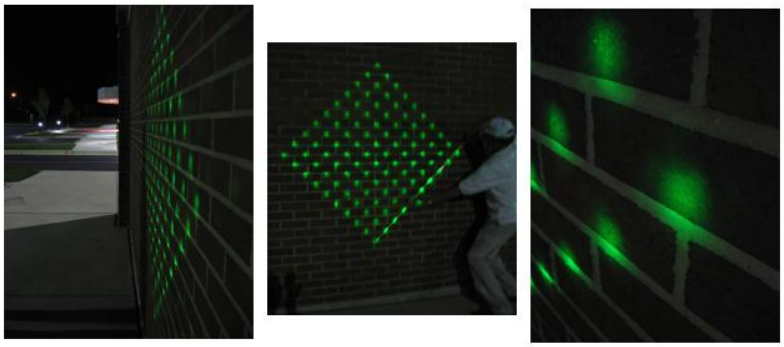

A B C

Figure 3-10. Footprint projected on a brick wall at a distance of 303.7570 m. A) Side view. B) Front view. C) Close up of four pixels.

CHAPTER 4
LSNR PERFORMANCE METRICS

Experimental results from the CATS prototype have yielded proof-of-concept LSNR operation and techniques for improving data processing related to system effects. Because the CATS is able to process multiple returns and has the ability to change sensitivity level between datasets, its penetration and noise reduction capabilities were assessed in a variety of different test setups.

There are a number of situations that can create difficulties for classic first / last return differentiation techniques. For example, Jutzi and Stilla describe sloped surfaces within the footprint of the beam leading to shifted mean distances, different elevated areas occurring at building walls leading to dilation and erosion, slightly different elevations leading to range superimposition, and small objects distributed randomly about a mean elevation value leading to a widened, low intensity pulse that is problematic for a fixed threshold analog system [55]. The ability of post-processing methods to overcome these difficulties in the LSNR case is dependent on measurable system properties. A number of experimental configurations were designed to investigate performance metrics for the CATS related to minimum separation distance, water penetration depth, and atmospheric backscatter [56].

Laser Ranging Concepts and Implementation

Range Calculation Fundamentals

In order to determine the range to a target, the two-way propagation delay of a laser pulse is measured. The ability of a ranging receiver to record multiple unique events, i.e. multiple canopy returns, is dependent on the length of the transmitted laser pulse. The pulse length contributes to a sensor's effective "blind zone," which refers to

a region after a registered return in which no subsequent returns can be detected [57]. The blind zone extent is determined largely by the light propagation speed c and the pulse length τ. In terms of estimated terrain resolution, this creates a distance below the initially reflecting object in which no other objects can be detected. For a 10 ns pulse length, the blind zone distance is,

$$c\tau = 10 \cdot 10^{-9}(s) \cdot 3 \cdot 10^{8}(m/s) = 300(cm). \tag{4-1}$$

The CATS sensor utilizes a short pulse length in comparison; approximately 480 picoseconds FWHM, which results in

$$c\tau = 480 \cdot 10^{-12}(s) \cdot 3 \cdot 10^{8}(m/s) = 14.4(cm). \tag{4-2}$$

Considering only pulse width restrictions, the instrument should be able to discriminate a distinct second object if it is 14.4 cm away from the first.

The overall resolution capability of a LIDAR system is not solely a function of transmitted pulse length, but rather the product of simultaneously occurring factors. Photodetector recovery time is another important element to consider. If the detector is not capable of a recovery faster than the amount of time related to the blind zone distance, the former will constrain the system specifications. The CATS photodetector, for example, has a recovery time of approximately 210 ps, which ensures that it is not the limiting factor.

Range Discretization

In the CATS, the laser pulse propagation delay is measured in discrete time intervals called range bins. A registered return is assigned a range bin number (RBN) based on the measured time since the transmission of the laser pulse. One of the

factors in the final range uncertainty is the length of the range bins used. This bin length is related to the effective range resolution.

To complement the sub-nanosecond pulse length of outgoing laser pulses, the internal system clock is set to 2 GHz. The range bin length is 1 / 2 GHz, or 0.5 ns. Accounting for the two-way travel time of the laser pulse, this makes the range resolution for consecutive single-photon events,

$$t_{res} = \frac{0.5 \cdot 10^{-9}(s) \cdot 3 \cdot 10^{8}(m/s)}{2} = 7.5(cm)\,. \tag{4-3}$$

In order to eliminate noise returns associated with backscatter as the laser pulse is just exiting the output window and to protect the PMT from being overexposed to returns from close proximity targets, a range gate is used to temporally filter responses. The range gate setting (RGS) is an offset to two-way travel time beyond the range gate value, in nanoseconds. The total two-way travel time and the related range are,

$$t_{2-way} = RGS \cdot 1 \cdot 10^{-9} + RBN \cdot 0.5 \cdot 10^{-9}\ (\mathrm{s})\,, \tag{4-4}$$

$$r_{1-way} = \frac{RGS \cdot 1 \cdot 10^{-9} + RBN \cdot 0.5 \cdot 10^{-9}}{2} \cdot 3 \cdot 10^{8}\ (\mathrm{m})\,.$$

Data Processing Fields

CATS range information is bundled into a binary file format with the .SPR extension. The raw files contain the following information about recorded returns:

- shot number
- channel number
- hit number
- range information
- time tag information

The first four fields are self-explanatory for the stream of data being recorded in a multi-element, multi-stop laser ranging system. The goal of the fifth field – global

positioning system (GPS) time tag information – is to reconcile the position of the scanner at any given time in relation to the temporal sequence of laser shots in a data set and Risley prism wedge index marks. Incorporating this data field allows for analysis of potential data flow problems, e.g. if the laser fire slaving system happens to miss synchronization pulses, or if scanner rotation is malfunctioning. Once correctly implemented, time tag information greatly aids in post-processing and potential troubleshooting. This idea is further developed in Appendix B.

Ground-based Static Testing

Experimental Setup

Practical testing of the instrument was conducted on the rooftop of a building in Lanham, MD—approximately 15 m tall. The sensor was mounted on a tripod with associated power and communications components (Fig. 3-8). The output window was pointed at buildings, vegetation, and other targets 200 to 800 m in the far field.

Initial data collections focused mainly on static pointing of the footprint, to measure standard deviation of measured ranges. Several attempts were made to range to nearby buildings. To establish static straightforward orientation of the laser footprint, the two prisms were set 180º out of phase so that the laser would be pointed straight along the optical axis of the transmit / receive path. C++ range processing code and MATLAB graphical capabilities were utilized to give a semi ‘real-time’ look at the limited data runs made on the rooftop in hopes that testing modifications could be made without incurring the delay of post-processing steps. PMT control software also provided a simple graphical output showing accumulated channel returns in a 10x10 intensity grid every second.

Range Accuracy

Ranging to a brick wall provided a calibration test for the consistency of returns per channel. Coding techniques for ranging are further explained in Appendix B, and the significance of a slight calculation error and oscillator variation is presented. The range gate value was incorrectly entered into software routines for the initial processing, so 40 m was later added to results to determine absolute range values. Relative measurements are still applicable, however. Hits were filtered for returns from 264 to 266 m to discard any noise returns not associated with scattering off the brick. The associated statistics and images are shown in Fig. 4-1.

At one standard deviation from the mean, 99% of the recorded range data falls within the 10 to 20 cm level. The outlier at channel 33 only registered 6 hits, a very small sample in relation to other channels. The distribution of channel hits, on the other hand, showed significant channel-to-channel deviation. The images in Fig. 4-2 show the orientation of the channels in the footprint, and the relative hit counts related to footprint geometry. In Fig. 4-2(A), hit counts are associated with height are plotted to emphasize variation in response levels. In Fig. 4-2(B), colors associated with these heights are more easily identified for spatial trends. Of note is that the bottom left row and far right row of channels are where most of the low hit count problems occur; this was theorized to be related to a problem aligning the reflected beamlets to the PMT anodes. Re-alignment procedures improved later ground-based data collections.

Minimum Separation Distance

In the case of a partially occluded laser beam, a multiple-stop receiver allows for recognition of multiple objects within the same laser shot. Given the 250 ps MCP-PMT recovery time and 0.5 ns (1 / 2 GHz) timing bins, it is expected that the "dead time" –

time before a subsequent multiple return can be registered – will be dominated by the 480 ps laser pulse width. More specifically, the system dead time should theoretically be limited primarily by the pulse width (14.4 cm in the atmosphere). Experiments were conducted to verify this value; the minimum separation distance (MSD) required to discriminate multiple scattering objects. Measurement of effective dead time establishes a boundary for sensor penetration.

A controlled experimental setup was developed for analysis of MSD in the situation where multiple hits would be necessary for target discrimination. The system was mounted on a tripod and pointed at the structures shown in Fig. 4-3. A 2 cm thick piece of sanded plywood was placed 1 m below a mirror approximately 560 m from the CATS to act as a calibration surface. At this distance, the 10x10 array of laser beamlets produced a rotated square footprint measuring approximately 2 m on one side. A central section of the large diamond-shaped array (shown reflecting off the chain-link fence in the background of Fig. 4-3) was intercepted by a cardboard mask. A square hole in the mask allowed transmission of only four beamlets to a 45º turning mirror located behind the cardboard. The mirror redirected the beamlets from the horizontal propagation direction to the vertical, and onto reflecting surfaces below.

The cardboard mask assisted in channel discrimination. Returns from the mask were filtered out (temporally), allowing for post-processing analysis to more easily identify desired signal responses. Half of a beamlet cross-section was projected onto the wood calibration surface, and the other half projected at a varying distance above on a similarly reflective wood sheet. Fig. 4-4 illustrates the intercepted surfaces.

Seven ranging trials (A-G) were conducted at various separation distances (Actual Separation column in Table 4-1). Data was recorded for 10,000 laser shots (1.25 sec) in each trial. Returns were filtered for a coarse 5 m window around the central response to include contributions from atmospheric returns near the primary reflecting surface. The return signal at the calibration surface (0 cm separation) was approximately two range bins wide—as expected for 0.5 ns timing bins, 480 ps pulse width, and a flat optical cross-section. Data was thus retained for laser shots reporting three or more total intra-shot returns, as hits beyond the second return were potentially secondary surface returns. For each laser shot, the differential range bin value (RBV) between the first and last hit was calculated to identify the secondary surface distance, shown in Fig. 4-5 plots. The analysis process for trial D is described here. In Fig. 4-5(A), large (>10 RBV) data values occur sparsely, meaning that they represent atmospheric returns. These peaks resulting from 3+ return shots account for less than 5% of the total data in trial D. Conversely, small (<5 RBV) data values occur frequently and at a consistent level, meaning that they represent secondary surface returns.

In Fig. 4-5(B), the differentials were accumulated into a total count per range bin distance (AD) and displayed in a histogram. The third column (Reported Separation) in Table 4-1 was generated from the peak histogram value in each trial. The fourth column in Table 4-1 shows the error in secondary surface measurement for each trial. Results from trial A (zero separation) are included to show that a single target produces a signal response less than three returns wide. The 2.6% of shots reporting multiple hits with 3 or more returns in this trial are attributed to atmospheric scattering. Increasing the separation of the two surfaces beyond 10 cm, as in trial B, begins to

produce significant (non-atmospheric) multiple returns. Because the resolution limit of the timing electronics is 2 GHz, the smallest surface that can be detected is the nearest range bin edge, or 15 cm resolution.

Though the timing oscillator is expected to be stable about 2 GHz, it is possible that the central frequency drifts over time with extended system usage. The significance of potential drift is further explored in Appendix B. In order to evaluate this empirically, the error values in Table 4-1 were calculated for known target separations. To determine a systemic range bias, the effect of imposing a constant offset on range estimation was tested. Table 4-2 shows analysis of four values of range bias in each trial—5, 4, 3, and 2 cm. The values in each column are calculated by taking the absolute value of the Reported Separation (RS) and Actual Separation (AS) difference in each trial. The average error for each offset is then calculated.

Analysis of distributed returns allows for identification of ground reflections under dense foliage and penetration past the water surface. Given CATS receiver specifications, dead time is theoretically limited primarily by laser pulse width. Assuming that the PMT is not saturated by the return pulse and that the intercepted cross-section is not vertically elongated, experiments show that a secondary surface can be detected at a distance of 15 cm from the first. Range errors in secondary surface identification for six separate trials were within 7.5 cm, or within the timing resolution limit of the system. Systemic bias testing showed that an offset of 4 cm minimized the average error in secondary surface measurement (down to 1.3 cm).

Crosstalk Evaluation

In the CATS, backscattered radiation from a 10x10 square of beamlets is imaged onto an equally spaced grid of photocathode material. Photoelectric events amplified

from each grid section are collected by separate anodes. Because all of the sub-beamlets are transmitted at once, the MCP-PMT must be capable of simultaneous sensing over each element in its grid. It is expected that each anode response will provide unique XY position information about intra-footprint responses. The spatial resolution of the system with regards to a single photon event is dependent on its ability to accurately register independent responses from individual anodes. A concern in adopting this type of detector structure is the influence of crosstalk on recorded observations.

Multi-anode PMT designs are commercially available with the following geometric plate layout: squares of photosensitive material associated with each anode are separated by narrow borders of non-conductive material in a single plate. Fig. 4-6 shows the output profile of a multi-anode MCP-PMT when a light spot of approximately 20 μm diameter is scanned across the plate.

Light incident on a singular portion of the photocathode material may produce a response at an adjacent anode—crosstalk between anodes. The overlapping regions of the waveforms in Fig. 4-6 are crosstalk areas. The amount of crosstalk between adjacent anodes of the photomultiplier tube contributes to the uncertainty of resolving a single return at the specified spatial resolution. This can result from broadening of electron flow when light is converted into electrons, or incident light spread within the faceplate. Testing of two types of Hamamatsu R5900 series photomultiplier tubes showed fairly low (~5%) nearest-neighbor crosstalk and even lower (1%) next-nearest-neighbor measurements [58]. These experiments indicated that crosstalk is mainly due to the spreading of optical photons in the entrance window; the M64 PMT used had a

1.3 mm thick glass entrance window. Reduction in window thickness to 0.8 mm further reduced inter-channel crosstalk. In comparison, the R4110U model PMT used in the CATS system has a 4.77 mm thick window; the observed crosstalk for this device may thus be higher than 5%.

The contributions from overlapping waveforms can be mitigated by restricting the area of focused energy. In the CATS, a lens in the transmit path is shimmed to increase the amount of defocus and resulting angular divergence of laser spots in the far field. The spot sizes then have 77% linear fill factor, or 46% area fill factor. A typical CATS pixel energy distribution is shown in Fig. 4-7. The teal contour line (and superimposed dotted circle) corresponds to 50% of the peak amplitude (FWHM). The blue line is the 2σ contour, or 95% of the total energy. Focusing backscattered energy to a smaller area on the active photocathode has the potential to reduce crosstalk, but can also reduce the effective lifetime of the tube.

In order to practically evaluate crosstalk contributions in the CATS, the setup pictured in Fig. 4-8 was created. Four pixels of the footprint were masked to create temporal spacing in receiver returns between pixels outside the central square. Pixels 19, 20, 23, and 24 were isolated for this experiment. For each laser pulse, returns were filtered temporally for a 5 ns window centered on the wood signal response. This separates any possible stray returns from the mask. Of the 8 surrounding pixels, 5 channels are considered to get a measure of pixel-to-pixel crosstalk. For example, channels 18, 22, 30, 31, and 32 are considered in the channel 19 crosstalk analyses. The contributions from these channels are labeled as a_{18}-a_{32} in Table 4-3 to express geometric relation within the CATS footprint (Fig. 4-9).

An experiment was first performed for multi-photon sensitivity (2300 V supply), or approximately $2 \cdot 10^5$ gain. The dark noise count at this gain is expected to be 119 counts per second (cps). Over 10,000 shots or 1.3 seconds of data, on average 25,000 returns were registered for each signal pixel (2-3 hits per shot). Each surrounding non-signal pixel registered on average 150 returns. This is close to the dark noise specification at this gain. Hits from channels $a_{18} – a_{32}$ were accumulated and divided by the number of total non-signal pixels (5). This value was 0.17% of the accumulated hits from channel 19 (100% level). Average crosstalk at the other three channels was calculated as the following: channel 20- 0.62%, channel 23- 0.22%, and channel 24- 0.65%. For multi-photon sensitivity, crosstalk between receiver channels is small relative to MCP-PMT design specifications (3.80%).

The same analysis was performed for single photon sensitivity (2500 V supply), or approximately $8 \cdot 10^5$ gain. Over 10,000 shots or 1.3 seconds of data, on average 45,000 returns were registered for each signal pixel (4-5 hits per shot). Each surrounding non-signal pixel registered on average 5,000 returns. This is an order of magnitude larger than the expected dark noise level at this gain, so channel crosstalk is assumed to have significant effect here. The accumulated hits from $a_{18} – a_{32}$ in this case were on average 12.22% of the accumulated hits from channel 19 (100% level). Crosstalk at the other three channels was calculated as the following: channel 14- 7.24%; channel 22- 15.39%; and channel 23- 9.96%. For single-photon sensitivity, the measured crosstalk is in some cases nearly four times as large as PMT specifications (3.80%).

Because of the large disparity between values – for example, channel 22 exhibited more than two times the amount of crosstalk than channel 14 – it was expected that sub-pixel backscatter was not properly aligned to the PMT grid. Even a very slight (0.1 mm) offset in the tube alignment can cause one channel in the grid to receive significantly more light than a neighboring channel. Re-alignment procedures were carried out to ensure that the backscatter was being uniformly projected on the grid before conducting airborne testing.

Water Penetration Depth

The potential for bathymetric mapping of near-shore waters was evaluated by recording ranges through water columns of variable depth. To gauge the signal response in a wide breadth of bathymetric scenarios, the optical clarity of tested waters was also altered.

A 55 gallon, 90 cm tall barrel was placed below a turning mirror so that four pixels of the CATS footprint were distributed down into the barrel (Fig. 4-10(A)). With the barrel filled with 90 cm of distilled water, the barrel bottom (painted white for optimal reflectivity) was clearly visible to the human eye. A 180º backscatter turbidimeter (infrared) reported an average value of 1.5 nephelometric turbidity units (NTU) for this sample. The barrel was also filled with natural water transported from the Gulf Coast. This salt water was skimmed off the top of a near shore area. The turbidity of the sample was measured at 18.6 NTU. The white barrel bottom was no longer visible to the eye at a depth of 43 cm.

Measurements were performed at night to aid in positioning of the 10x10 footprint on the cardboard mask / large turning mirror shown in Fig. 4-8. During the day, the laser reflections were sufficiently weak at 600 m that they were not visible to the naked

eye; meaning that precise positioning of a single channel down through a water column, for example, was not possible. Operating at night did have the benefit of reducing potential solar events in these trials, but previous experiments have shown that daytime operation has minimal effect on SNR for wood surfaces at 550 m.

Because the location of the barrel bottom was precisely known – 60 cm water column depth – for this experiment, a narrow range window corresponding to ± 3 bins around the expected response was chosen. This made it possible to accumulate a history of returns related exclusively to the barrel bottom response, rather than including sporadic returns from the water column and potential noise events (by using a wide range window). For each laser shot in the accumulated return history, data from a selected channel corresponding to a beamlet projected down into the barrel was considered only within the narrow range window. For example, if on average 70% of the transmitted laser shots registered one or more signal events from the barrel bottom, this means that 300 out of a total 1000 accumulated laser shots did not register at least one hit within the selected window.

For 60 cm of this clear water, on average 97% of the transmitted laser shots registered one or more signal events from the barrel bottom. Estimating the beam attenuation coefficient from this data and extrapolating the signal intensity to further depths, it is expected that approximately 90% of the incoming beamlets would register a signal event at 5 m. Likewise, at a depth of 50 cm in coastal water, on average 12% of shots registered at least one signal event. Extrapolation of experimental results to further depths leads to the suggestion that this is a sufficient signal level to produce meter-scale shallow (2 to 5 m depth) bathymetry data [56].

A 22.7 kg bag of sand was poured into distilled water. Data was collected while silica particulate was settling down into the water column. This was a heavily turbid suspension; visibility to the eye was approximately 7.5 cm. Histograms from a data window of 10,000 laser shots are shown in Fig. 4-11 for three different supply voltages. The blue and red signals are spaced approximately 15 range bins peak-to-peak; close to the height of the water column after accounting for the change in the index of refraction. The blue signal is thus associated with the water surface return, the green from the middle of the column, and the red from the bottom of the barrel. A plot of all four channels merged together (left image) and a single channel (right image) are shown to illustrate response consistency.

Although detection of small low reflectivity targets submerged in highly turbid waters may be difficult, the density of data points from the sea bottom given 20 cm pixel spacing should be sufficient to establish near-shore depths (up to 5 m) at coarser spatial resolution (1 m scale). For example, if the signal strength at 5 m degrades such that 4% of the pixels within a footprint produce ocean bottom returns, a 600 m flying height, 8 kHz laser rep rate, and 60 m/s platform velocity is enough to reconstruct the digital terrain model at 1 m grid spacing. Partially submerged targets with intercepted cross-sections smaller than 0.25 m^2, however, may not be detected. Additionally, for the heavily turbid case, the multi-photon state (2300 V or $2.5 \cdot 10^5$) was not sufficient for feature identification. Extraction of the bottom signal in a heavily turbid suspension necessitated maximum MCP-PMT gain (2500 V or $8 \cdot 10^5$).

Multi- vs. Single-Photon Sensitivity

Varying levels of photomultiplier tube sensitivity were assessed to weigh noise production versus variations in supply voltage. For example, Fig. 4-12 displays stacked

histograms of accumulated atmospheric events per channel for a 1.25 second data capture. Changing the supply voltage from a multi-photon state (blue) to a single-photon state (red) drastically affected the recorded number of atmospheric scattering events across most channels.

Atmospheric backscatter as a result of laser light propagating through an 8 μs range gate and sky irradiance was measured. The sensor output window was pointed towards the sky on a clear day and returns recorded for the duration of the range gate. This procedure was repeated for three different PMT voltages, or gain settings of $2.5 \cdot 10^5$, $3.5 \cdot 10^5$, and $8 \cdot 10^5$. Fig 4-13(A) displays results from all channels combined, and Fig. 4-13(B) displays results from one channel. Blue colored bins correspond to events early on in the gate, and red to events near the end. There were significantly more events recorded early in the range gate at the single photon level; the theorized cause was a switching problem related to the high voltage supply. The majority of the gate showed a fairly constant level of returns, however.

The contributions from laser light / diffuse solar irradiance scattering by atmospheric particulate and direct solar irradiance were significantly increased for the central 32 channels as gain increased toward a single photoelectron threshold. This was an expected result as atmospheric events are generally single photon events, and reaching a single photon threshold required full gain ($8 \cdot 10^5$). On average, the quantity of recorded returns increased by a factor of about 70 by increasing the gain from $2.5 \cdot 10^5$ to $8 \cdot 10^5$.

The CATS offers the capability to change the PMT supply voltage between experimental collections. Operating at multi-photon sensitivity may have value for

situations in which high ambient noise precludes single-photon sensitivity, as man-made objects such as buildings features may be easily distinguishable even at lower gain ($2.5 \cdot 10^5$). This idea is explored in the following sections describing scan results. It is expected that operating at high gain ($8 \cdot 10^5$) will produce the best fine-scale resolution and foliage/water penetration, but large amounts of noise can obscure some features. Decreasing PMT gain may then provide higher contrast between signal and noise for highly reflective features.

Ground-based Scan Testing

Horizontal Scan – Building Features

Early attempts at creating a three-dimensional image from range and timetag information are chronicled in Appendix B. Diagnostic signal analysis allowed for identification of mechanical problems such as a cracked encoder plate. After rectifying these issues, point cloud generation aided by diagnostic tools based on time histories has produced significantly cleaner point clouds. With scan motion set to project a horizontal line pattern, the CATS was run for 30 seconds. Post-processing of returns yielded the point cloud shown in the top left of Fig. 4-14. The footprint shape reflected off the main scattering surface is prominently shown across the solid brick building face. Metal light poles located approximately 10 m in front of the building are also discernable from the building front. Noise events occurring throughout the scan are easily separated from the bulk of signal returns.

Rotating Line Scan – Building Features

Data from a rotating line scan (shown in Fig. 3-6) was collected to produce a larger three-dimensional view of the same building. A top view of the resulting point cloud in Fig. 4-15 is shown for 9 seconds of scan data (approximately 72000 laser shots). An

isometric view of the same scene is shown in Fig. 4-16. This data was collected with a 2100 V PMT supply voltage.

Raising the voltage level on the PMT to 2200 V produced the expected result of a larger variety of distinguishable fine features at the cost of more noise returns. This is shown in Figs. 4-17 and 4-18. Tree structure is also visible in Fig. 4-19. During this data collection, there were semi-occlusions as a result of leaves; points on the building face were discernable through the spaces between tree trunks / branches.

Rotating Line Scan – Building Features (Partial Obscuration)

Test scans of a building with heavy vegetation obstructions occluding the building (Fig. 4-20) yielded the large point cloud shown in Fig. 4-21. A top view of the cloud is plotted here using the QTModeler software package and colored according to elevation. To get a better idea of the sensor response from building faces and objects directly in front of the building, points were filtered for a 3 m elevation window in this region. The results, shown in Figs. 4-22 and 4-23, depict features more clearly. Here we see range "tails" associated with strong responses from highly reflective surfaces. While these can pose a serious problem for automated imagery generation and display, such effects may be beneficially exploited. Isolated dark noise points do not exhibit the same type of geometrically organized response. The deconvolution algorithm employed in the MIT Jigsaw system, for example, eliminates these responses while simultaneously enhancing SNR [54].

Fig. 4-24(A) shows a photo near the building and further zoom-in on the isometric cloud view. Here we see small bushes, narrow tree trunks, and a white stone bench. In Fig. 4-24(B), the white stone surface is the most highly reflective and produces the most returns; the geometry of the small top arch is discernable. The dark tree bark is also

highly reflective. There is a significant difference between the number of the returns from the trunks and the dense small bushes. The system demonstrates in this case the potential to separate the trunk and foliage features.

Expanding the points filter to 5 m elevation shows penetration through the heavy tree foliage. Fig. 4-25 shows top and side views of the point cloud colored by elevation. In this case red points correspond to leaf returns close to 5 m, and orange points correspond to leaf and roof returns close to 4 m. The system is unable to define much of the roof structure due to almost total obscuration by the dense vegetation in this case.

UFL_Steady_RangeCal_24.SPR

<u>Statistics</u>

# of shots fired: 16000

total # of hits in file: 279197

# of channel error hits: 0

# of non-error hits: 1279197

total # of filtered hits: 922202 (72% of total)

average hits per shot for all hits: 79.9498

average hits per shot for filtered data: 57.6376

averaged range to target, all channels: 265.1215

A

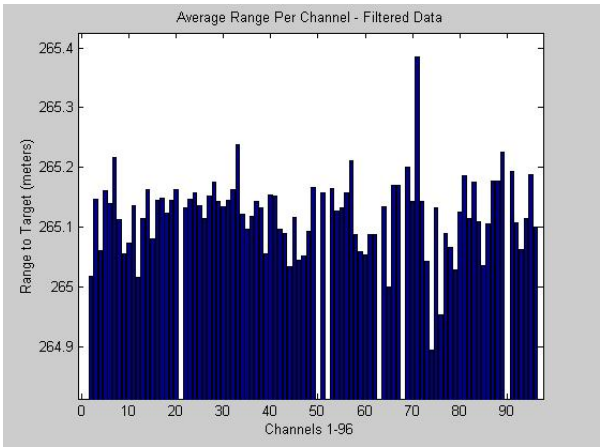

C

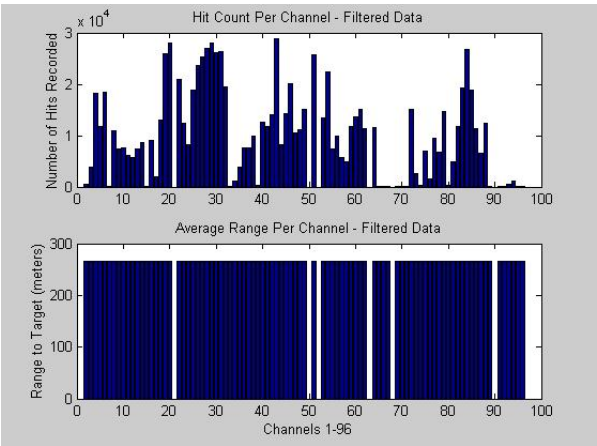

B

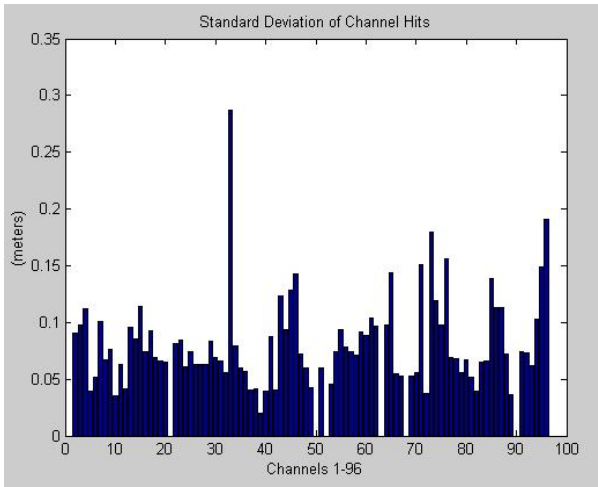

D

Figure 4-1. CATS static (no scan) returns analysis from a brick wall approximately 300 m from the instrument. A) Statistics from calibration test. B) Histograms related to hit count per channel and average range per channel. C) Average range per channel, zoom-in. D) Standard deviation of recorded ranges per channel.

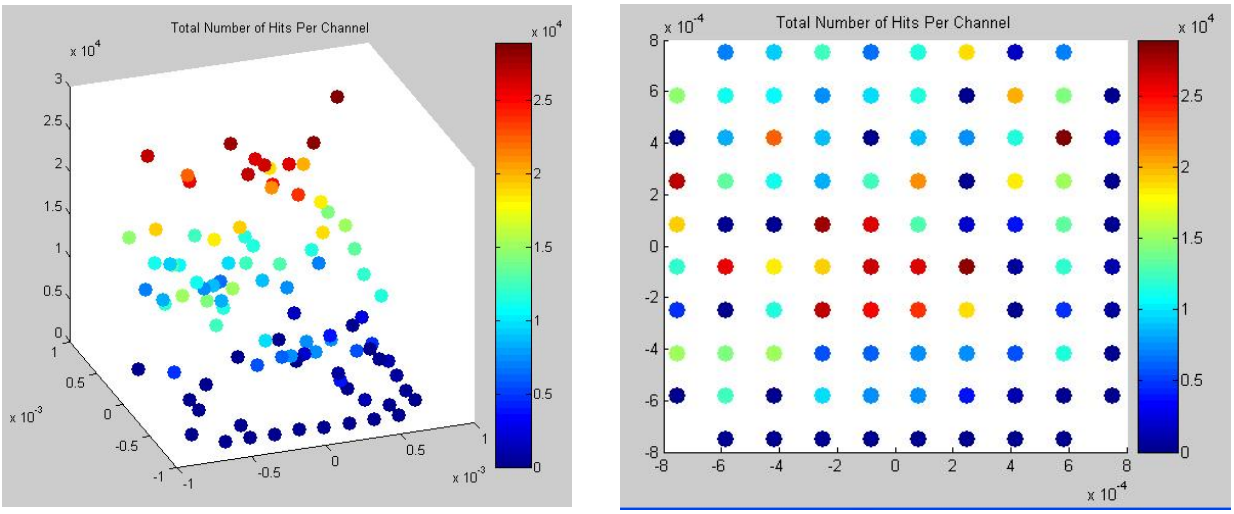

A B

Figure 4-2. Relative accumulated hit counts per channel for a CATS range calibration test. A) Hits are associated with height and plotted to emphasize variation in response levels. B) Colors associated with these heights are more easily identified for spatial trends.

Figure 4-3. CATS static footprint test setup. A 45º turning mirror deflects four central pixels onto reflecting surfaces below. The pixels immediately surrounding these four are masked by cardboard to aid in channel discrimination. half of one pixel -- channel 15 -- is distributed on the wood calibration surface, and the other half is distributed 11 cm above on a wood sheet.

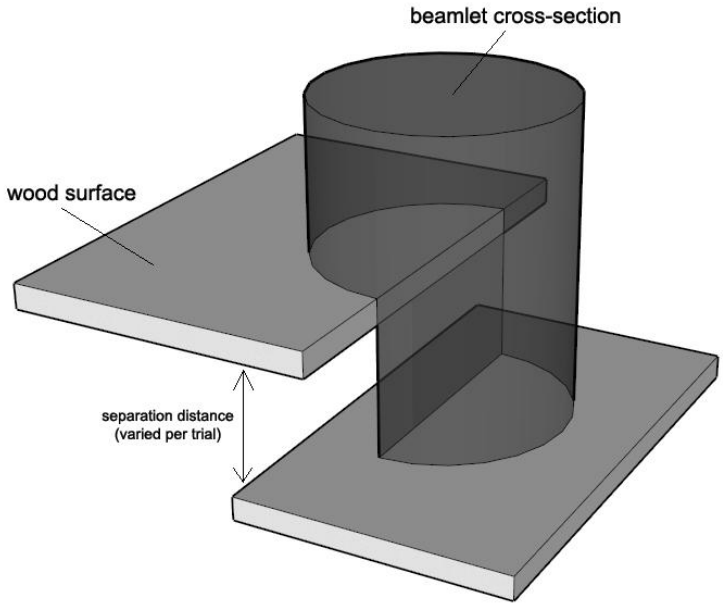

Figure 4-4. Illustration of beamlet cross-section projected onto wood surfaces.

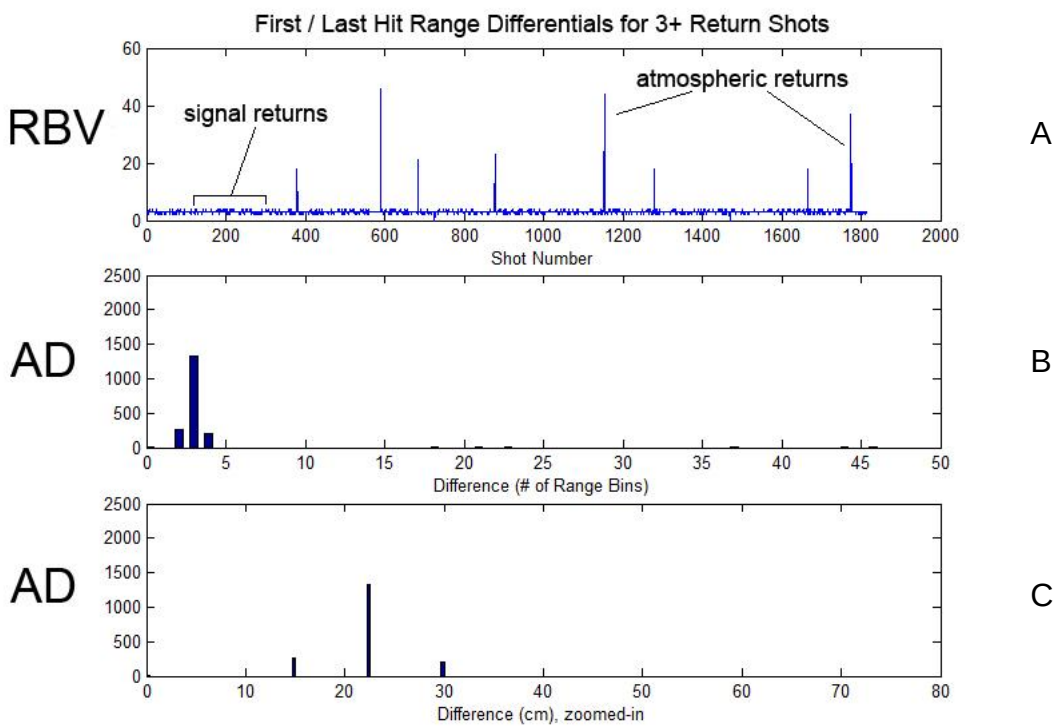

Figure 4-5. Calculation of reported separation for 19 cm distance between multiple scattering surfaces (trial D). A) Range bin value (RBV) difference between first and last returns is plotted on the y-axis versus shot number on the x-axis. B) Histogram of accumulated differentials (AD). C) Histogram of accumulated differentials, zoom-in.

Table 4-1. Ranging trials for shots reporting 3+ returns

Trial	Actual Separation (cm)	Reported Separation (cm)	Error (cm)	# of Multiple Hit Shots	% of Total Shots
A	0	n/a	n/a	259	2.6
B	11.0	15.0	4.0	2094	29.4
C	14.0	15.0	1.0	2435	24.4
D	19.0	22.5	3.5	1815	18.2
E	24.0	30.0	6.0	831	8.3
F	31.0	37.5	6.5	2112	21.1
G	41.0	45.0	4.0	1471	14.7

Table 4-2. Effect of range bias offset on measurement error (in cm)

Trial	|RS-AS|	|(RS-5)-AS|	|(RS-4)-AS|	|(RS-3)-AS|	|(RS-2)-AS|
A	n/a	n/a	n/a	n/a	n/a
B	4.0	1.0	0	1.0	2.0
C	1.0	4.0	3.0	2.0	1.0
D	3.5	1.5	0.5	0.5	1.5
E	6.0	1.0	2.0	3.0	4.0
F	6.5	1.5	2.5	3.5	4.5
G	5.0	1.0	0	1.0	2.0
average error	**4.3**	**1.7**	**1.3**	**1.8**	**2.5**

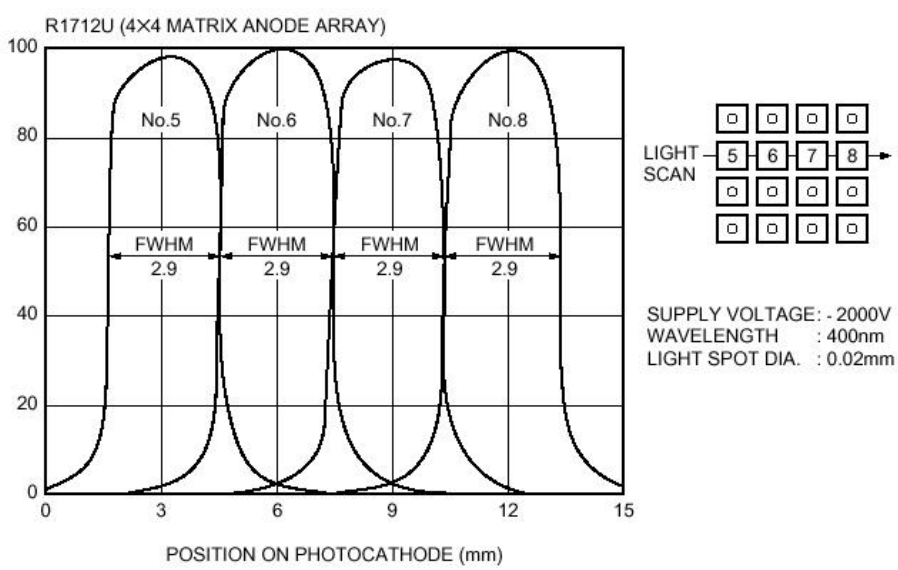

Figure 4-6. Output profile of multi-anode MCP-PMT when a light spot of approximately 20 µm diameter is scanned across the photocathode active areas (1.4 x 1.4 mm squares) [50].

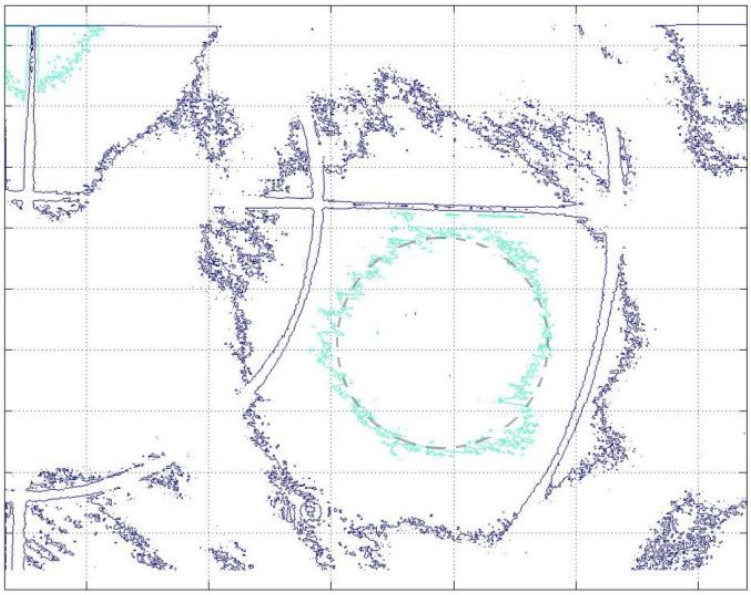

Figure 4-7. Contour map of beam energy for a single pixel. The inner contour is indicated by a dashed circle. Edges of neighboring pixel energy patterns are also visible in the image corners.

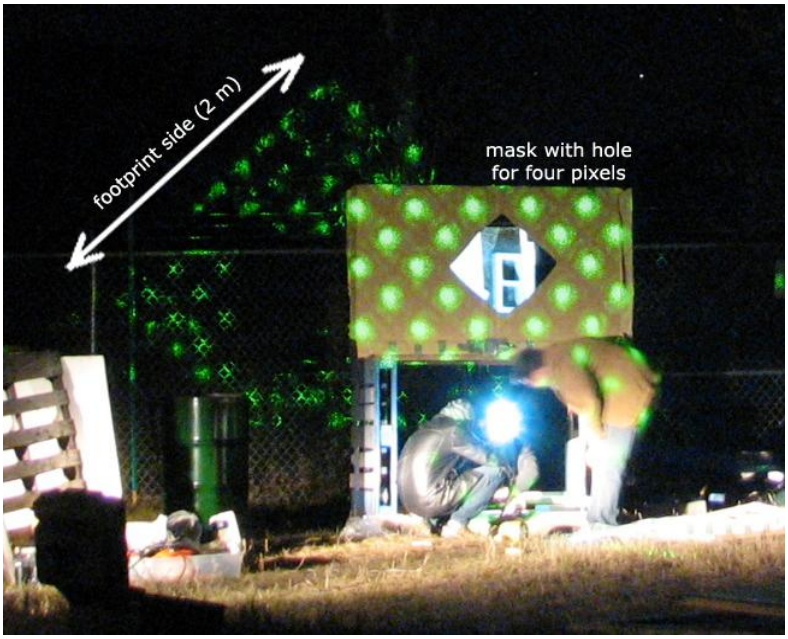

Figure 4-8. CATS static footprint test setup. A 45º turning mirror approximately 560 m from the sensor deflects four central pixels onto a wood sheet used as a calibration surface. The pixels immediately surrounding these four are masked by cardboard to evaluate crosstalk of returns from the four pixels.

Table 4-3. Channel orientations for crosstalk calculations

a_{30}	a_{18}	a_{22}
a_{31}	100%	X
a_{32}	X	X

Channel 19

a_{18}	a_{22}	a_{14}
X	100%	a_{15}
X	X	a_{16}

Channel 23

a_8	X	X
a_7	100%	X
a_6	a_{32}	a_{31}

Channel 20

X	X	a_{15}
X	100%	a_{16}
a_7	a_8	a_{54}

Channel 24

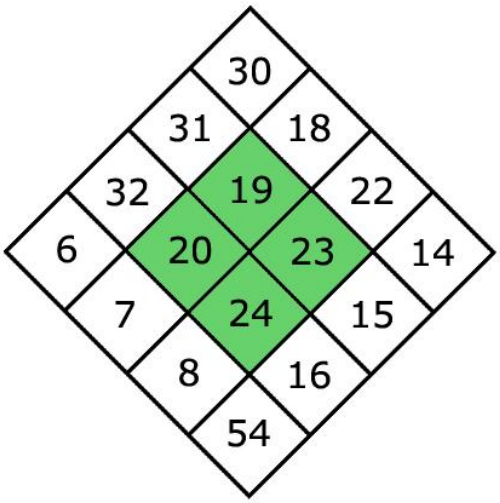

Figure 4-9. Geometric orientation of isolated pixels (shaded central four) in CATS footprint.

A

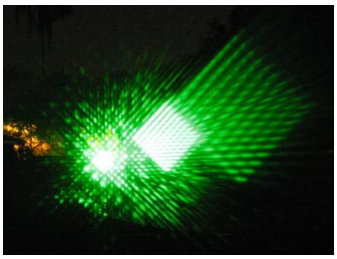

B

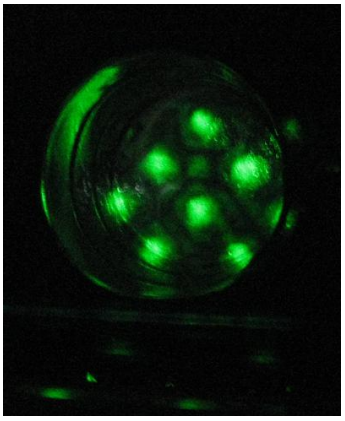

C

Figure 4-10. Photos of CATS barrel testing. A) A 55 gallon barrel filled with water of variable constituency is placed below a 45º turning mirror. B) Beam propagation through 560 m. C) Four pixels are reflected down into the barrel by the mirror.

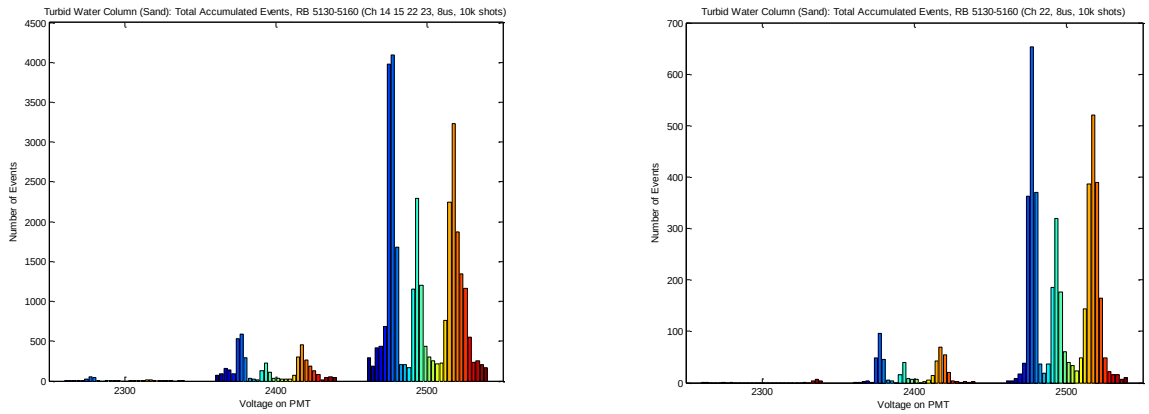

A B

Figure 4-11. Histograms illustrating accumulated signal events for a heavily turbid water-sand solution. Blue colored bins correspond to expected water surface returns, green to middle of the column, and red to the bottom of the barrel. A) Returns from four barrel channels combined. B) Returns from channel 22 only.

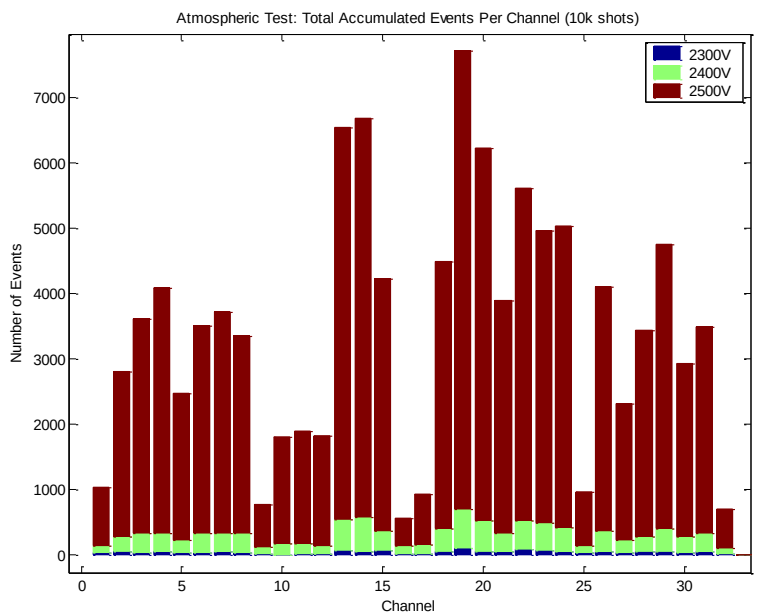

Figure 4-12. Stacked histograms depicting accumulated atmospheric events per channel at three different PMT supply voltages.

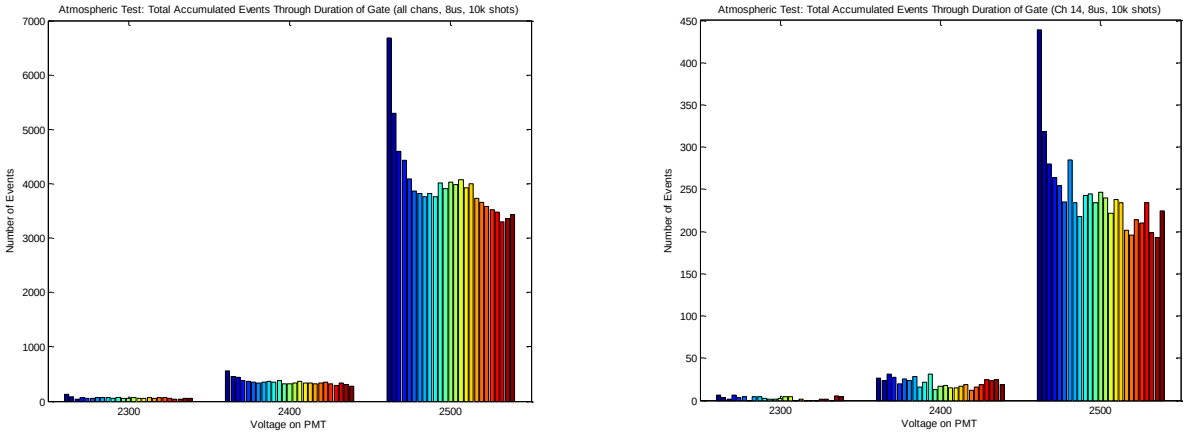

A B

Figure 4-13. Histograms depicting the consistency of accumulated events through the duration of an 8 μs range gate for three different PMT supply voltages. Blue colored bins correspond to events early on in the gate, and red to events near the end. A) Returns from all channels combined. B) Returns from channel 14 only.

Figure 4-14. Point cloud (green) resulting from CATS horizontal scan after timetag structure modification. The sensor was situated on rooftop approximately 300 m from building.

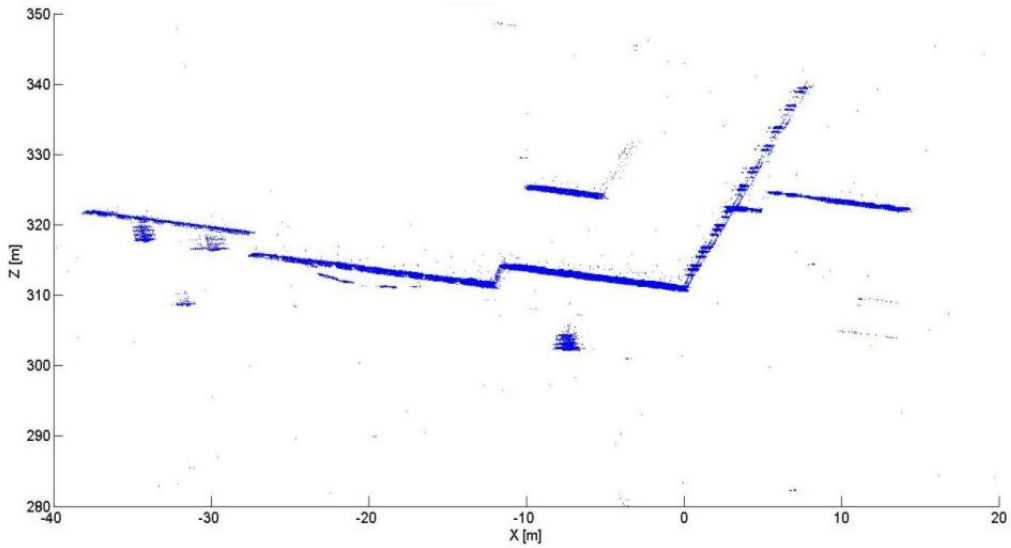

Figure 4-15. Top view of point cloud generated from rotating line scan data at 2100 V.

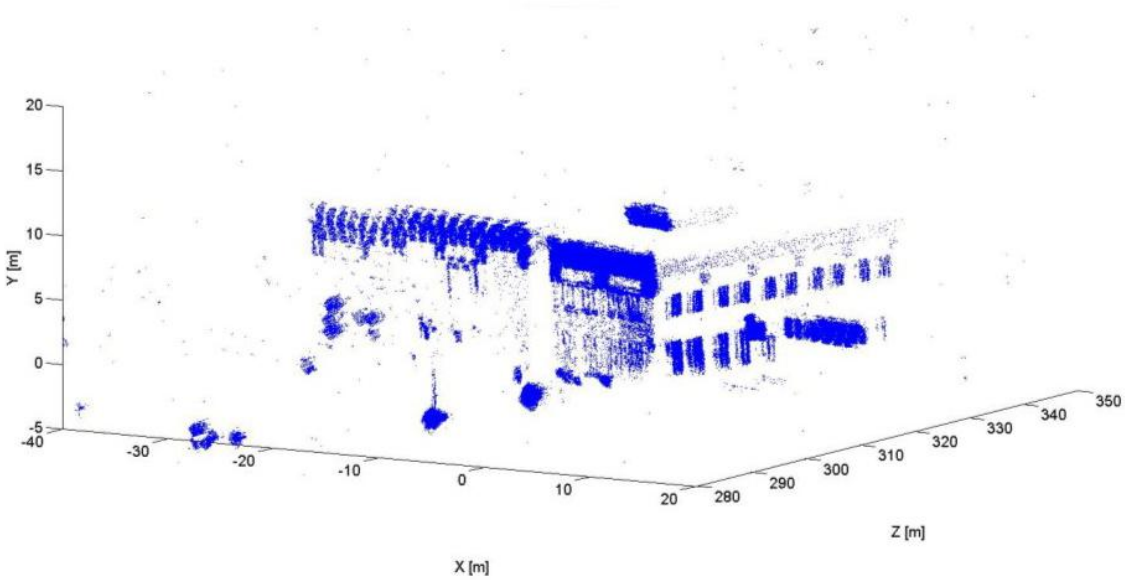

Figure 4-16. Isometric view of point cloud generated from rotating line scan data at 2100 V.

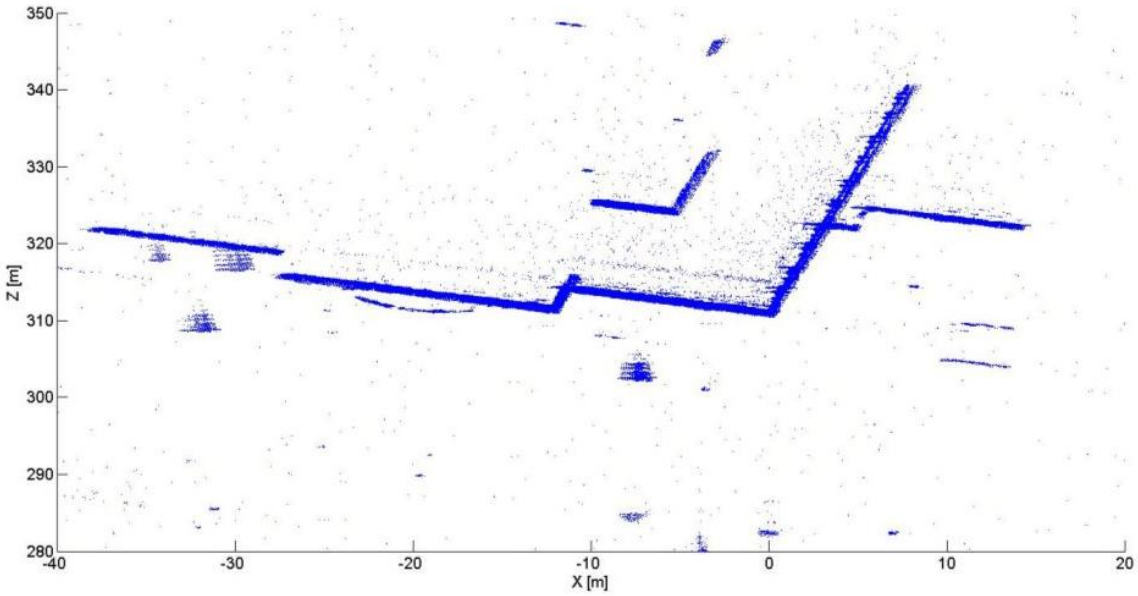

Figure 4-17. Top view of point cloud generated from rotating line scan data at 2200 V.

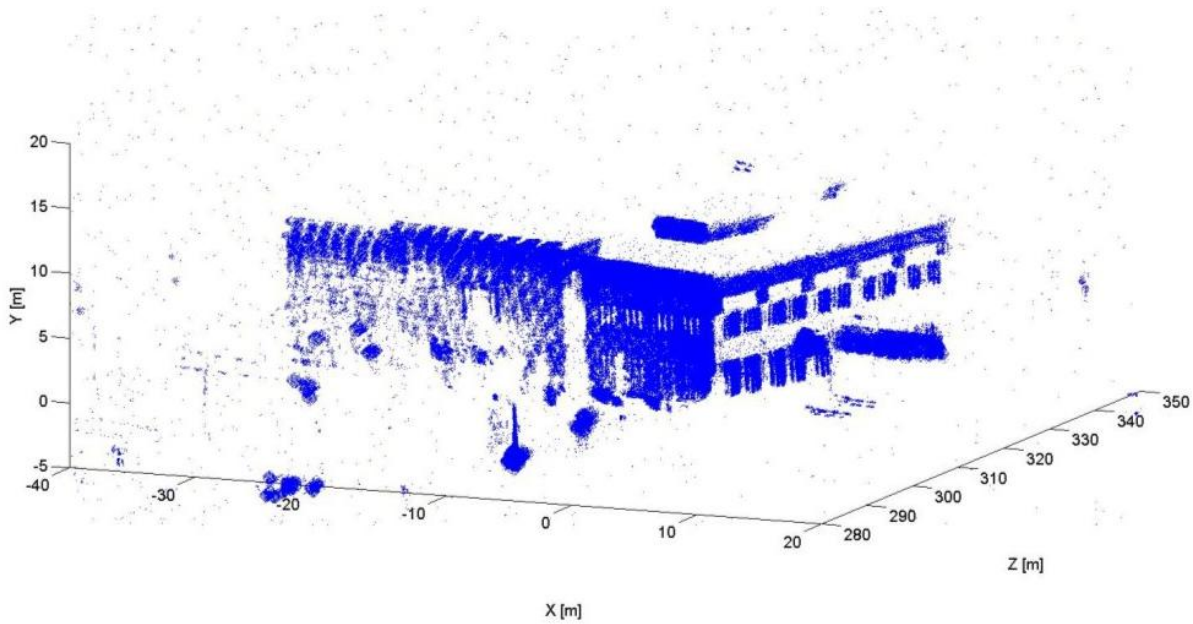

Figure 4-18. Isometric view of point cloud generated from rotating line scan data at 2200 V.

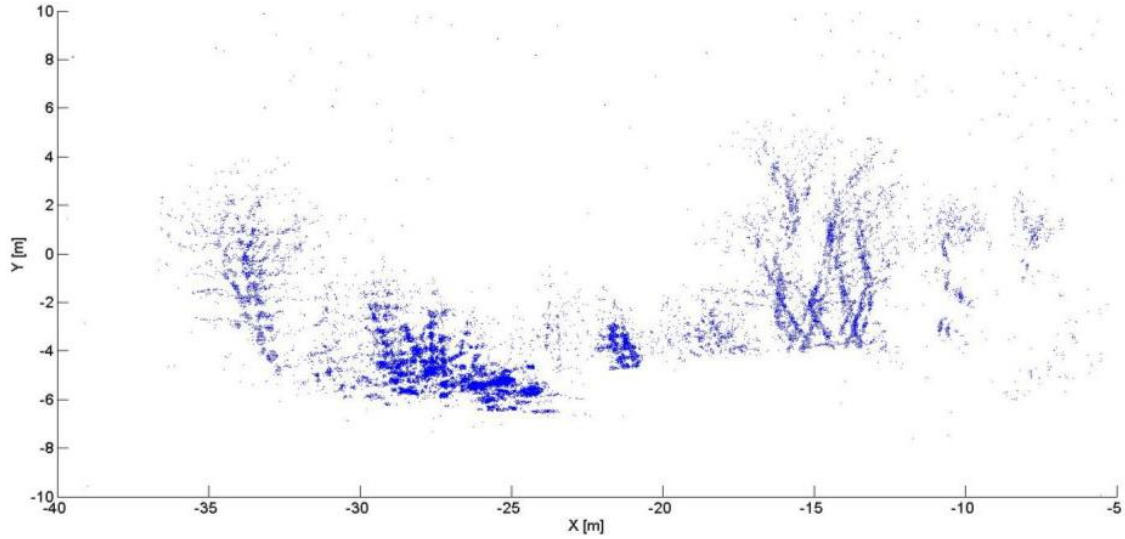

Figure 4-19. Front view of point cloud generated from rotating line scan data at 2200 V, zoom-in of tree structure.

Figure 4-20. Photograph (front view) of a building with a large number of nearby trees.

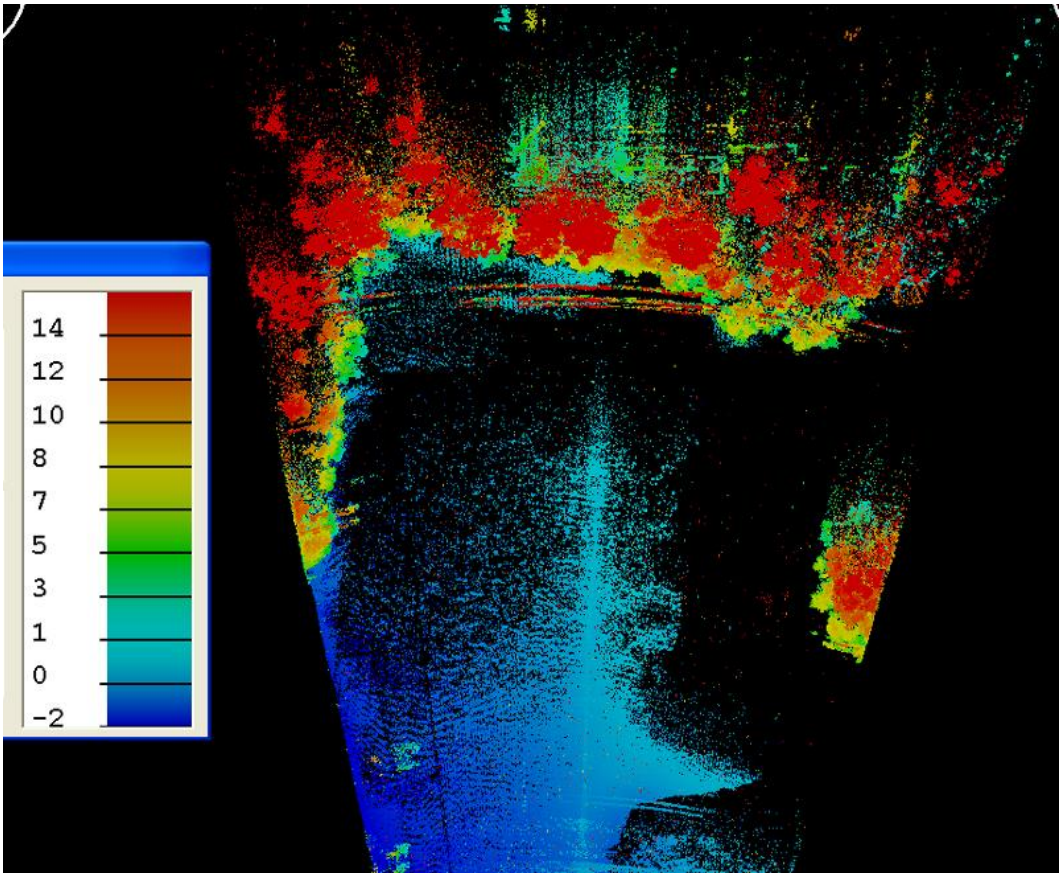

Figure 4-21. Overhead view of large point cloud generated from the building with heavy tree obstruction. Data was colored according to height (m) using QTModeler software. Dark blue points correspond to the low slope of the grassy field leading up to the building. Dark red points correspond to the tops of the trees directly in front of the building.

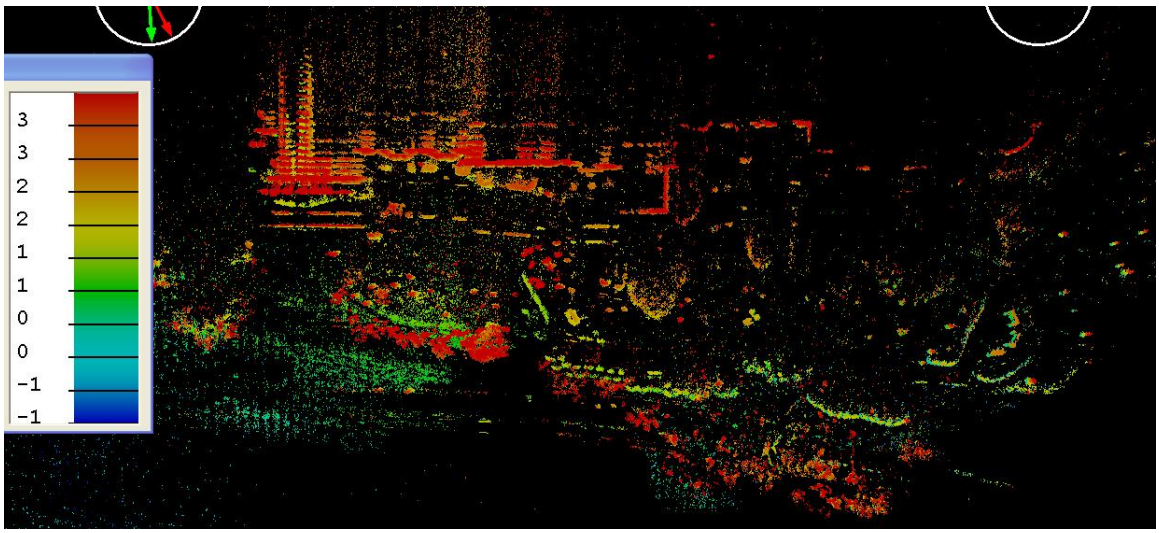

Figure 4-22. Overhead or top view of 0-3 m data segment associated with building location.

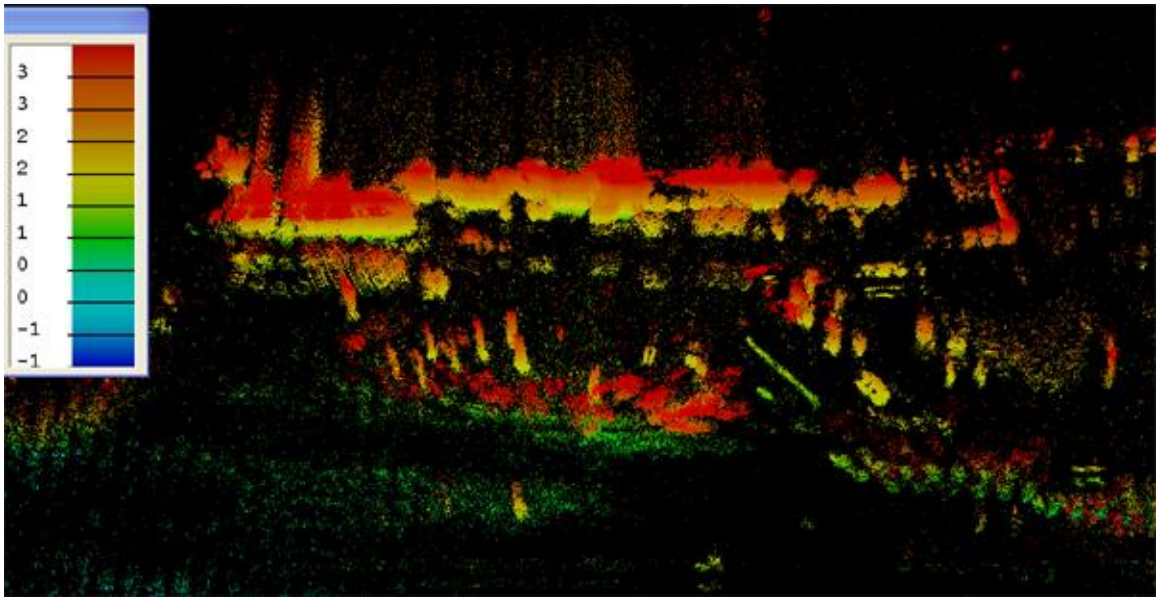

Figure 4-23. Isometric view of 0-3 m data segment to emphasize heights.

A

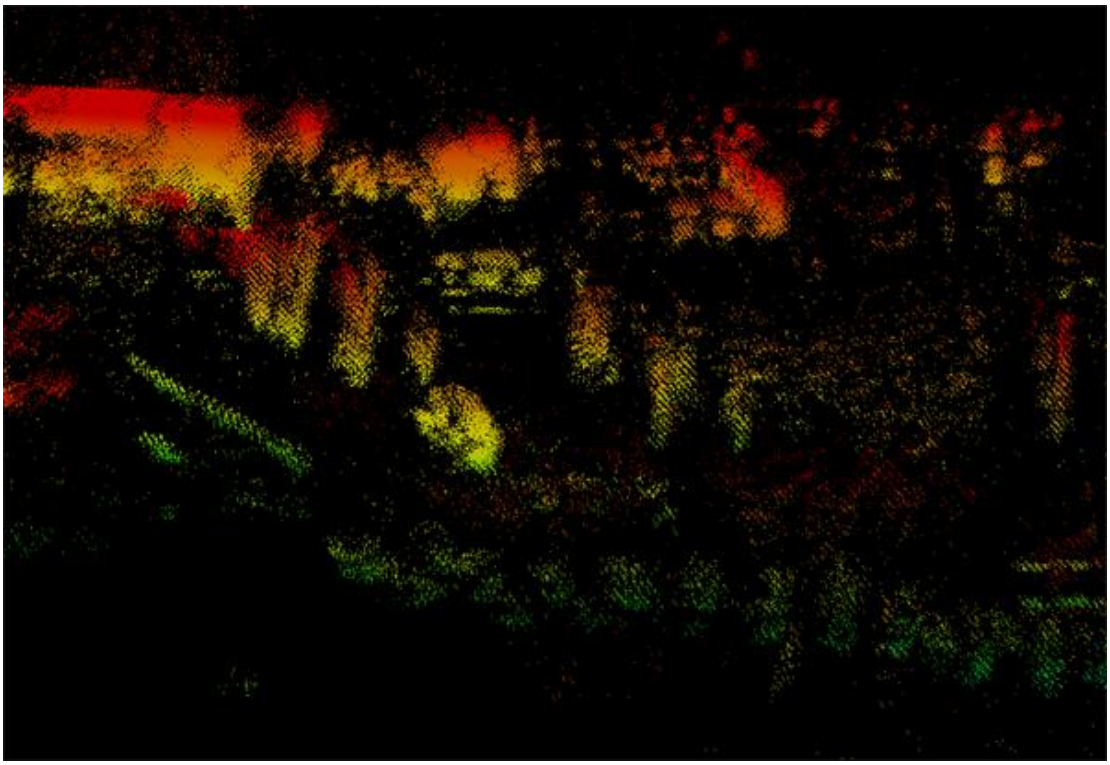

B

Figure 4-24. Zoom-in on isometric view of 0-3 m data segment. A) Photo near building. B) Isometric view with bushes, tree trunks and white bench chair with rounded top in foreground and building walls in background.

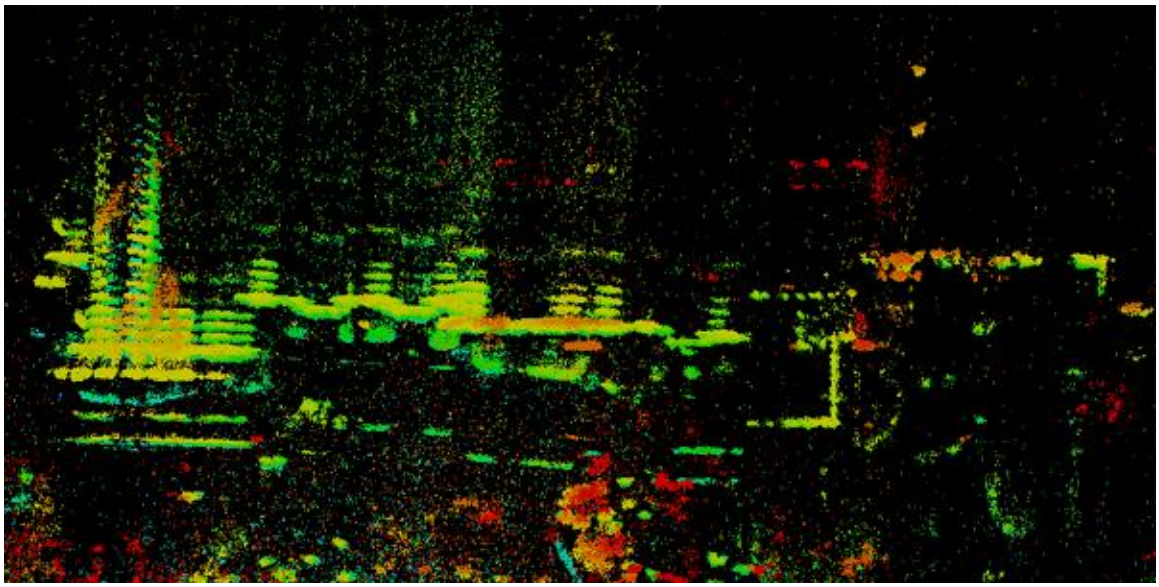

A

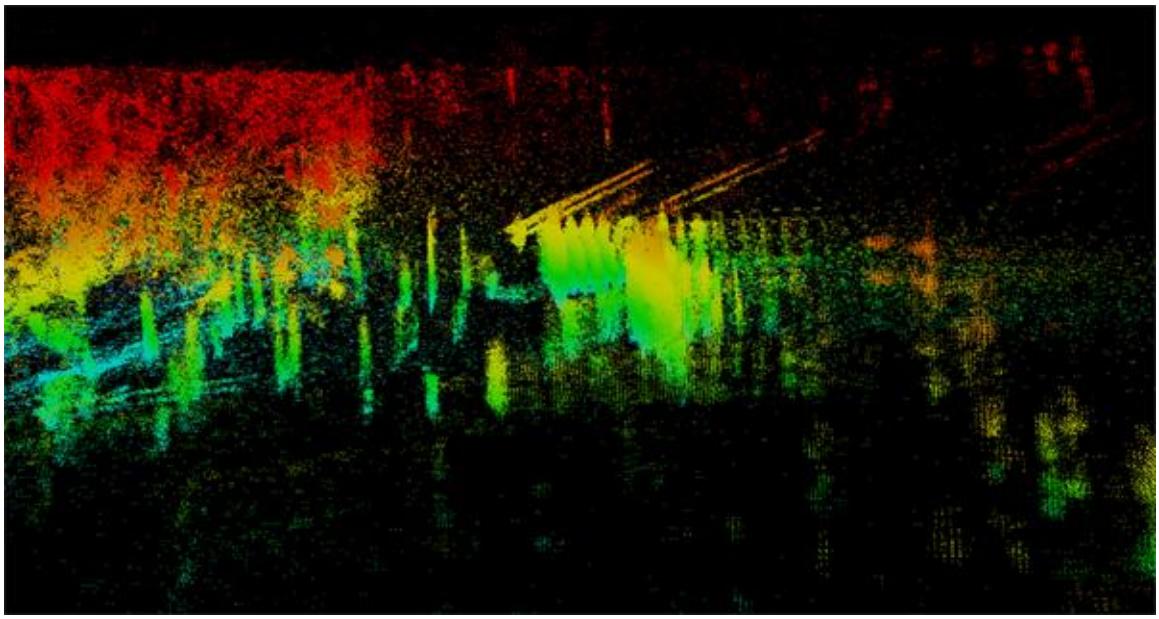

B

Figure 4-25.Top and side view of 0-5 m data segment. A) Top view expanded to 5 m height (red points). B) Side view expanded to 5 m height.

CHAPTER 5
LSNR AIRBORNE LASER BATHYMETRY

ALB Background

The ability of light detection and ranging (LIDAR) hydrography to create detailed maps via flexible data collection methods supports a variety of applications, including nautical charting, hazard identification, erosion modeling, storm damage assessment, and beach nourishment / design [59]. By the late 1980s, the idea of airborne laser bathymetry (ALB) showed promise from systems such as the U. S. Airborne Oceanographic LIDAR, the Canadian Larsen 500, the Australian WRELADS, and the Swedish FLASH [60]. Operational systems matured during the early part of the next decade, with successes by systems such as the Royal Australian Navy's Laser Airborne Depth Sounder (LADS), the U.S. Army Corps of Engineer's Scanning Hydrographic Operational Airborne Laser Survey (SHOALS), and the Swedish Maritime Administration's HawkEye.

As volume of data and rate of acquisition became less restrictive concerns for progressing computer technology, the processing workflow moved from a manually intensive line based approach to an automatic area based methodology [59]. In the early 2000s and through much of this decade, improvements have been made to increase the pulse rate, spot spacing, and portability of ALB systems [61], but the nature of the sensing – representation of the air/water interface, water column, and bottom via green channel waveforms – remains largely the same.

Multiple Information Channels in Laser Ranging

The combination of green channel information with other types of observations has proven useful for feature separation, especially in the bathymetric context. Data from

the SHOALS, for example, have been used to make high-density measurements of the coastal zone for a number of years [62]. Analysis of 1064 nm (infrared) channel data in conjunction with parallel green waveforms is beneficial for distinguishing the specular interface reflection, or water surface, from the diffuse bottom reflection [62], [63], [64], [65]. As a general rule of thumb, the SHOALS is sensitive to bottom returns out to 2-3 times the Secchi depth and out to a maximum of 60 m in the clearest coastal waters.

Shallow water detection (<5 m), however, has been shown to be difficult. Older ALB data sets such as those collected prior to 2004 tend to have gaps in coverage related to complexities in processing very shallow water data [61]. Traditional depth extraction algorithms have problems dealing with merged waveforms even with manual interventions. Recent enhancements to the traditional SHOALS depth extraction algorithms from green APD waveform data have shown interesting developments for dealing with mixed-mode signals in waters less than 1.5 m [61].

Changes in laser-induced water Raman backscatter can be used to detect surface oil slicks [66], [67] and to measure chlorophyll concentrations to estimate phytoplankton dynamics [68]. Research also indicates that novel analysis of red-channel waveform data associated with Raman scattering can provide an approach for measuring very shallow (<2 m) water depths [64].

Additional channels of information are a luxury that modern systems can exploit to produce high-resolution area maps. The work pursued here, however, is aimed at evaluating whether information from only the green channel can be used to provide similar types of feature detection when a different type of detection methodology is utilized.

Challenges Facing Single-Channel Detection

Ideally, a light detection and ranging (LIDAR) system will record a digitization of the return waveform resulting from each laser shot. This allows for a post-processing algorithm to identify time intervals associated with inflection points in the reconstructed signal. Small footprint LIDARs then have the potential to provide detailed characterization of vertical structure at high spatial resolution [14]. The idea of building an "all-green" airborne bathymetry system that meets depth accuracy standards faces several impediments. For full-waveform mapping, the interface component signal amplitudes depend strongly on the beam nadir angle, wind speed, and specific irradiated wave slopes, causing signals to vary with huge standard deviation [47]. Subject to these varying conditions, there may only be a small fraction of the outgoing laser energy that is reflected back into the atmosphere to be collected by the ranging receiver. The resulting surface uncertainty problem is a serious issue for system designers attempting to decide which portions of the return waveform to interpret as sea surface and bottom in a real-time, automatic manner.

At 532 nm in a typical coastal environment, less than 2% [69] of the laser light is reflected back from the air-surface interface. A large portion of the green laser pulse is refracted into the water column. The beam undergoes scattering from entrained microscopic particulates that causes it to spread into a cone of continuously increasing angle. A fraction of the transmitted energy in the water column, which decreases exponentially in magnitude with greater depth, is incident on the bottom with a lateral extent that depends on the scattering properties of the medium and optical depth. A portion of this incident energy, typically 4 to 15% depending on bottom composition [64], is reflected from the sea floor back into the water column. Absorption and scattering

again attenuate and stretch the pulse as it passes back to the surface, where most is refracted back into the atmosphere.

A photodetector such as the avalanche photodiode or photomultiplier tube needs to employ substantial amplification (>10^4) in order to magnify low amounts of this backscattered energy (<1 fJ) into a measurable signal. Detection beyond 10 m depths has typically required significant outgoing pulse energy at 532 nm (>50 µJ). The generation of large amplitude pulses (>2 mJ) can simultaneously increase the outgoing pulse width (>10 ns), which has reduced the capability of typical ALB systems to accurately survey shallow (<5 m) coastal areas [61],[64]. Increasing output energy can also cause safety issues at low altitudes and requires more sophisticated lasers.

Pulse Width and Output Energy Considerations

In past ALB systems, green beams were purposely expanded to a diameter of at least several meters in order to achieve eye-safe operation with sufficient pulse energies to provide reasonable signal-to-noise ratios at greater depths [70]. For example, the Optech SHOALS-3000 system uses a 3 kHz, 6 ns, 3 mJ laser [Tuell, personal communication, 2009] to provide bathymetric measurements up to 60 m depth at 2x2 m spot spacing [62]. The NASA Experimental Advanced Airborne Research LIDAR (EAARL) takes a different approach by using 532 nm, 10 kHz, 1.2 ns, 70 µJ pulses (~1/43 the amount of energy) with a much narrower FOV; ~2 mrad [70]. This is an interesting system because the combination of short pulse and small FOV is expected to overcome the ambiguity traditionally encountered with surface location detection in green-only ALB; an idea that must hold true if the CATS is to achieve any success. Four 1 ns waveform digitizers connected to photodetectors operating at varying sensitivity allow for cross-environment surveys that include abrupt surface

brightness boundaries, typically a cause of saturation in sensors optimized for viewing dark water targets. This system has been shown to be capable of accurately surveying 12 m depths [71]. Optical rugosity analysis by the EAARL in Biscayne National Park showed measurements consistent with field observations of coral features relative to rubble-dominated bank reefs within the study area.

Given recent advances in low-signal level detector technology, a further question is raised: how much can we lower the outgoing pulse energy and still achieve shallow (0-5 m) bathymetric detection when paired with current commercially available photomultiplier tubes? We have previously alluded that LSNR detection methodologies work well for low-noise environments such as satellite laser ranging, but shallow-water bathymetry presents a host of new variables with which to contend. The CATS sensor is uniquely suited to answer this question. In relation to previous successful ALB systems, the EAARL sensor is considered to be a low-power system. In comparison to the EAARL, the CATS sensor outputs 35 nJ per channel; 1/2000 of the energy. This represents quite a drastic shift from traditional ALB design philosophies.

Contrast to Waveform Digitization

In waveform digitization post-processing or embedded filtering (such as constant-fraction discrimination), there is some level of decision making that occurs on an automatic scale. For example, effects such as amplitude dependent range walk, slope dependency of range and signal ringing can have negative effects without proper compensation [72]. For LSNR shallow-water bathymetry, complete waveform digitization may not be mandatory. It may be possible to move to a simple fixed-threshold detection strategy and retain similar feature detection results. In Chapter 4, static experiments showed that the estimated density of data points from the sea bottom

given 20-cm pixel spacing should be sufficient to establish near-shore depths (up to 5 m) at coarse spatial resolution (1 m scale) [56].

Experimental Setup

The CATS sensor was designed to be mounted alongside a commercial ALTM unit such as the Optech Gemini, which is routinely operated by the University of Florida. To minimize costs, it contains no inertial measurement unit (IMU). However, for the tests reported here, the Gemini sensor was not used and the CATS sensor was mounted in a Cessna Skymaster twin-engine aircraft, shown in Fig. 5-1. A special mount was constructed out of aluminum plates and bolted directly to the rails that normally support the co-pilot's seat. The system was therefore rigidly attached to the aircraft frame, but no IMU data were collected with which to correct the observations for changes in the orientation of the aircraft. Artifacts resulting from changes in the orientation of the aircraft (roll, pitch, and yaw) include undulations of flat water surfaces and lateral wandering of the surface profiles.

The mounted CATS sensor head fits down into an opening in the floor of the aircraft with approximately 5 cm free space surrounding the main cylinder containing the Risley prisms. A DC power supply provided 24 V at approximately 3 A. The DC supply received 120 VAC from an inverter, connected to the aircraft's main power system. A laptop PC was also connected to this inverter. The scanner control box and timetag module were secured behind the pilot and at the feet of the operator.

Experiments were conducted to test the system's airborne profiling capability. The two prisms were set 180º out of phase so that the laser would be pointed straight along the optical axis of the transmit / receive path, or at nadir. The aircraft was flown at approximately 60 m/s and 500-600 m height above ground level for a series of ranging

trials. Because a large number of returns per channel were expected, only channels on the second ranging board (17-32 or the central 4x4 square) were enabled for a majority of the experiments. Initial collections with all 96 elements enabled in profiling mode at the highest gain produced such a wealth of returns that the data throughput exceeded system capacity.

Small Structure Identification

Several different types of buildings and other manmade objects were profiled at nadir in a flight over the University of Florida campus in Gainesville, FL. Fig. 5-2(A) shows an aerial photo of a region at the south end of campus and flight line. Fig. 5-2(B) is the raw point data from channels 20 and 23. The image allows us to identify a small outcropping in a building roof, a roof from a nearby parked car, angled roof geometry from small office buildings, the outline of a stone bench, and a low-hanging awning between two buildings.

Vertical Canopy Structure Identification

Fig. 5-3 shows an unfiltered point cloud generated from data over a forested region in Mine Run, VA. Small leaf structure elements are definable here based on a large number of multiple scattering events. The flight was conducted in autumn as the deciduous forest was in the process of shedding leaves; this left small pockets of space in the overhead canopy through which individual beamlets could propagate. Even partial transmission of beam elements as a result of semi-occlusion by leaf surfaces was enough to reconstruct intra-canopy elements and the ground surface below the tree line. A zoom-in depicting a narrow tree trunk is pictured.

Optimizing System Performance

Analysis of data from test flights showed that overall signal strength at maximum PMT gain (2500 V or $8 \cdot 10^5$) was high enough to warrant changing data collection parameters. Responses from strongly reflective surfaces at this gain level produced a stacking effect (hits in many consecutive range bins) near roof surfaces in the resulting image. Since the microlaser output energy and detector type were selected to maximize LSNR performance in turbid waters, this was an expected outcome. The dynamic range between different types of features (especially when contrasting topographic and bathymetric returns) may be very large. Responses from artificial surfaces for on-nadir beam propagation at 2500 V were tens of range bins deep in some cases.

Data collections at multi-photon sensitivity (2300 V or $2 \cdot 10^5$ gain) are capable of producing responses 3 to 4 bins deep from surfaces such as building roofs, bare earth, and tops of tree canopies. We could thus reduce the tube voltage for future surveys and expect the top end of our dynamic range to be reduced. Generally speaking, if interrogated far-field surfaces were of uniform reflectance and the gain of the tube is matched to provide exactly enough amplification to barely produce a threshold crossing, this might be an acceptable technique. Of course in practice, target reflectance properties are not precisely known, and tailoring a detection strategy to one type of feature negates the real benefit of this type of sensor—mixed mapping. As shown in Chapter 4, shallow-water bathymetry is difficult at less than full amplification (2500 V). For the LSNR detection paradigm to be worthwhile related to submerged surface mapping, an amplification level should be maintained that produces returns from even very weak scatterers.

Another solution may be viable: changing the type of airborne profiling from on-nadir to off-nadir. By imposing a fixed incidence angle relative to ground for outgoing laser light, the magnitude of the backscattered radiation is decreased due to less significant contributions from specular reflections and increased slant range. This has special relevance in the case of mirror-like water surfaces as large specular components cause problems for shallow bathymetry on-nadir operation. A circular pattern is one way to propagate this effect throughout a scan and retain contiguous terrain coverage; in fact along-track resolution is effectively doubled.

Even with off-nadir operation, and the potential advantages of circular versus raster scanning, CATS data shows that there is still a dynamic range issue because of the large difference in signal strength between topography / sea surface elements and distributed targets such as partially occluded forest canopies and submerged surfaces. For large-scale uniform surfaces such as building roofs, it may be possible to automatically collapse range tails into first returns and simultaneously provide some measure of intensity about the response, dependant on the number of range bins that the signal stretches over and the expected cross-section geometry [24]. Dynamic range is one of the major challenges for adaptive algorithm development [73]; automatic procedures are usually dependent on the local coherence of return information.

Data Artifacts

Accurate characterization of data artifacts can be one of the most challenging obstacles for a developmental LIDAR system. This is especially relevant for LSNR mapping as in some cases the noise floor can eclipse the true signal level. We expect, however, that true signals will exhibit some form of spatial coherence even in lowly populated areas due to the random nature of noise formation, allowing us to use

techniques such as Post-Detection Poisson Filtering (PDPF) and a Correlation Range Receiver (CRR) [15] to beneficially exploit data trends. We will consider in detail artifacts specific to the CATS to evaluate the applicability of this claim for mixed topographic and bathymetric data processing.

A closer inspection of detected surfaces in Fig. 5-2 shows a potential problem; a "ghost image" of roof surfaces appears at a constant offset beyond the first return. Though we may be able to easily remove these types of artifacts for bare-earth and building measurements via an automatic first-surface algorithm, we risk losing important multiple-return information from other types of features. On the other hand, if no algorithm is applied, we risk lumping the ghost returns in with partial reflections in close proximity (<10 m) to the first. Our data sets may then also require significant manual processing. In the worst-case scenario an automatic data classifier may erroneously identify a ghost image from the water surface as a submerged element, yielding an inaccurate depth estimation. Analyzing the scope of such artifacts is thus of prime concern for shallow water bathymetry.

The influence of this type of noise is not always obvious because the magnitude of the responses is suspected to be fairly low, meaning that certain types of data visualizations can cause the effects to be classified as random thermal events or volumetric scattering residuals rather than deterministic occurrences. It is important to develop an automatic data processing technique that compensates for the noise effects so that their influence does not lead to false feature characterizations. For example, when first returns are plotted from channel 23 in Fig. 5-4(A), ghost surfaces are difficult to identify. The image seems close to what we would expect; canopy returns are well-

distributed for partial leaf-on conditions, bare-earth surfaces (x<150 m) are singular, and water returns (x>150 m) are generally bi-modal. The distribution of noise returns relative to these features, however, should be analyzed in further detail.

Above the ground / water surface, we expect random contributions from dark / solar events as well as atmospheric laser backscatter. Below ground and past ~5 m water depth, we expect only contributions from dark / solar noise. Fig. 5-4(A) thus gives us some indication that an aberrant effect may be in play; below ground noise events are more numerous. The opposite should be true if our noise assumptions are valid. When all returns from 16 channels of data are plotted in Fig. 5-4(B), artifacts become much more evident; atmospheric noise increases slightly as expected, but the large number of below-ground returns is now a stark contrast. This effect persists even through overlapping first-return data; the theorized cause is a combination of noise and crosstalk between PMT grid elements.

Though it is clear from Fig. 5-4(B) that artifacts below strongly reflective surfaces are significant, further quantification may aid in noise identification and processing efforts. For example, MATLAB can be used to compute estimates for local density in selected regions within the cloud. A segment of flat ground data was manually windowed to encompass expected signal returns. Ghost responses should exhibit well-defined correlation to this window; the temporal offsets of expected highest correlation are shown in Fig. 5-5 as "afterpulse 1/2." By then sliding the true signal window vertically as in Fig. 5-6 and expressing the correlation coefficient as a ratio of true signal density to the measured effect, the plot in Fig. 5-7(A) was generated. The plot decreases exponentially starting at zero distance (correlation % of 1.0) down to the

noise floor, which is below a correlation % of 0.1. Here the correlation of ghost images is not distinguishable. We then conclude that the spatial distributions of artifacts are significantly less dense than the true signal. In order to analyze information near the noise floor, the y-scale needs to be expressed logarithmically, as in Fig. 5-7(B). If we fit Gaussian profiles to the output and measure the peaks, the largest correlations occur at 12.67 and 24.00 ns, with respective peaks of 0.0085 and 0.0053 (Fig. 5-7(C)).

We can posit several possible explanations for the noise. First, gas impurities in the tube envelope can generate additional responses beyond the initial high-intensity return; this is commonly referred to as "afterpulsing" in nuclear particle physics experiments. Second, the cable connecting the PMT output to the high-speed data interface could have an impedance mismatch. A mismatch could cause undesirable reflections from the interface junctions to become significant at very high signal levels. Third, the silicon germanium high speed gain block could be being overdriven in cases of large signal output. This would cause the amplifier to operate beyond maximum recommended ratings, thereby inducing anomalous effects.

PMT Afterpulsing

Exploration into the chemical and physical nature of PMT afterpulsing effects [74], [75], [76] showed that diffusion of trace gases through the tube envelope contribute to an increase in the probability of pulse formation. In particular, diffused helium was found to be the main source of afterpulses in tubes more than two years old. In contrast, the contribution from this impurity in new tubes was often small [76]. An exponentially decaying low-level background signal has been shown to occur after the abrupt termination of a sub microsecond light pulse [77]. Positive ions produced during the ionization of residual gas in the PMT by photoelectrons produce secondary

electrons during their drift back onto the photocathode, which are then amplified [78], [79]. Other possible explanations for both short (sub-microsecond) and long-term (microsecond to millisecond) responses are electron-induced luminescence of the dynodes or their support structures and microdischarges produced during high-gain operation [77].

Because the CATS uses an MCP-PMT manufactured in 2004 that has undergone significant use, it is possible that trace amounts of atmospheric gas diffused into the envelope over time may have risen to significant levels. Quantifying the amounts of impurities is beyond the scope of this work, but potential contributions from afterpulsing should be mentioned due to the age of the tube.

Impedance Matching

For radio frequency (30 kHz to 300 GHz) circuitry, the impedance of the transmission line itself becomes significant. In order to maintain maximum power transfer, the characteristic impedance of the cable (Z_O) should be closely matched to the source (Z_S) and load (Z_L). If the total path length is greater than 10% of the signal wavelength, mismatch effects can have greater impact. In the CATS system, 2-GHz level signals mean that transmission lines longer than 4 cm must be well matched (assuming velocity factor of 0.8). We should then consider the layout of associated PCBs in the receiver design and estimate the total length between the PMT and data capture elements. The minimum trace length is the sum of the following lengths:

- MCP-PMT pin to PMT adaptor board connector: 12.95 cm
- Samtec HFHM2 cable (1): 25.40 cm
- Samtec HFHM2 cable (2): 25.40 cm
- Frontplane board trace: 8.13 cm
- Connectors: 12.70 cm

The total trace is then 84.58 cm. Assuming an average propagation delay of 70.98 ps / cm, the total delay is 6 ns. The layout of potential cable reflections in relation to a transmitted signal is shown in Fig. 5-8. In this model a signal pulse is initiated at T=0, at the near end of the trace. The pulse reaches the far end of the trace at T=6 ns. Here a portion of the signal is reflected back dependant on the match between R_o and R_L, which causes another reflection at T=12 ns based on the match between R_s and R_o. This reflection reaches the far end of the trace at T=18 ns. This process continues infinitely, and output pulses of diminishing magnitude will be received at T=6, 18, 30, etc. intervals. The estimated spacings of the first two reflections are close to the temporal spacings calculated from local density correlations (12.67 and 24 ns). The next step is to calculate the expected magnitude of reflections based on manufacturer specifications for impedances.

The line lengths of the Frontplane board are matched for a maximum channel-to-channel delay difference of 18 ps. Signal routes are 50 Ω single ended lines. Test data using Time Domain Reflectometry (TDR) are given in Table 5-1. The measurements show the average impedance for each layer; deviations are expected due to variations in PCB manufacturing tolerances of the layer thickness and line width. If we let Z_L = 49.9 Ω and consider Layer 3 (L5), Board 2 as a worst-case scenario, we can use the following analysis to calculate the magnitude of the first two reflections. When a signal is impressed on the end of a transmission line, a fraction of the full source voltage propagates down the line. This is referred to as the input acceptance function A, and is expressed in terms of Z_S and Z_O [80],

$$A = \frac{Z_O}{Z_S + Z_O}. \tag{5-1}$$

Next, the signal is attenuated by the propagation function H. For this analysis we will assume an average value of 0.94. At the far end of the cable a fraction of the attenuated signal amplitude emerges, which is determined by the output transmission function,

$$T = \frac{2 \cdot Z_L}{Z_L + Z_O}. \tag{5-2}$$

When a fraction of the propagating signal emerges from the far end (T=6 ns in our model), a reflected signal also travels back along the cable towards the source. The magnitude of this reflection is determined by the far-end reflectance function,

$$R_2 = \frac{Z_L - Z_O}{Z_L + Z_O}. \tag{5-3}$$

The reflected signal is again attenuated again by H as it travels towards the source where it reflects a second time off the source impedance. The source end reflection function is given by,

$$R_1 = \frac{Z_S - Z_O}{Z_S + Z_O}. \tag{5-4}$$

After the second reflection, the signal is attenuated by H as it travels back to the load as it again emerges via the transmission function T. This process continues on indefinitely. We can use these functions as coefficients to calculate the magnitude of the first three signals:

$$Signal_1 = A \cdot H \cdot T, \tag{5-5}$$

$$Signal_2 = A \cdot H \cdot R_2 \cdot H \cdot R_1 \cdot H \cdot T$$

$$Signal_3 = A \cdot H \cdot R_2 \cdot H \cdot R_1 \cdot H \cdot R_2 \cdot H \cdot R_1 \cdot H \cdot T$$

For $Z_S = Z_L$ = 49.9 Ω and Z_O = 52.84 Ω (upper worst case), we find $Signal_1$ = 0.47, $Signal_2$ = 0.0004, and $Signal_3$ = $2.46 \cdot 10^{-7}$. For $Z_S = Z_L$ = 49.9 Ω and Z_O = 47.52 Ω (lower worst case), we find $Signal_1$ = 0.47, $Signal_2$ = 0.0002, and $Signal_3$ = $1.31 \cdot 10^{-7}$. The first reflection in both worst-case scenarios is then expected to be three orders of magnitude smaller than the true signal, and the second reflection six orders or magnitude smaller. Though potential reflections resulting from worst-case impedance mismatch may occur at the same temporal spacing as the ghost images, the magnitudes appear to not be significant.

Gain Block Overdrive

Output signals are amplified by a 4000 MHz 2.8V SiGe gain block manufactured by Sirenza Microdevices (part number SGA-1263). The output of this device is fed directly into the threshold comparator for each channel. Because the system needs to operate on a single-photon sensitivity level, channel thresholds are set to a 4 mV trigger. According to the manufacturer's data sheet, the gain block has a maximum RF input power of -12 dBm, or 63 µW, which equates to 56 mV into a 50 Ω load. An output current over 1.1 mA will therefore begin to overdrive the gain block.

In Fig. 5-9, a large signal (110 mV) is injected into the gain block. This is approximately 25 times larger than a signal expected to barely produce a threshold crossing (4 mV). The resulting output is shown in Fig. 5-10. The desired response is the first large negative pulse. Deviations from zero-level in the waveform after the first negative pulse are anomalous effects resulting from the large signal input. Here we see small negative deformations before and after a positive peak. If we inject a larger signal

(200 mV) (Fig. 5-11), the output shown in Fig. 5-12 is produced. A line is drawn here to approximate the threshold crossing. The second crossing occurs at approximately 13 ns. If a still larger signal (300 mV), shown in Fig. 5-13, is injected into the block, we can identify threshold crossings in Fig. 5-14 at approximately 13 and 20 ns.

The temporal spacings of these outputs are similar to that estimated from local density correlation within the point cloud. Because the dynamic range between submerged surfaces and highly reflective topography is so large, it is likely that the overdrive of the gain block is the main cause of ghost images.

Point Cloud Filtering Based on Density Estimates

A data processing method should be developed to eliminate the noise artifacts while preserving feature structure within the point cloud. Because the spatial densities of data artifacts are fairly low (peaks less than 1% of true signal), we can perform point cloud filtering based on local point information and expect not to lose a significant amount of signal information about strongly reflective surfaces. To validate the potential of the LSNR data, generated algorithms should be near-automatic; i.e. with the least amount of manual input as possible.

First, a decision boundary between land and water surfaces was estimated using a sliding horizontal window similar to Fig. 5-6. For each point in the data set used to create Fig. 5-4(B), a 0.6 x 1.0 x 1.0 m box was fitted to produce density estimates in the topographic data defined by the decision boundary. All other points were then classified as potential bathymetric responses and a 0.3 x 1.5 x 1.0 m box was fitted to produce density estimates. The results of this operation on data gathered from a single channel of information are shown in Fig. 5-15. Next, the scene is split into coarse grid cells and data within cells below the noise threshold are eliminated (Fig. 5-16(A)). The secondary

step helps to eliminate the few remaining artifacts, and the final processed image is shown in Fig. 5-16(B). A dense clump of points 5 m above the water surface is visible at x=180 in Fig. 5-16(B); this is the result of returns from an overhanging island tree near the flight line. Because the density of returns suggests that this is not atmospheric noise, the filter retains the associated points.

Fresh Water Bottom Mapping

The major goal of flight testing for the CATS instrument was to evaluate LSNR water penetration capabilities. Application of the expectation maximization (EM) Gaussian-mixture (GM) algorithm shows that surface and bottom can be reliably separated in sea (total attenuation coefficient of 0.05 / m) and coastal (total attenuation coefficient of 0.5 / m) water to a depth of 2 m [21]. At larger depths, simulation also shows that horizontal resolution of the reconstructed sea bottom is greatly limited by water clarity; meter-scale bathymetric mapping should only be possible at sea depths less than three times the Secchi depth.

A zoom-in view of processed data from the shallow fresh water area (the Lake of the Woods) in Mine Run, Virginia is shown in Fig. 5-17(B). The path of the aircraft near the shoreline is indicated in an aerial photo (Fig. 5-17(A)). The water in this area contained low amounts of colored dissolved organic material (CDOM); at the time of the data collection the Secchi depth was measured out to 2 m. The lake bottom was a mixture of dark sand and decaying organic material; bottom reflectivity was expected to be very low. 16 channels of data were collected at 2500 V, or maximum PMT amplification. Manual measurements of water depths in this area at 10 m intervals were also performed using a measuring tape with an attached weight.

Point cloud values were interpolated to estimate the lake bottom surface, shown as a dashed line in Fig. 5-17(B). The bottom was then corrected for the index of refraction of water (1.33), shown as a solid line. Here we see a consistent response from the water surface, shown as a flat line, and an exponential decay of water column returns progressing to further depth. The lake bottom produces a strong signal at ~1.5 m depth near the shoreline at x=140 m. Water depths at 10 m intervals were extracted from the LIDAR data in this region by differencing the interpolated water surface and corrected lake bottom function. Lake bottom returns become negligible at approximately 2 m water depth. There was a large amount of sediment buildup from organic / inorganic particulate near a small island located at x=180 m. This could lead to shortening of the estimated depth near the island. Table 5-2 compares LIDAR depth estimates to measured values. The average difference between estimates and measurements is 21 cm.

The lake bottom was slightly more reflective in other parts of the lake. Fig. 5-18(A) shows a location to the northeast at the same lake where the bottom was composed of a mix of lighter sand and organic material. The increase in reflectivity produced returns from the lake bottom at greater depth. Fig. 5-18(B) shows an off-nadir profile for 16 channels at 2500 V depicting recovery of the lake bottom out to 2 m depth.

Salt Water Bottom Mapping

Further flight testing was conducted over the intracoastal waterway in St. Augustine, Florida. Fig. 5-19(B) shows point cloud data starting from the shoreline (aerial photo in Fig. 5-19(A)) and out to a boat dock 60 m away. In Fig. 5-19(B), the water surface and bottom profile between boat docks and a shallow boat launch region are depicted. Dense clusters of points 1 to 2 m above the water surface are a result of

narrow wooden walkways (x=175, 189, 203 m) leading out to the boathouses. The sand bottom was reflective enough in this case for a single channel to provide bottom reconstruction out to a depth of 2.5 m. Hand measurements of wood platform heights above the water surface were performed at five locations, shown in the third row of Table 5-3. LIDAR estimates of platform heights were calculated by differencing the first above-water return associated with the wood surface and the interpolated bottom at the five indicated locations. These estimates showed an average error of 17 cm.

Fig. 5-20(B) shows information from 3 channels over a sand bar. Bottom features out to a depth of 1.5 m are recovered here in high detail; submerged pockets and dunes are identifiable as currents have affected the sand geometry. An aerial photo of the east coast of Florida near St. Augustine with the aircraft path is shown in Fig. 5-21(A). Fig. 5-21(B) shows the associated point data from 3 channels. Of particular interest in this image are the gradually increasing sea floor slope in the surf zone near the beach / water interface (indicated in dark blue), and the sand bar located 40 m from shore.

Mapping Statistics and Discussion

Simulation [21] predicts that CATS bathymetric performance will largely be dependent on water conditions; in turbid waters, the operational depth for mapping should be limited to a few meters. Analysis of airborne profile data from the CATS over a fresh water lake in Mine Run, Virginia and salt water areas near the eastern coast in St. Augustine, Florida have largely confirmed these predictions for practical turbidities at 0 to 3 m depths. The central 16 channels – 17% of the total footprint area – were sufficient in profile mode to reconstruct a fresh water lake bottom composed of dark decaying organic / inorganic material (estimated to be highly non-reflective) out to 1.65 m. The Secchi depth in this area was measured to be 2 m. At a depth of 0.5 to 1.5 m,

on average 38 returns per meter were registered from the lake bottom. For 8 kHz laser pulse rate and 60 m/s flight speed, this corresponds to an average of 1.77% of the outgoing shots registering returns from the lake bottom. The central 16 channels were also used to reconstruct a fresh water lake bottom composed of light sand and dark decaying organic material (estimated to be slightly more reflective) out to 2 m. In Fig. 5-18(B), less bottom returns near the shoreline were received as a result of overhanging tree branches, but multiple returns still provided information about submerged surfaces. At a depth of 1 to 2 m, on average 74 returns per meter were registered from the lake bottom. This corresponds to an average of 3.49% of the outgoing shots registering returns from the lake bottom.

A single channel of information – 1% of the total footprint area – was used in profile mode to reconstruct a salt water intracoastal floor (estimated to be highly reflective) in water of high clarity out to 2.5 m. At a depth of 1 to 2 m, on average 45 returns per meter were registered from the submerged floor. This corresponds to an average of 33.98% of the outgoing shots registering returns from the floor; these are assumed to be near-ideal conditions. Three channels of information – 3% of the total footprint area – were used in profile mode to reconstruct the sea floor (estimated to be highly reflective) in the surf zone near a beach in water of optimum clarity out to 2 m. At a depth of 1 to 2 m, on average 56 returns per meter were registered from the sea floor. This corresponds to an average of 13.98% of the outgoing shots registering returns from the floor.

A

B

Figure 5-1. Photos of the CATS mounted in aircraft. A) Cessna Skymaster aircraft. B) Mounted CATS sensor head.

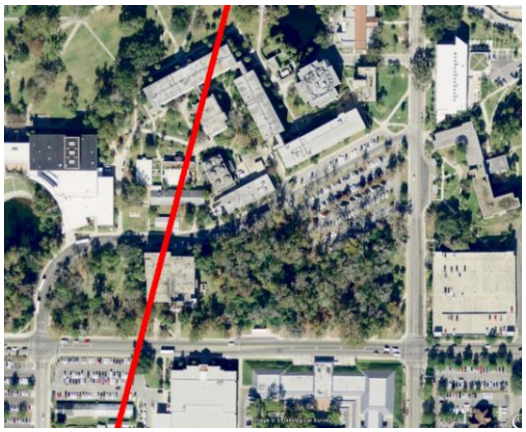

A

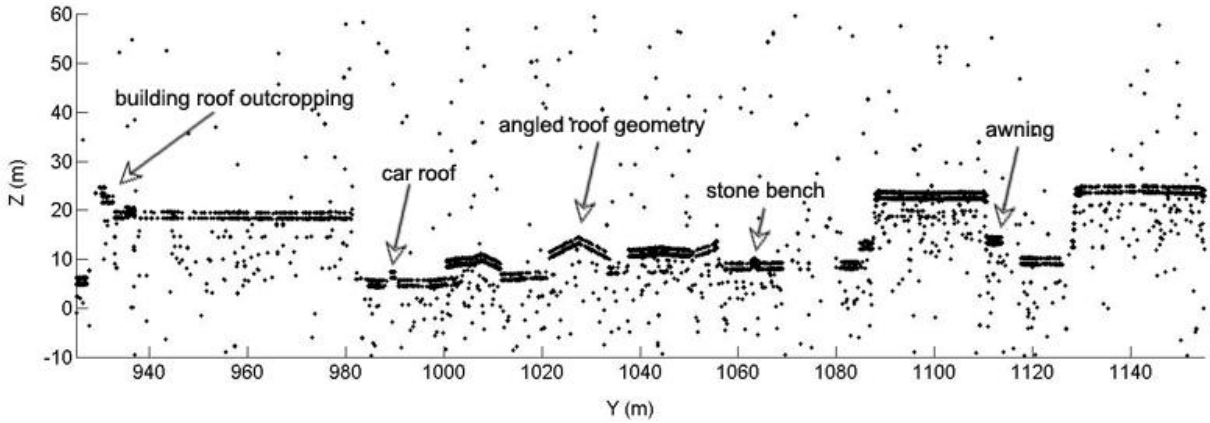

B

Figure 5-2. Flight testing in Gainesville, FL over University of Florida campus. A) Aerial photo with flight line. B) Channels 20 and 23, 2300 V, all returns, unfiltered data showing vertical resolution capability in structure identification.

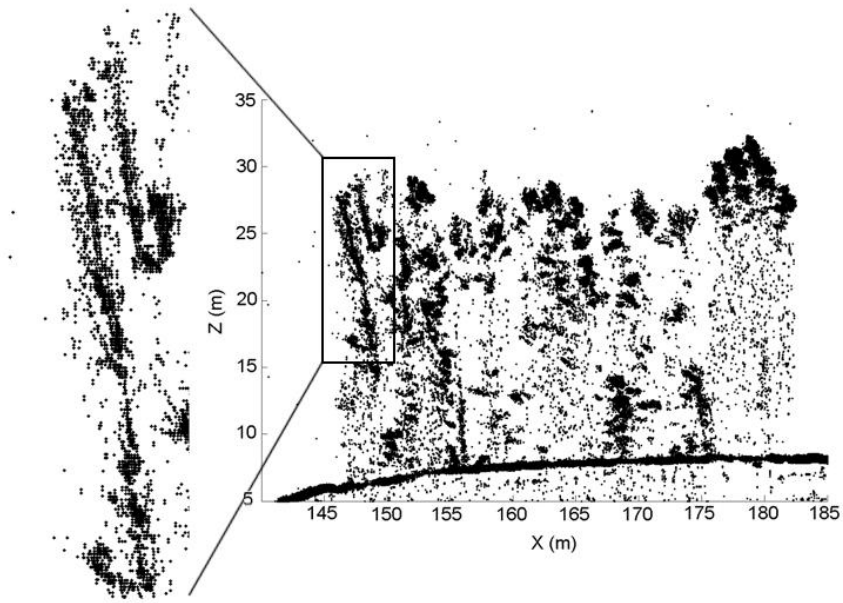

Figure 5-3. Small point cloud from forested region in Mine Run, VA. Small leaf structure elements are definable along with trunk and ground information.

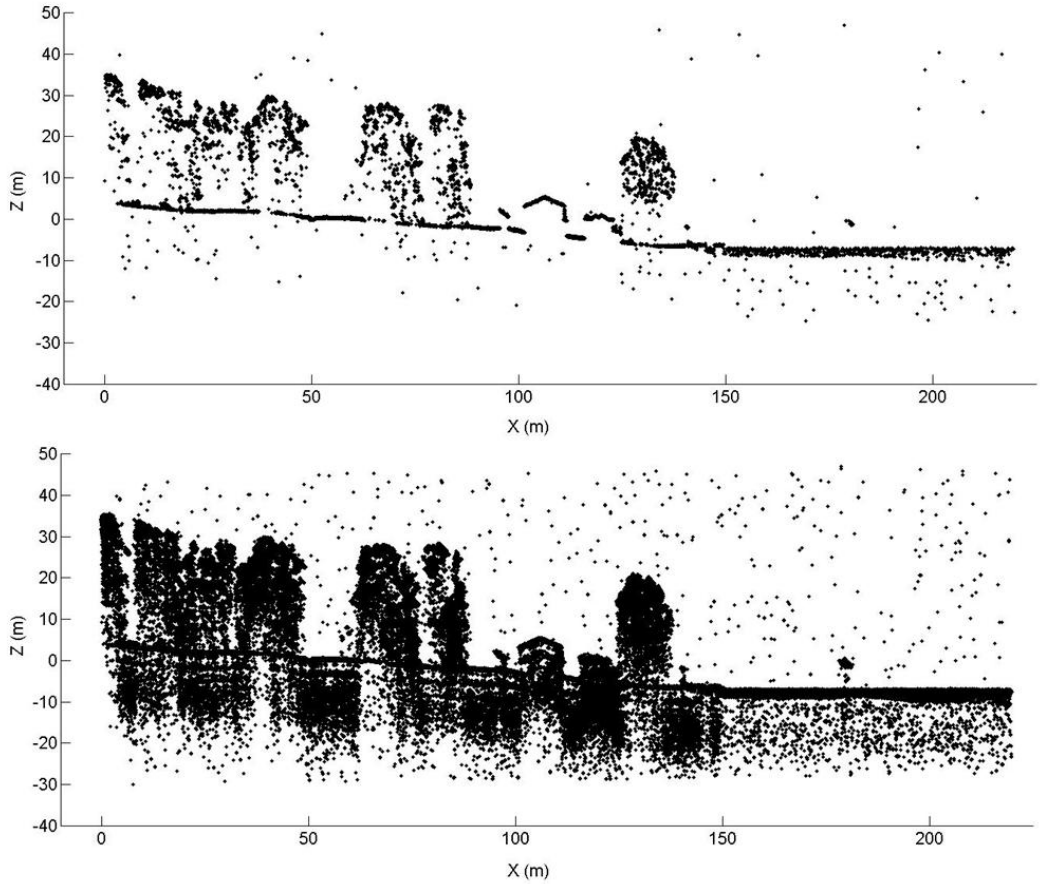

Figure 5-4. Large point cloud from forested region in Mine Run, VA. A) Channel 23, 1st returns plotted. B) Channels 17-32, all returns plotted.

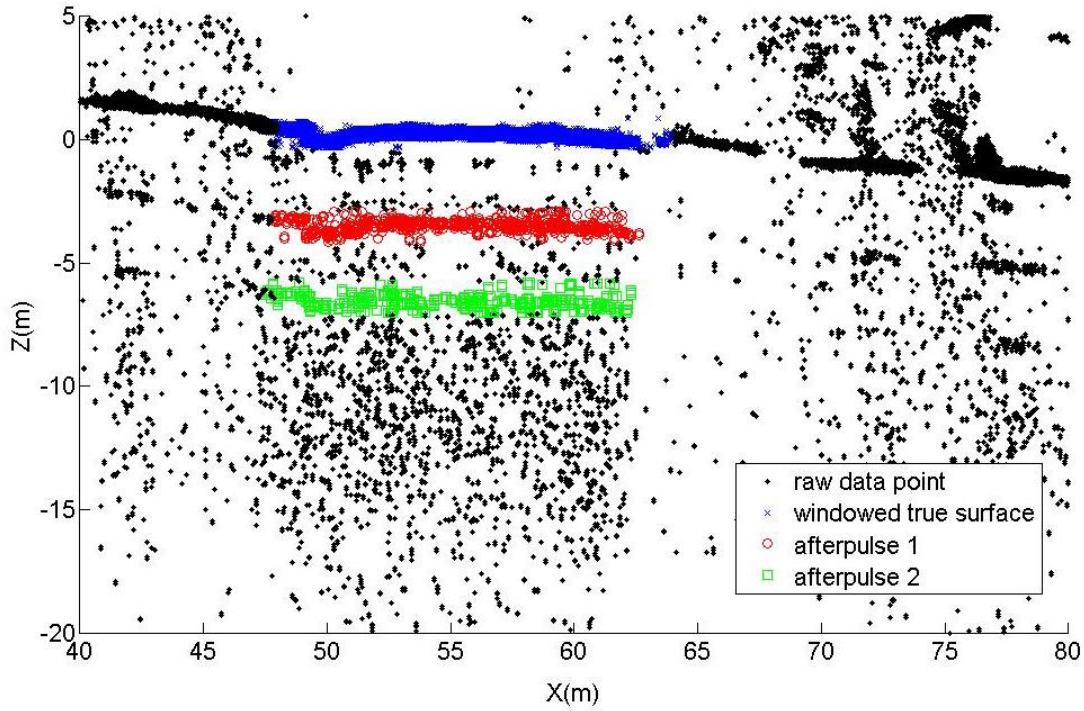

Figure 5-5. Ghost images in raw data.

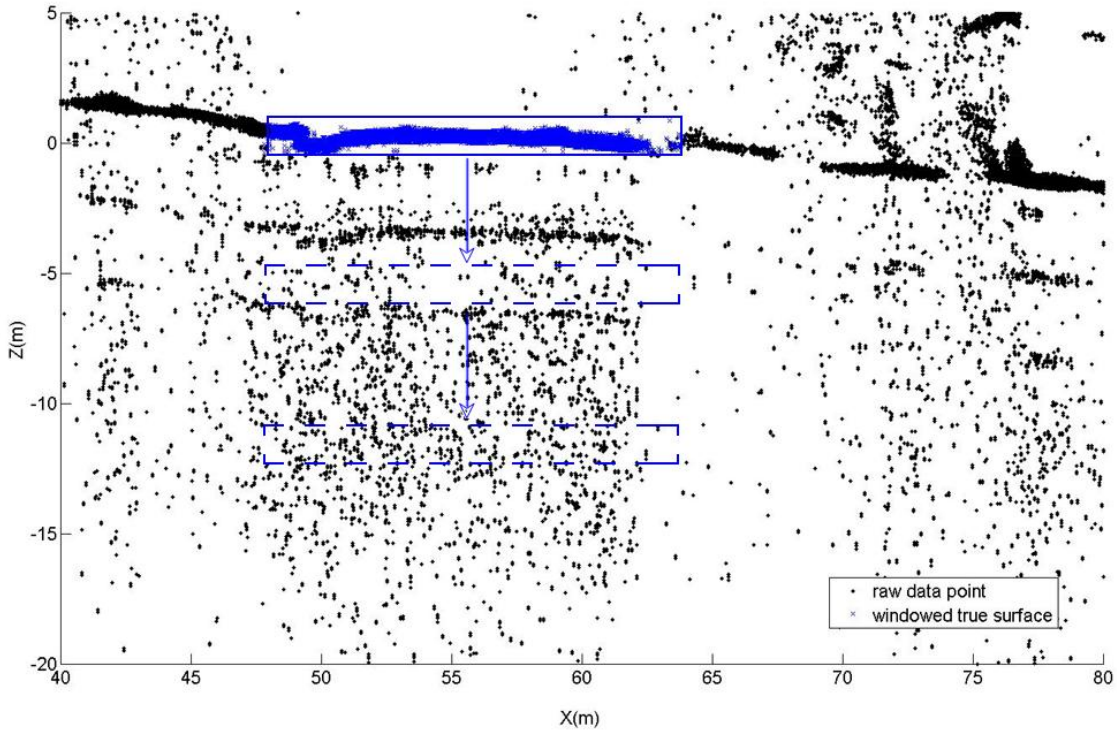

Figure 5-6. Vertical sliding window to evaluate magnitude of ghost responses.

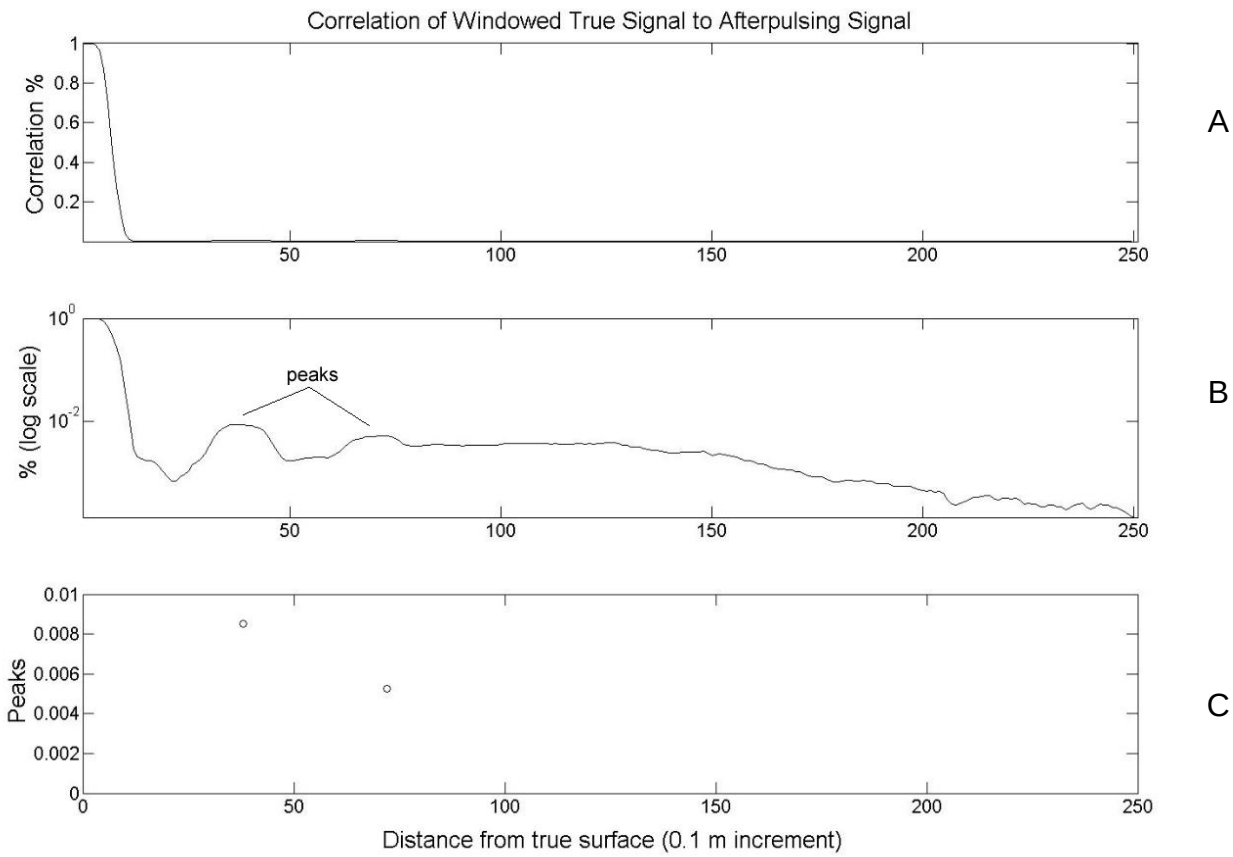

Figure 5-7. Results from sliding window. Correlation between responses in 0.1 m increments, starting from true surface (correlation coefficient of 1.0). A) Normal scale y-axis, peaks are indistinguishable. B) Log scale y-axis, ghost peaks are visible. C) Magnitude of peaks are both less than 1%.

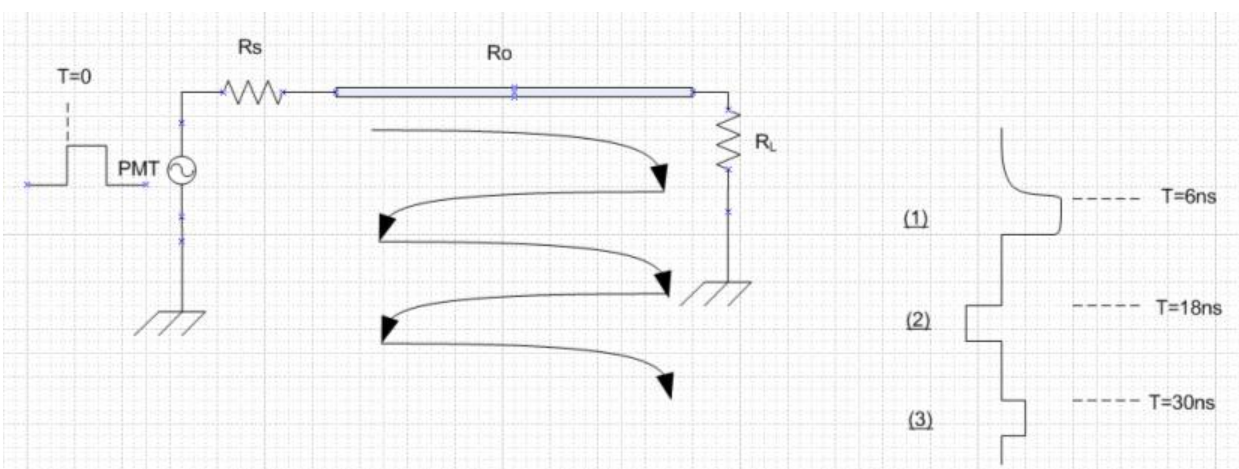

Figure 5-8. Graphical model depicting reflections from detector cable interfaces.

Table 5-1. Time Delay Reflectometry test data (courtesy of Fibertek Inc.)

Board #	L1 (Ω)	L3 (Ω)	L5 (Ω)	L7 (Ω)	L9 (Ω)	L11 (Ω)
1	51.28	52.00	51.17	51.43	51.91	51.72
2	49.27	52.84	52.82	51.63	51.29	51.88
3	47.52	52.00	50.80	51.82	52.47	51.76

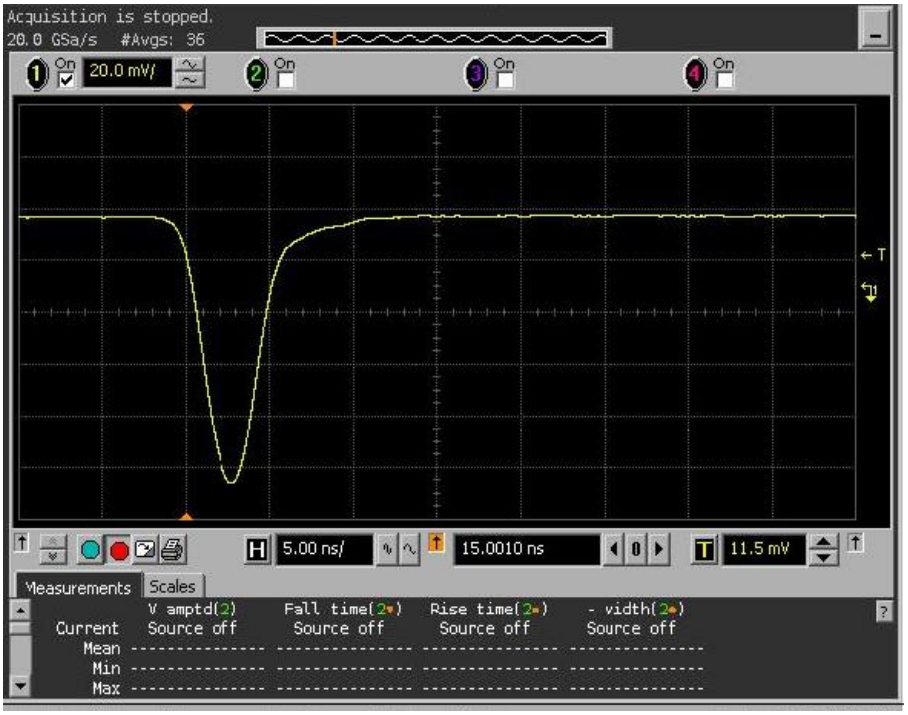

Figure 5-9. Large signal (110 mV) injected into gain block (courtesy of Fibertek Inc.).

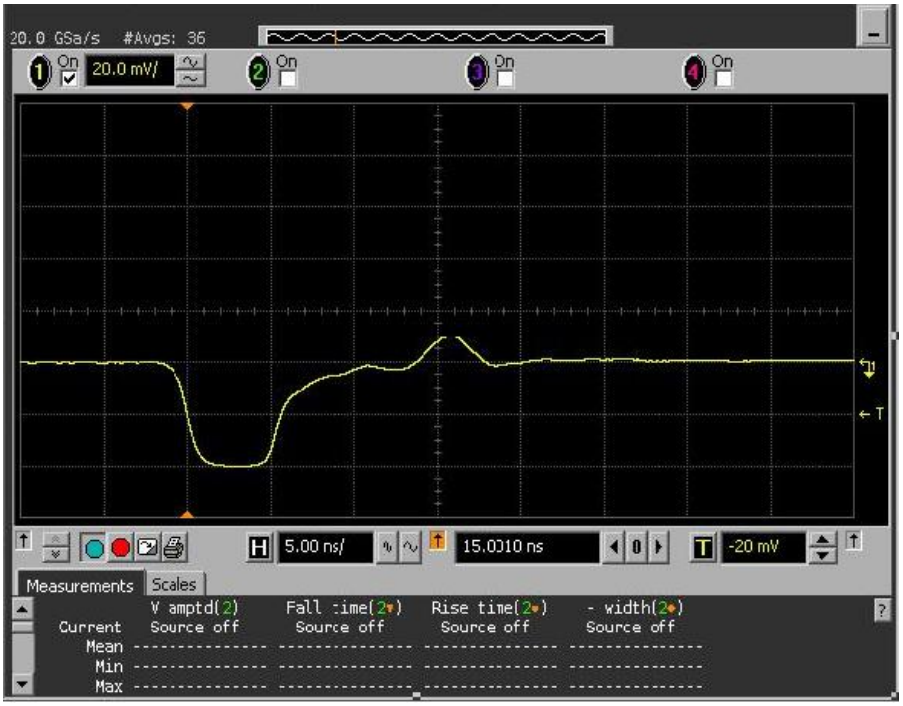

Figure 5-10. Output of gain block from 110 mV signal (courtesy of Fibertek Inc.).

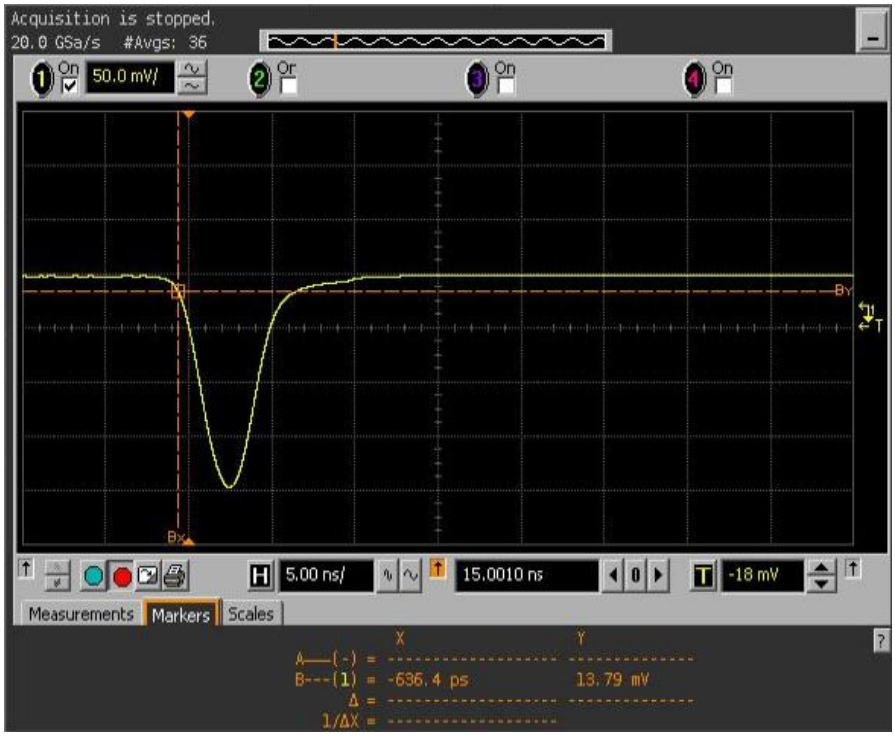

Figure 5-11. Large signal (200 mV) injected into gain block (courtesy of Fibertek Inc.).

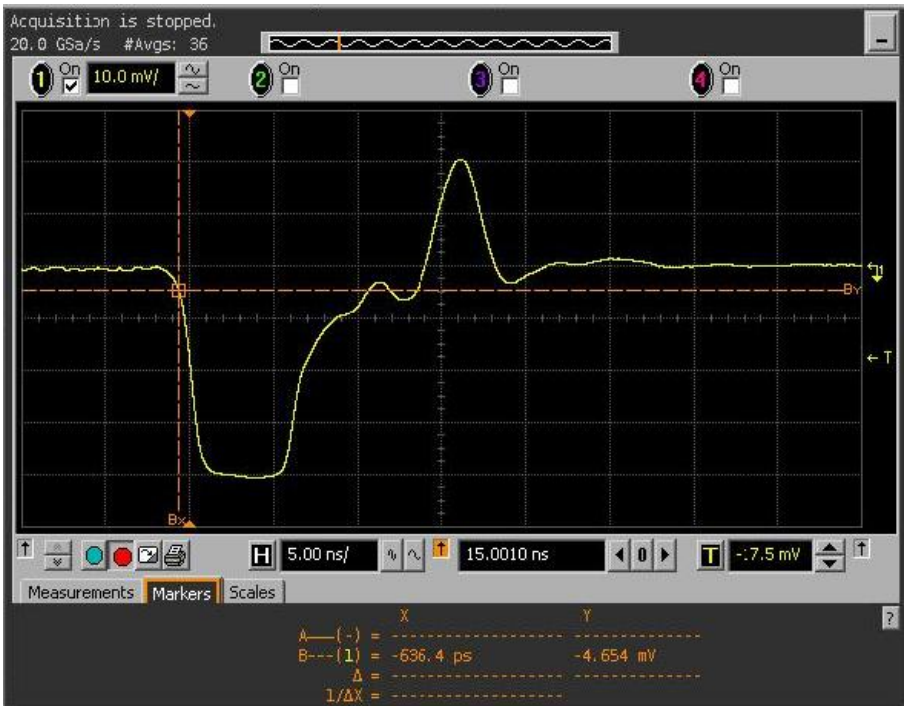

Figure 5-12. Output of gain block from 200 mV signal (courtesy of Fibertek Inc.).

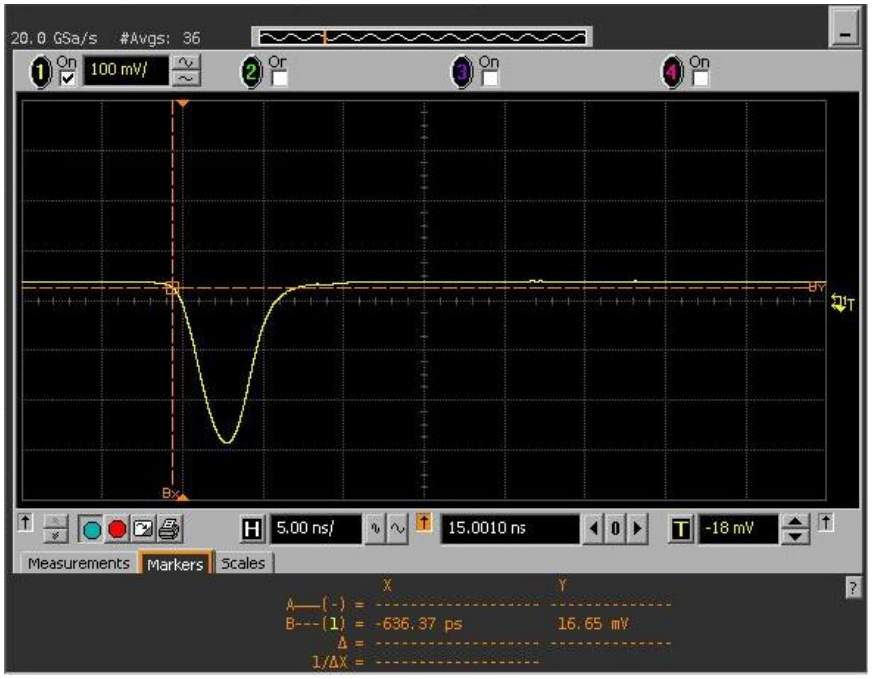

Figure 5-13. Large signal (300 mV) injected into gain block (courtesy of Fibertek Inc.).

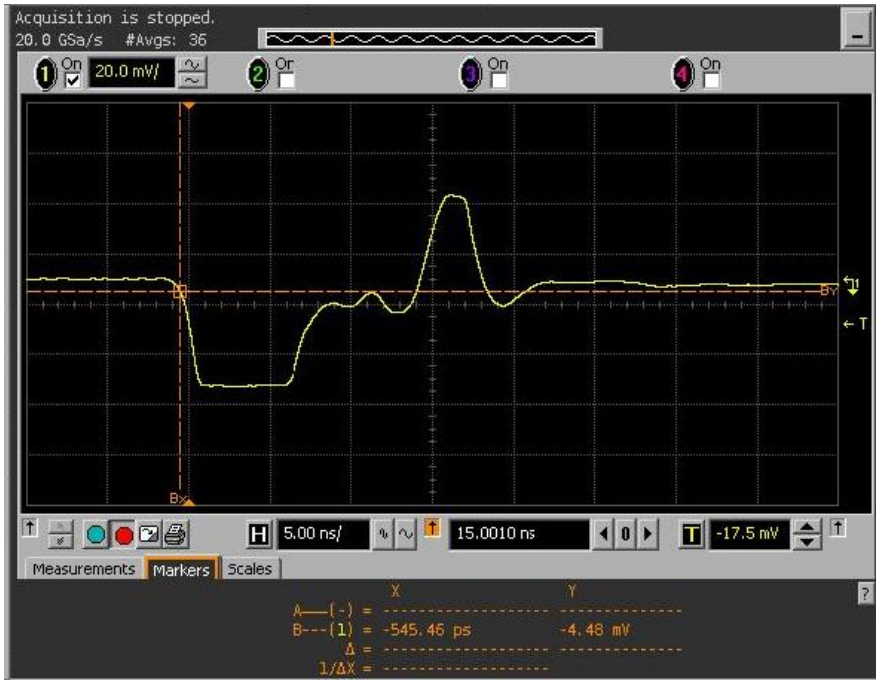

Figure 5-14. Output of gain block from 300 mV signal (courtesy of Fibertek Inc.).

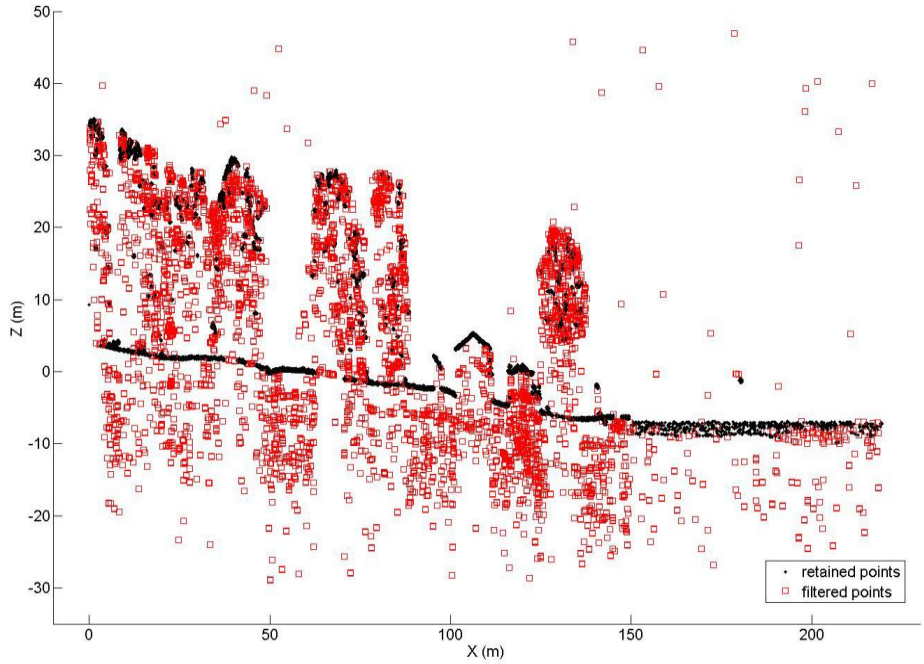

Figure 5-15. Result of first step of MATLAB local density filter for a single channel of raw airborne profile data.

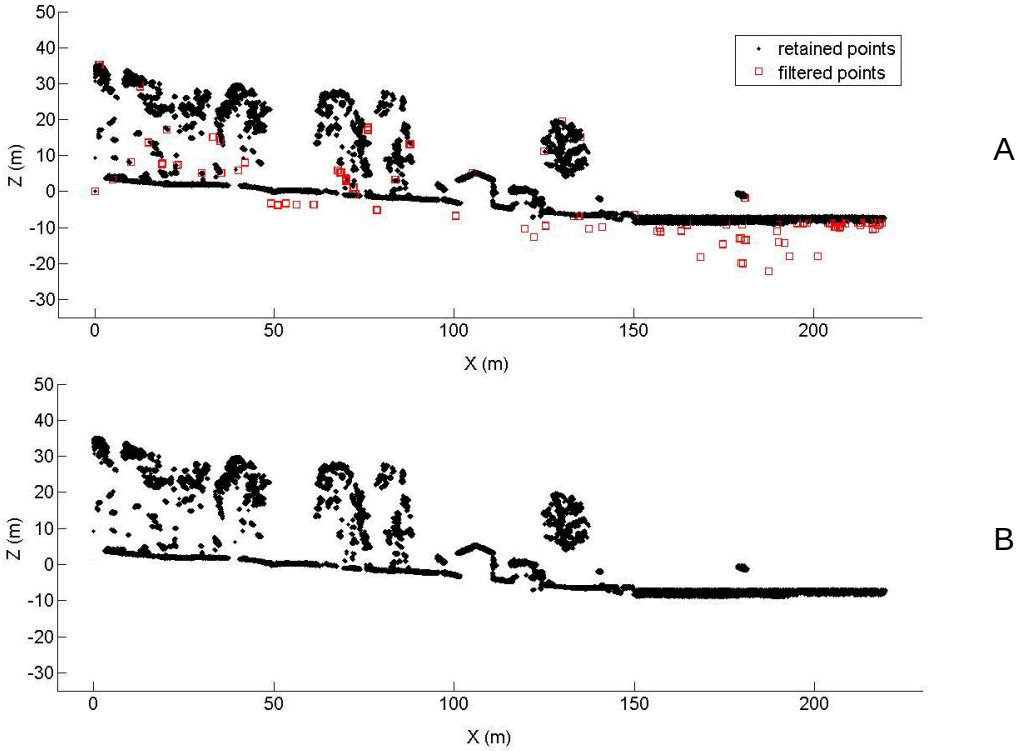

Figure 5-16. Result of second step of MATLAB local density filter for raw airborne profile data. A) Retained and filtered points. B) Retained points only.

A

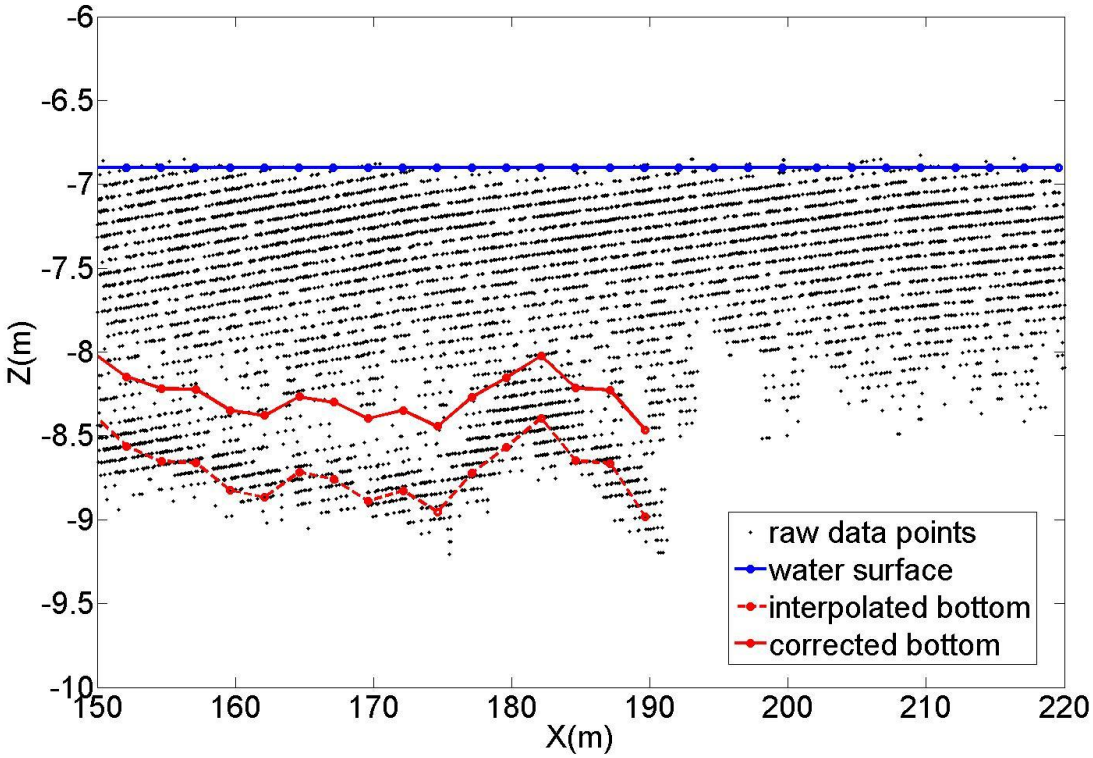

B

Figure 5-17. Flight testing in Mine Run, VA over the Lake of the Woods, southwest. A) Aerial photo near boat docks and shallow launch region with flight line. B) Off-nadir profile, channels 17-32, 2500 V, all returns, processed data depicting fresh water penetration out to 1.65 m.

Table 5-2. Comparison of LIDAR depth estimates and measurements

X (m)	150	160	170	180	190	200
LIDAR Depth Estimate (m)	1.12	1.45	1.49	1.24	1.65	NA
Depth Measurement (m)	1.27	1.52	1.65	1.52	2.03	2.44
Difference (m)	0.15	0.07	0.16	0.28	0.38	NA

A

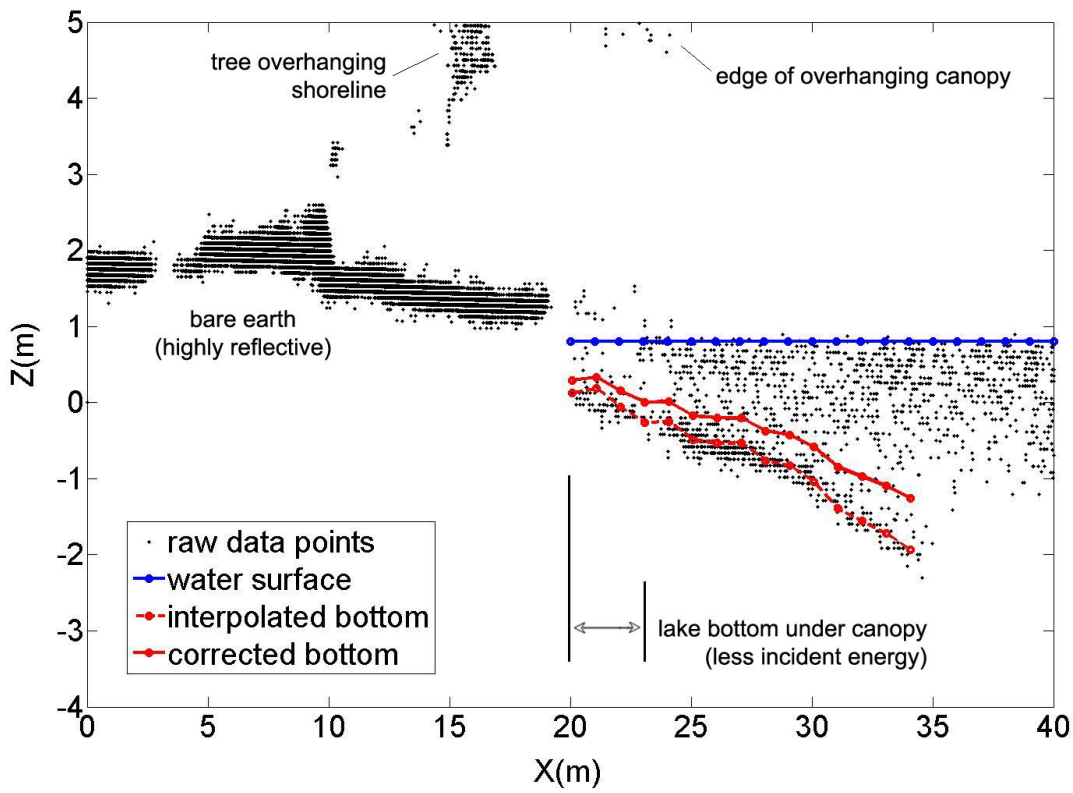

B

Figure 5-18. Flight testing in Mine Run, VA over the Lake of the Woods. northeast. A) Aerial photo near lake shoreline with flight line. B) Off-nadir profile, channels 17-32, 2500 V, all returns, processed data depicting fresh water penetration out to 2 m.

A

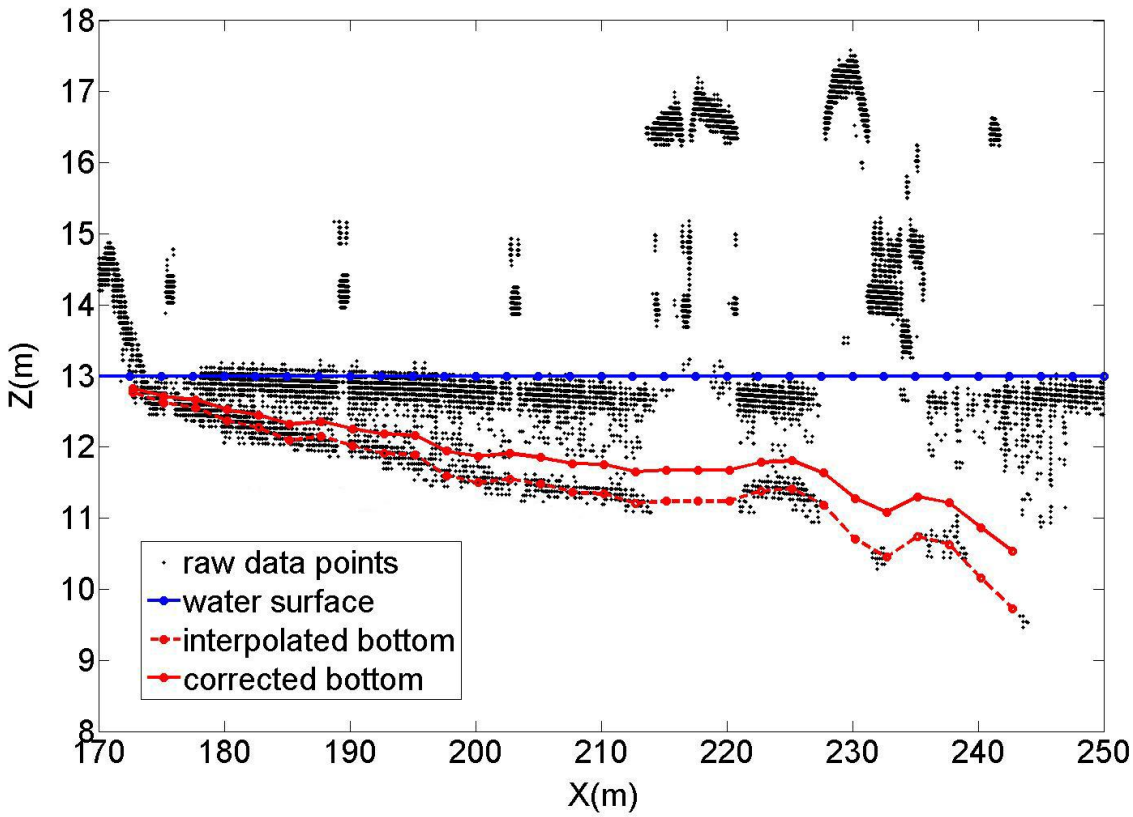

B

Figure 5-19. Flight testing in St. Augustine, FL over docks on the intracoastal waterway. A) Aerial photo near boat docks and shallow launch region with flight line. B) Off-nadir profile, single channel (18), 2500 V, all returns, processed data depicting salt water penetration out to 2.5 m.

Table 5-3. Comparison of LIDAR platform distance estimates and measurements

X (m)	175	189	203	214	236
LIDAR Platform Estimate (m)	1.68	2.13	2.37	2.53	2.90
Platform Measurement (m)	1.82	2.20	2.59	2.74	3.12
Difference (m)	0.14	0.07	0.22	0.21	0.22

A

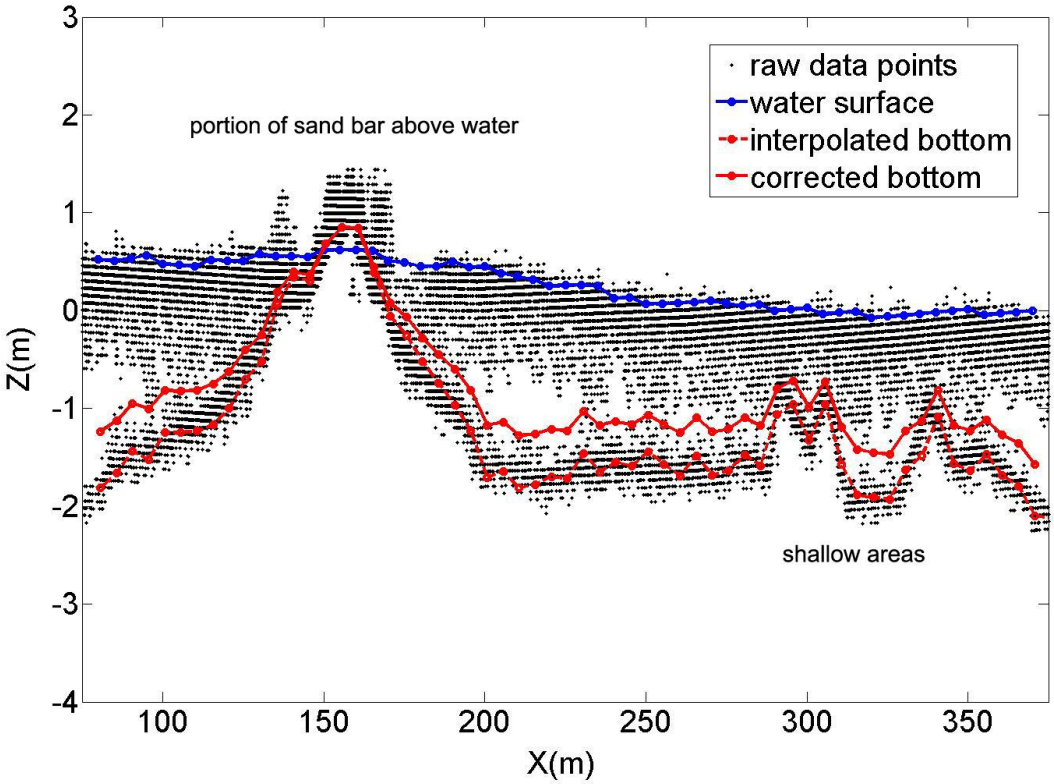

B

Figure 5-20. Flight testing in St. Augustine, FL over a sandbar on the intracoastal waterway. A) Aerial photo over sand bar with flight line. B) Off-nadir profile, channels 21-23, 2500 V, all returns. Point cloud depicting sand bottom out to 1.5 m.

A

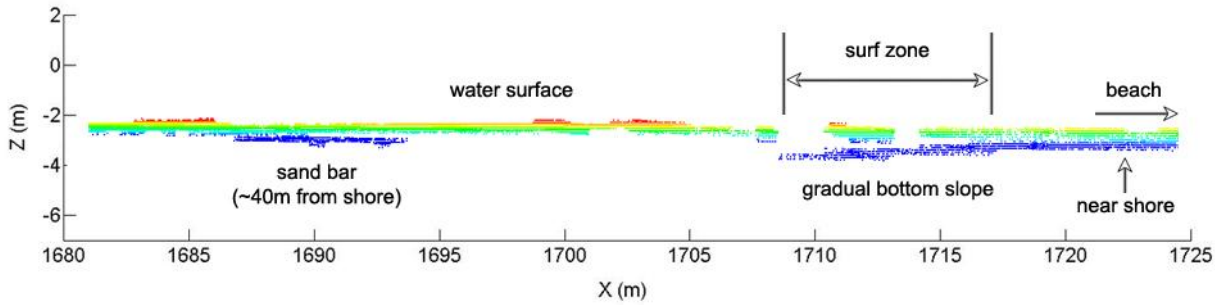

B

Figure 5-21. Flight testing in St. Augustine, FL over the eastern coast. A) Aerial photo of flight path relative to beach. B) Off-nadir profile, 2500 V, channels 21-23, all returns, processed data related to beach / water interface region.

CHAPTER 6
CONCLUSIONS AND FUTURE WORK

Scope of Research

This dissertation has described the essential design elements necessary to construct a low signal-to-noise ratio (LSNR) light detection and ranging (LIDAR) system and assessed the capability of single wavelength, mixed topographic / bathymetric mapping by analyzing the design and testing process of the University of Florida's Coastal Area Tactical-mapping System (CATS).

Design and Testing Overview

Airborne laser swath mapping (ALSM) instruments have conventionally used high energy / high-pulse rate designs. Exploration into alternate detection strategies with the benefit of a highly sensitive detector suggests that detection efficiency can be improved by moving to a LSNR LIDAR paradigm. For example, NASA's Satellite Laser Ranging station (SLR2000) demonstrated the capability of employing passively Q-switched microlasers with output energies of 135 μJ and rates below 5 kHz to achieve millimeter-level ranging precision at satellite altitudes of 20,000 km [23]. Discrimination between signal and noise was achieved by utilizing a range receiver able to identify and extract laser echoes from solar background noise through Poisson statistical analysis of the received photon distribution.

In a very low incident light state, a high gain (10^5) photodetector is able to produce amplified responses due to weak backscattered laser radiation via the photoelectric effect. Individual discrete pulses can be analyzed in a digital mode. If the time resolution of a detector is sufficiently fast that the average time intervals between signal pulses are wide in comparison, then individual incident photons can be "counted" and

the receiver is then capable of “photon counting” (i.e. single photon sensitivity). The generation of a photoelectron in this configuration is a binary event given proper discriminators, making the photon counting method superior to analog signal measurement in terms of detection efficiency and stability.

The power level of incident radiation from signal events may therefore be on the order of the noise, e.g. solar events, reflections off atmospheric particles, and detector thermionic emissions (dark events). Noise events may occur randomly and with low enough frequency to be separated from terrain signals; this has been practically demonstrated by data collected and analyzed by Goddard Space Center in flights of a photon counting laser altimeter, showing clear identification of trees, buildings, and even potential shallow water penetration [23].

An operating wavelength between 500 to 600 nm allows for water penetration due to minimum absorption in this spectral band. In order to estimate the output energy required for single photon detection, signal strength can be estimated as a function of transmitter, receiver, and environment characteristics. Using a modified form of the LIDAR link equation, we can expect 63% chance of signal event registration at a one photoelectron threshold can by transmitting greater than 13.5 nJ pulse energy given the following parameters: a receiver optical efficiency of 0.4, detector quantum efficiency of 0.28, hologram optical efficiency of 0.8, 532 nm wavelength, 0.15 surface reflectivity coefficient (representative of sand), 5º local surface incidence angle, and receiver collecting area of $3.3 \cdot 10^{-3}$ m^2.

The Coastal Area Tactical-mapping System (CATS), the University of Florida’s prototype LSNR mapping system, has provided data essential to exploring the viability

of a multi-element design with these parameters. Improved spatial resolution in single beam scanning LIDAR systems has traditionally been achieved by increasing laser pulse rate to decrease the amount of space between scanned ground footprints. This provides an inherent limitation to avoid the condition of multiple pulses in flight at once; the two-way travel time of electromagnetic radiation at an average flying height of 600 m dictates a maximum pulse rate of 250 kHz. If, however, a single laser beam is split into an array of elements and transmitted at once, spatial resolution improvements are then dictated by the number of array elements and the capability of the receiver to process returns over the array simultaneously. A moderate laser pulse rate can then theoretically provide decimeter-scale resolution.

In the CATS, a passively Q-switched, frequency doubled neodymium-doped yttrium aluminum garnet (Nd:YAG) microchip laser was selected to produce a stable train of pulses. 3.48 μJ per pulse are output at 7.76 kHz. The beam diameter is 0.2 mm with ±2 mrad divergence. Laser light passes through a 10x magnification beam expander, which also decreases the beam divergence to 0.2 mrad. After the beam expander, each pulse is passed through a holographic diffraction element that separates the beam into a 10x10 square array of beamlets rotated 45°, each containing ~35 nJ of energy. Outgoing laser beamlets then pass through shared afocal lenses with a total magnification of 4x. The laser light is deflected through two Risley prisms (V-coated optical wedges with 99.5% light transmission). BK7 material is selected with a refractive index of 1.52, wedge angle of 13.58°, diameter of 88 mm, and central thickness of 22.5 mm. The refractive properties of these elements combined with the wedge surface angle deflect the beam through a predicted path. This allows for the

array of laser beamlets to be arranged in a variety of repeatable patterns. Different types of patterns can provide enhanced coverage for specific applications.

Temporal filtering via a range gate eliminates atmospheric backscatter immediately outside the aircraft and ensures that strongly reflective targets near the output window do not produce a response. Incident radiation passes back through a shared afocal lens. Spatial (2.8 mm field stop) and spectral (0.3 nm bandwidth about 532.1 nm) filters reduce unwanted interference, and the filtered beamlets are rotated 45° by a Dove prism and refocused via a telephoto lens before reaching the MCP-PMT and the associated timing electronics.

Because a very low amount of backscattered radiation is expected from each laser beamlet, a detector must be employed with high enough gain to amplify single photon events. In order to achieve 10^5 gains with 200 ps rise time, 25 ps transit time spread (TTS), and 200 ps dead time specifications, a micro-channel plate photomultiplier tube (MCP-PMT) was selected. This device is capable of simultaneous detection of independent events from a 10x10 pixel array, allowing for two-dimensional resolution. The MCP-PMT provides exceptional gain while maintaining compact size (less than 10 cm^3), immunity to anode saturation, and stability with respect to variations in supply voltage. Varying threshold settings with regards to pulse height distribution plots can provide application-specific versatility.

Ground-based field testing results have yielded 10 cm range accuracy at one standard deviation from the mean and small-scale feature identification at variable scan settings. Building edges, tree structure, bushes and narrow light poles are easily discernable from background noise. GPS time tag information reconciles the position of

the scanner at any given time in relation to the temporal sequence of laser shot in a data set and Risley prism wedge index marks. Analyzing this data allows for study of potential data flow problems, e.g. if the laser fire slaving system happens to miss synchronization pulses, or if the scanner rotation is malfunctioning. An accurate time history with regards to scanning operations aids in point cloud rectification and diagnosis of mechanical errors.

The CATS sensor is capable of recording multiple returns in each channel of the PMT from each laser pulse. Analysis of distributed returns allows for identification of ground reflections under dense foliage and penetration past the water surface. Static experiments were conducted to test LSNR LIDAR performance metrics such as minimum separation distance between multiple scattering objects, water penetration depth for submerged surfaces, and multi- vs. single-photon sensitivity. Discriminating between accumulated histogram waveforms of two separate objects required a separation of 15 cm. An upper limit or “blind zone” for multiple intra-shot returns was thus established.

Varying the PMT sensitivity changed the contrast between noise production and detected signal strength. Atmospheric noise increases significantly on a consistent basis as gain increases toward a single photoelectron threshold (due to solar noise events generally being single photon events). Depending on the reflective properties of targets in the scan area, employing lower gain can decrease the amount of noise throughout the range gate.

The CATS offers the capability to change the PMT supply voltage between experimental collections. Operating at multi-photon sensitivity may have value for

situations in which high ambient noise precludes single-photon sensitivity, as ground-based testing has indicated that man-made objects such as buildings features are easily distinguishable even at lower gain. Airborne data collections at multi-photon sensitivity (2300 V or $2 \cdot 10^5$ gain) are capable of producing responses 3 to 4 bins deep from surfaces such as building roofs, bare earth, and tops of tree canopies. Reducing the tube voltage could help to reduce dynamic range variance. Generally speaking, if interrogated far-field surfaces are of uniform reflectance and the gain of the tube is matched to provide exactly enough amplification to barely produce a threshold crossing, this might be an acceptable technique. It is difficult, however, to estimate target reflectance properties ahead of time, and tailoring a detection strategy to one type of feature negates the real benefit of this type of sensor—mixed mapping. Static testing shows that shallow-water bathymetry is difficult at less than full amplification (2500 V or $8 \cdot 10^5$). For the LSNR detection paradigm to be worthwhile related to submerged surface mapping, an amplification level should be maintained that produces returns from even very weak scatterers.

Another solution has shown significant promise for reducing dynamic range without significantly altering bathymetric responses: changing the type of airborne profiling from on-nadir to off-nadir. By imposing a fixed incidence angle relative to ground for outgoing laser light, the magnitude of the backscattered radiation is decreased due to less significant contributions from specular reflections and increased slant range. This has special relevance in the case of mirror-like water surfaces as large specular components cause problems for shallow bathymetry on-nadir operation.

A circular pattern is one way to propagate this effect throughout a scan and retain contiguous terrain coverage; in fact along-track resolution is effectively doubled.

Simulation has suggested that surface and bottom can be reliably separated in sea water to a depth of 2 m [21]. At larger depths, simulation also suggests that the horizontal resolution of the reconstructed sea bottom is greatly limited by water clarity. Static tests of the CATS sensor show that at a depth of 50 cm in coastal water, on average 12% of shots registered at least one signal event. This was estimated to be a sufficient signal level to produce meter-scale shallow (2 to 5 m depth) bathymetry data at coarse spatial resolution (1 m).

Before reporting on bathymetric statistics from airborne data, contributions from several different noise sources were considered. Two "ghost" images commonly appear after responses from highly reflective surfaces. The first is the largest in amplitude and consistently occurs approximately 12.67 ns beyond the first return of the true surface. The second is approximately half the amplitude of the second, and occurs 24.00 ns later. Three possible sources have been suggested for the ghost images: afterpulsing from gas impurities in the tube envelope, impedance mismatching in PMT cables, and gain block overdrive. The latter was shown to be the most likely cause of the spatially coherent noise due to the dynamic range relation. Reflections from impedance mismatches in transmission line components will be distributed at similar temporal offsets, but their magnitudes are expected to not be significant. Increased levels of random noise after strong input signals suggest contributions from PMT afterpulsing; factory testing should be performed to identify diffused impurity levels.

Though more significant than dark / atmospheric noise, the magnitude of the artifacts was evaluated with regards to local point cloud densities. Because the calculated densities were fairly low (peaks less than 1% of the true signal), we can perform point cloud filtering and expect not to lose a significant amount of signal information about highly reflective surfaces. The result is an affirmation of the temporal coherence idea for LSNR LIDAR expressed by Degnan in 2001 [15]. Even with potentially varied sources of noise producing corruptive data, we can still identify important features via automatic cleaning algorithms.

After post-processing, data from the CATS has largely confirmed bathymetric predictions via airborne profile scans over a fresh water lake in Mine Run, Virginia. The central 16 channels, or 17% of the total footprint area, were sufficient to reconstruct a fresh water lake bottom composed of dark decaying organic / inorganic material (estimated to be highly non-reflective) out to 2 m. Approximately 3.49% of the outgoing laser shots registered a return from the lake bottom. With partial occlusion from an overhanging tree near the lake shore, multiple returns still provided enough information about the submerged surface to fit a gradually decreasing trend line consistent with more highly dense points farther away from shore. An accuracy survey at five near-shore locations yielded 21 cm average error.

In a salt water intracoastal area near St. Augustine, FL, a single channel of information (1% of the total footprint area) was used in profile mode to reconstruct the submerged floor out to 2.5 m depth. The light sand here was estimated to be highly reflective and turbidity near ideal for these types of coastal waters. On average 33.98% of the outgoing shots registered returns from the bottom. An accuracy survey at five

dock platforms yielded 17 cm average error. In the surf zone near the beach, three channels of information (3% of the total footprint area) were able to reconstruct the sea floor in water of optimum clarity out to 2 m depth. Sea surface points in this part of the cloud are sparse, meaning that the local density filter produces voids near the surface in expected white water areas. The sea floor profile underneath these areas is uninterrupted, however, with limited discontinuity near the beach / water interface. On average 13.98% of the outgoing shots register returns from the sea floor.

Future Work

Automatic processing of topographic and bathymetric data can be difficult with high water turbidities and low-reflectivity bottom surfaces. Even with off-nadir operation, and the potential advantages of circular versus raster scanning, CATS data shows that there is still a dynamic range issue because of the large difference in signal strength between topography / sea surface elements and distributed targets such as partially occluded forest canopies and submerged surfaces. For large-scale uniform surfaces such as building roofs, it may be possible to automatically collapse range tails into first returns and simultaneously provide some measure of intensity about the response, dependant on the number of range bins that the signal stretches over and the expected cross-section geometry [24]. Dynamic range is one of the major challenges for adaptive algorithm development [73]; automatic procedures are usually dependent on the local coherence of return information.

It has been shown that gain block overdrive is the most likely cause of ghost images in CATS data. Within the current receiver structure, we may be able add a limiting circuit to ensure that input to the block does not exceed maximum amplifier tolerances. Clipping large signals would result in a higher noise figure, but single-

photon level responses should occur below the -12 dBm level. We should then be able to limit responses to this level and eliminate the ghost effects.

Another proposed method for combating the dynamic range problem is to implement a "sensing" stage to modify signal amplification on a dynamic level. For example, the high voltage in the CATS system is already stepped on a per-shot basis in order to reduce power consumption and extend PMT life. If a separate photodetector were placed in front of the primary MCP-PMT (whether physically or by temporal delay sequencing) such that it were possible to determine the intensity of the backscattered radiation before stepping up the tube high voltage, the level to which the voltage was stepped could be dynamically altered. It would be possible, then, to obtain different amplification for sea surface returns as opposed to sea bottom returns with fairly minimal modification to the current system structure.

The MCP-PMT is already operating at maximum amplification, but if a sensing stage negated the possibility of full amplification during periods of high intensity laser backscatter, it would be possible to fly lower than 500 m and potentially increase the maximum water penetration depth. The 10x10 array output is eye safe down to 100 m altitudes, so the only restricting factor even for populated areas are FAA regulations. Flying lower would also decrease the ground point spacing, providing a denser cloud and discrimination of finer features.

The total power draw for the CATS system is 372 W during profiling and 396 W during scanning. In comparison, the Optech Gemini system power draw is average 560 W and peak 980 W. If a dedicated ASIC or FPGA could be developed to encapsulate system control on a scripted level, the need for a control laptop could be eliminated from

the CATS design. The laptop currently requires 200 W, or approximately half of the total power draw of the entire system. Compensating for this part of the system with a low-power processing unit would move the unit closer to the realm of unmanned air vehicle (UAV) payloads.

The potential for small-feature identification in an airborne scanning capability has been shown in a second-generation system developed by Sigma Space Corporation. A footbridge, gazebo, and street lamps are visible in Fig. 6-1 from flight testing over the U.S. Naval Academy Campus in Annapolis, MD. Design parameters for this system are similar to the CATS design, with the exception of higher (1.5x) output power and faster pulse rate (22 kHz) [81]. A profile section in the Chesapeake Bay is shown in Fig. 6-2 depicting bottom reconstruction out to a depth of 4 m. The maximum depth tolerance in this turbid media (estimated water clarity 14/100) is larger than CATS results in water of higher clarity, meaning that increasing laser pulse energy has significant effect. An interesting result is shown in Fig. 6-3 for a profile over a melt pond in Greenland; here we have some of the best water clarity and bottom reflectivity possible. We can see the frozen lake bottom out to 15 m depth—this suggests potential for LSNR LIDAR in submerged glacial mapping.

Conclusions

We can break down the essential qualities required for a successful ALB system into three general categories: accuracy, capability, and cost effectiveness [70]. For CATS data, comparisons to submerged ground truth in two different environments have shown average error within IHO Order 1 standards (±50 cm at 95% confidence interval) for shallow (<5 m) waters. Seamless mapping at the land/water interface and within the surf zone has been demonstrated, and reconstructions of submerged bottom profiles

were shown for a variety of cases. The potential for larger maximum depth tolerance in more turbid media has been indicated via reference to a second-generation system; this system used slightly higher output energy (50 nJ) and the same detection methodology. The successes with drastically lower output energies (five orders of magnitude less than the traditional mJ-level) suggest that a compact, low-power microlaser and small-form factor MCP-PMT can serve as a basis for potential UAV miniaturization. Elimination of full-waveform digitization, which is commonly found in most modern ALB systems, further supports this approach and also allows for significant cost reduction.

We have arrived at these conclusions by lowering the detection threshold down to the single photoelectron level, allowing the system to record all effective observations without having to resort to an interpretation strategy such as a classic CFD implementation. This has the benefit of avoiding the requisite optical power integration problem normally encountered when working with a large amount of backscattered photons. The natural caveat is increased probability of false positives, but we have shown that spurious noise can be kept to a minimum even at high amplification with appropriate selection of spatial, spectral, and temporal filters.

Using a very short laser pulse width (500 ps) allows for a sufficiently fast timing receiver to differentiate surface and bottom to a small margin (approximately 15 cm accounting for returns in separate range bins). This is not quite zero depth, but for bathymetric mapping beyond 0.5 m it is an acceptable margin. Combining this approach with expansion of the primary beam into an array of sub-beamlets produces ultra-dense point clouds. As a result, even if uncertainty exists in representation of volume backscatter and bottom reflection, geometric patterns can be exploited to aid

classification. This idea was illustrated by eliminating data artifacts in LSNR data associated with large dynamic range based on spatial density coherence. The possibility of exploiting the related detection paradigm has previously been evaluated in only a few developmental systems.

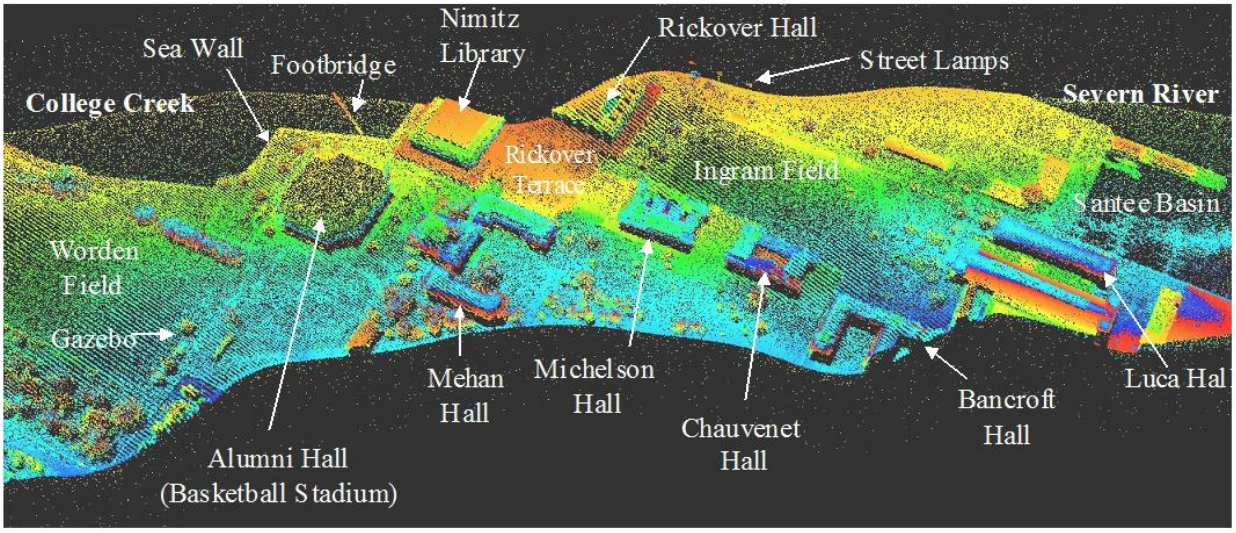

Figure 6-1. Flight testing of second generation LSNR LIDAR by Sigma Space Corporation over US Naval Academy campus in Annapolis, MD [81].

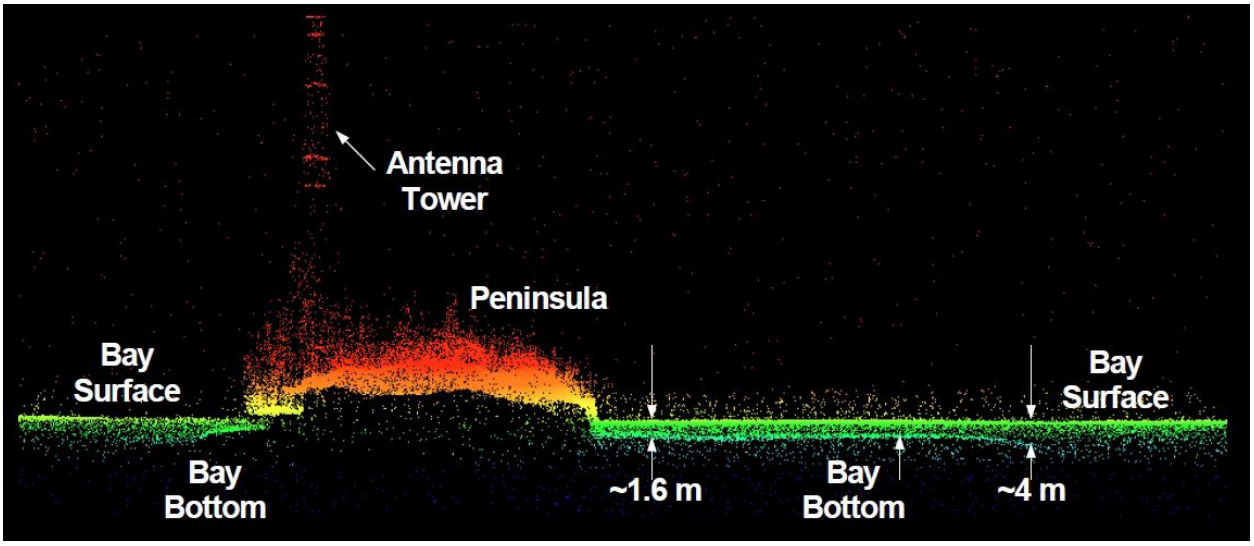

Figure 6-2. Flight testing of second generation LSNR LIDAR by Sigma Space Corporation in Chesapeake Bay off US Naval Academy Campus. Point cloud depicts bay bottom out to approximately 4 m [81].

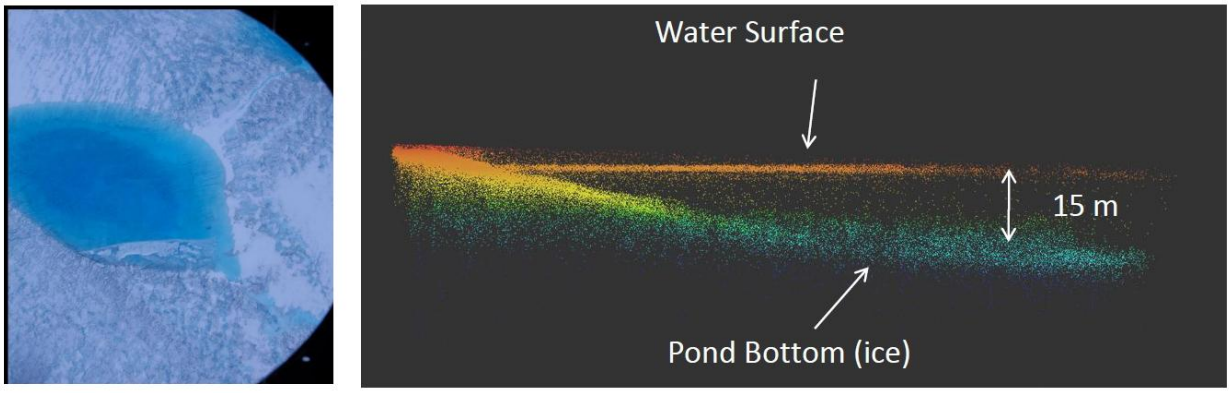

Figure 6-3. Flight testing of second generation LSNR LIDAR by Sigma Space Corporation in Greenland. Point cloud depicts ice bottom penetration out to 15 m [courtesy of Sigma Space Corporation].

APPENDIX A
DATA PROCESSING ELECTRONICS

Ranging Receiver

Gated timing events from 100 "channels" in a 10x10 array are recorded by a multi-stop ranging receiver in the CATS. Signals from the detector elements are processed at several different stages, as dictated by the system controller. Fig. A-1 shows a. receiver block diagram for *n* channels. The four stages are:

- Pre-amplification
- Threshold Detection
- Serial to Parallel Conversion
- Data Capture / Control / Communications Logic

The receiver system detects fixed threshold level crossings from multi-element detector pixels. A narrow pulse received by any one of the detector elements is amplified and low pass filtered. The low pass filter is used to stretch the pulse due to the fact that the input signal pulse width could be of the same order as the sample period of the threshold comparator. Given test data, the bandwidth of the low pass filter has been calculated to achieve greater than 90% counting efficiency for single photoelectron events. The detector has high quantum efficiency and low noise with a bandwidth greater than 1 GHz. The preamplifier is a wide band (DC to 1 GHz) low noise RF gain block that amplifies the detected signal to a level suitable for the processing electronics to operate.

Fig. A-2 shows a data capture board block diagram. After the signal is filtered, it passes through an automatic gain control (AGC) amplifier. The AGC amplifier is used to compensate for the non-uniform response between singular elements across the detector array. AGC amplifier settings are voltage controlled via a digital to analog

converter (DAC). A data capture field programmable gate array (FPGA) stores calibrated data values that are sent to the AGC DAC.

Next, the signal goes to a threshold comparator. DAC channels, associated with the threshold comparators, provide the threshold voltage reference. This voltage reference corresponds to the expected level for a single photoelectron event. The FPGA control logic provides reference point data to the DAC. The output of the threshold comparator is low voltage positive emitter coupled logic (LVPECL).

Serial to parallel conversion changes sequential pulse outputs from the comparator to an 8-bit parallel output at $1/8^{th}$ of the sample clock speed. The operation of this block de-multiplexes sequential photon detection from the threshold comparator and spreads the data out into eight data lines. This provides a relatively low-speed data input for the data-capture FPGA to synchronize to its internal clock and latch the data. Each device receives a separately driven differential clock based on the system clock. A divide by eight clock based on the input clock is an 8-bit word framer to synchronize the parallel data outputs. This clock output is used to latch the 8-bit word into the data-capture FPGA. A reset pin synchronizes multiple devices together. Because each serial to parallel converter requires its own separate clock, the high-speed system clock is buffered with fan-out drivers. In order to sample all the signals at the same time, each of the clock edges must be as close as possible. Programmable delay chips are used for this purpose in order to match propagation delays.

Data management is dictated by a capture FPGA, which performs three main functions: (1) to collect and store data from two serial to parallel converters, (2) send commands to the corresponding DACs associated with each channel, and (3)

communicate with an FPGA dedicated to control logic. Each four-channel section requires the use of two capture FPGAs. A 16-channel board will thus have eight capture FPGAs. These units carry out actions based on instructions from control logic. High level control functions are built into a separate layer to support communication with the system controller. This forms the structure allowing the download of captured data via specific commands.

Event Timer Circuitry

The practical design for implementing the aforementioned theoretical structure can be separated into five sections:

- Back Plane
- Range/control board
- Detector Assembly
- Data Capture boards
- Front Plane

In the CATS, all boards except for the front plane and detector interface board are plugged vertically into the back plane. The back plane accommodates a range/control board, a detector high voltage assembly, and three 32-channel data capture modules. The front plane board lies across and mates perpendicular to the top of the 32-channel data capture modules. The four outer pixels of the 10x10 array are currently not implemented because a 96 channel design was more easily created.

The back plane supports a JTAG data bus shared by the three data capture modules. The JTAG data bus is used for command/control and reading/writing individual channel parameters. A 4-bit differential data bus is used for downloading captured data to the system controller via the range/control board. Each of the data capture assemblies has four sets of 4-bit data bus outputs. For three data capture

modules, 48 data bus lines to the range/control board are therefore supported. In addition, the back plane provides power and clock distribution.

The range/control board has four main functions: (1) to generate a stable high frequency system clock, (2) provide control for the high voltage section of the detector assembly, (3) perform range gate sequences, and (4) support central communications between the data capture assemblies and the system controller. A JTAG link from the system controller interface is used to send command/control information to the range/control board. The command/control section interprets this information.

The T0 pulse circuit is driven by an optical pickup monitoring bleed light from the Nd:YaG laser. The leading edge of each pulse in the train of laser output triggers a sequence of events related to data capture, similar to how the incremental rotation of each optical wedge is triggered. A range gate circuit first delays applying power to the MCP-PMT according to a user set value; this ensures that the outgoing laser pulse is far enough away from the sensor to avoid noise associated with power-up and returns from objects outside the intended return window. Once the gate delay operation is complete, initializations are sent to the data capture boards and detector assembly.

The command / control circuit shown in Fig. A-3 monitors the detector assembly data lines, and issues commands to the data capture boards via the JTAG link when the data lines are ready for transfer. A multiplexor circuit allows for all three boards to be controlled via one control block, and transports return information from the 96 detector elements.

High voltage power supplies are used for detector bias. In order to control the high voltage supplies, the detector assembly has both a DAC and an ADC. A low

voltage reference input to the DAC is used to program the high voltage supplies. The system controller provides the voltage level settings to the range/control board. A corresponding digital value is sent to the DAC located at the detector assembly. The range/control board also reads the detector assembly ADC and uses the data for a voltage level feedback. To maintain detector gain stability, a command circuit incorporates closed loop control using the DAC data as the reference and the ADC data as the feedback value.

For maximum sensitivity (and to prolong detector life) the photon-counting detector is normally off and then gated for data collection. The high voltage is also switched to a lower level between range measurements in order to limit the average current consumption and build-up of heat in the associated electronics. In order for the photon-counting detector's gain to settle, the gate pulse must be sent out prior to the start capture signal. The detector gate pulse is derived from the start capture circuit's coarse counter. A register within the FPGA circuit contains the terminal count that initiates the detector gate pulse. Terminal count values for both the start capture pulse and the detector gate pulse are received from the system controller via a circuit on the range/control board.

Fig. A-4 shows the organization of the receiver components in the processing electronics block assembly. Each data capture board has 16 channels. Two data capture FPGAs and one control FPGA are used for every four-channel section. A 32-channel module has two data capture boards placed back-to-back. An aluminum plate is sandwiched in between these two boards for thermal transfer.

The front plane provides equal path routes for the high-speed detector signals from the detector assembly. Signals from the photon-counting detector are routed via the front plane to each of the 100 data capture channels. The signal routes are 50 Ω matched transmission lines. The individual data capture channels must simultaneously collect all signal outputs from each detector element. The front plane is used to equalize these signal paths among all channels.

FPGA programming is performed over the backplane bus. The data capture and data control FPGAs receive programming information from the master range/control FPGA located on the range/control board. The same source code is uploaded to all of the FPGAs. Individual board variations can be built into the source code and selected using the board select address information. Additional board settings and parameters can be sent over the system JTAG bus after the program has been uploaded. This provides a number of advantages: only one program needs to be maintained, the program resides within the system controller (can be easily changed), and receiver channel boards can be interchangeable without reconfiguration.

These five parts – back plane, range/control board, detector assembly, data capture boards, and front plane – are contained within a cube below the cylindrical motor head shown in Fig. A-5. This cube housing the timing electronics can be decoupled from the optical elements for maintenance and modification.

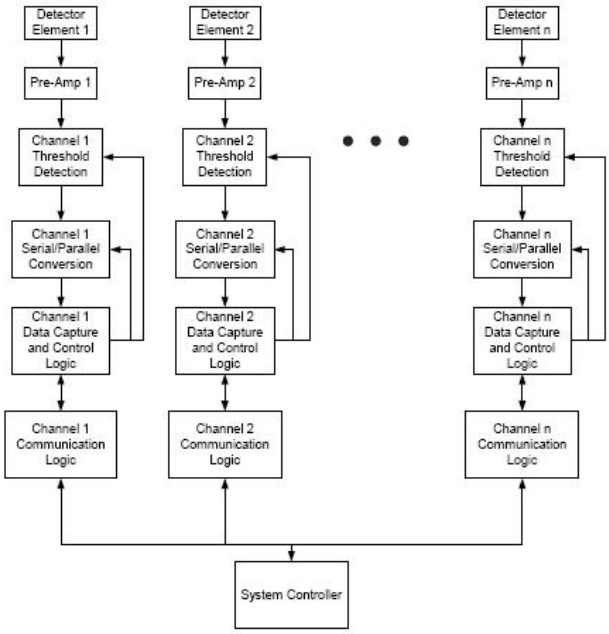

Figure A-1. Receiver block diagram for *n* channels.

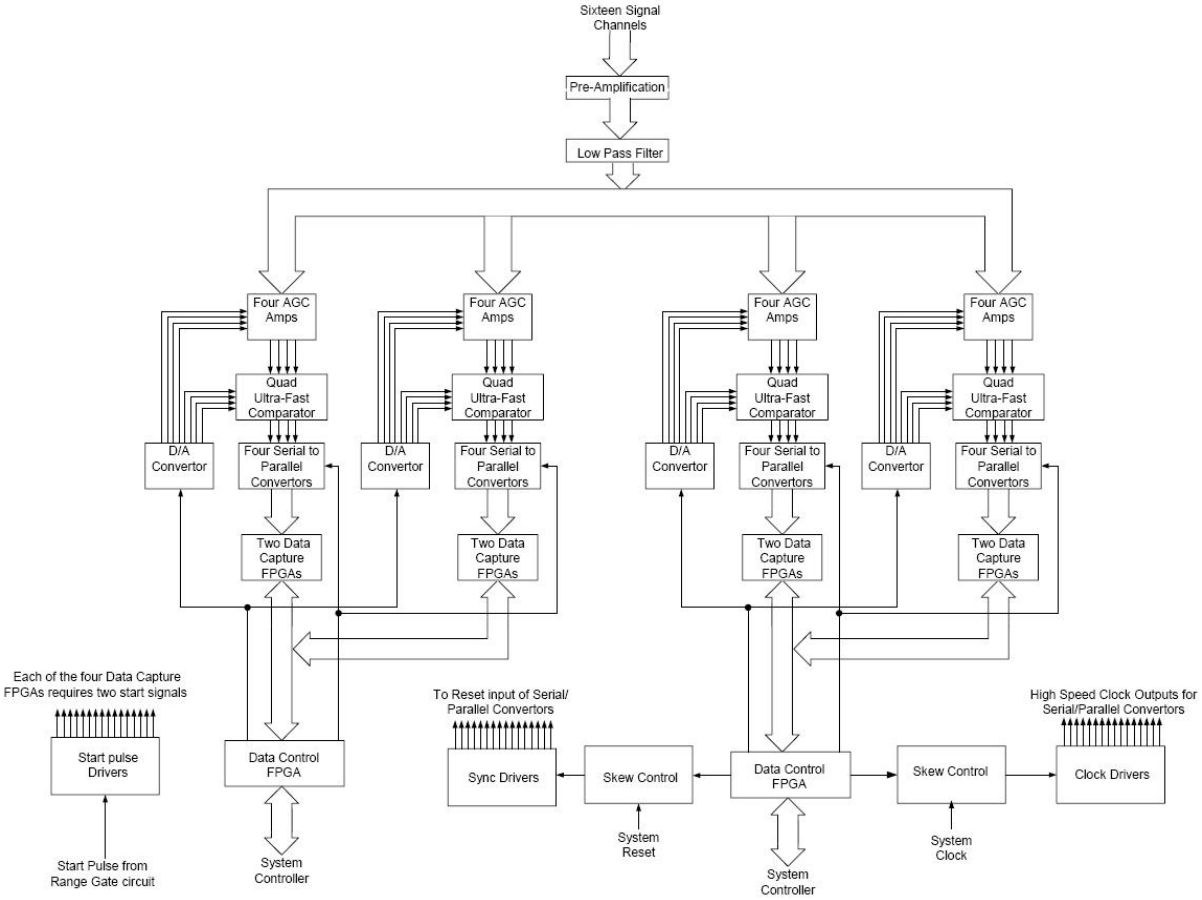

Figure A-2**.** Data capture board block diagram.

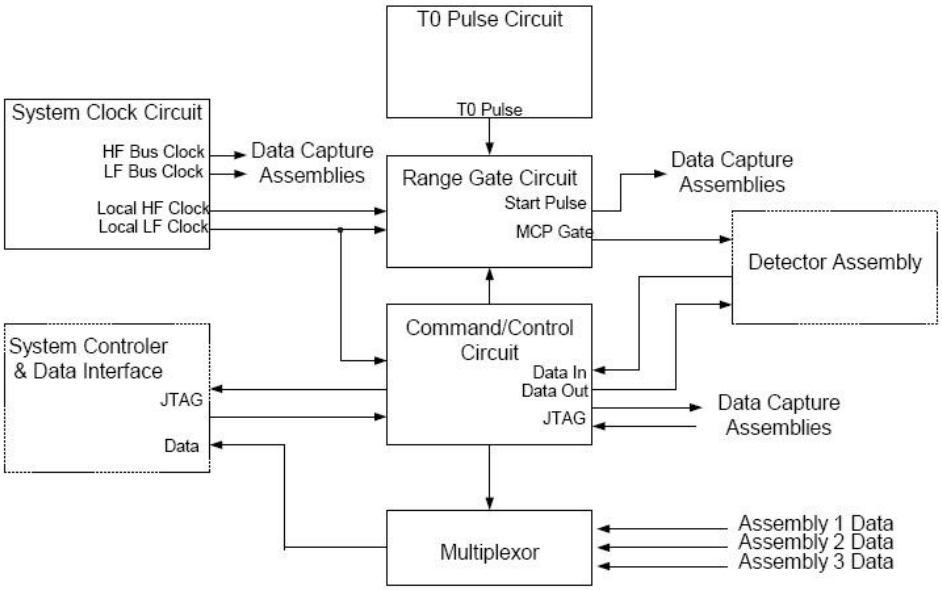

Figure A-3. Range/control board block diagram.

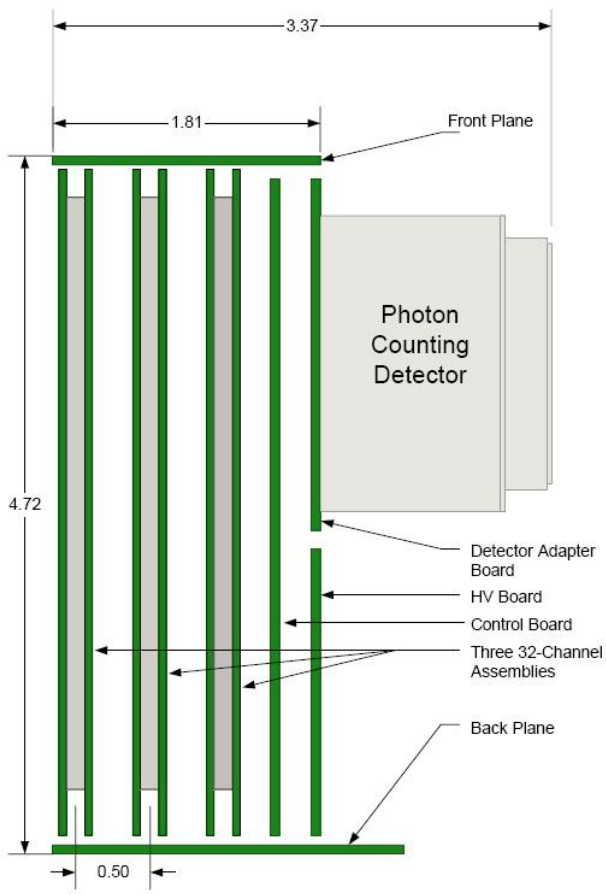

Figure A-4. Receiver components.

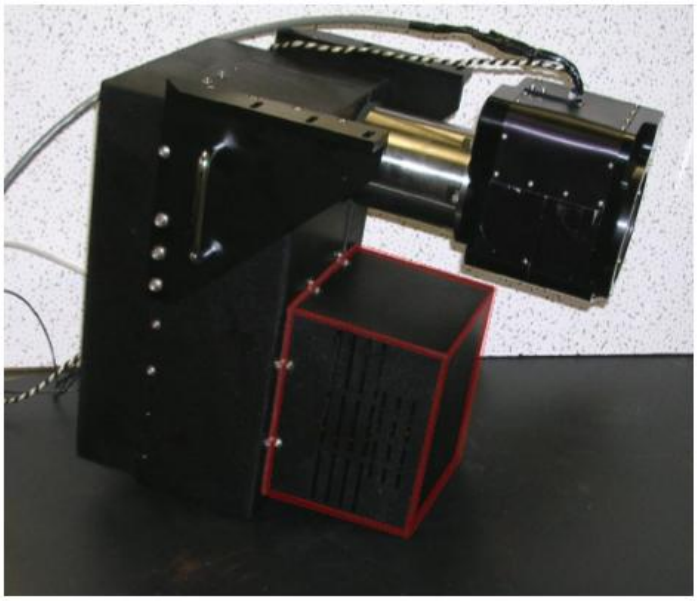

Figure A-5. Assembled CATS system photo with timing electronics “box” outlined in red.

APPENDIX B
SYSTEM TROUBLESHOOTING

Range Offset Error

In early versions of CATS processing software, the RGS value was multiplied by 0.5 ns. This was found to be in error and current versions of code have incorporated the correct value of 1.0 ns. Carrying out the old calculation for a nominal value of RGS=719 would give,

$$\begin{aligned} t_{2-way,error} &= 719 \cdot 0.5 \cdot 10^{-9} + RBN \cdot 0.5 \cdot 10^{-9} \text{ (s)} \\ r_{1-way,error} &= \frac{719 \cdot 0.5 \cdot 10^{-9} + RBN \cdot 0.5 \cdot 10^{-9}}{2} \cdot 3 \cdot 10^{8} \\ &= \frac{719 \cdot 0.5 \cdot 10^{-9}}{2} \cdot 3 \cdot 10^{8} + \frac{RBN \cdot 0.5 \cdot 10^{-9}}{2} \cdot 3 \cdot 10^{8} \\ &= 53.925 + \frac{RBN \cdot 0.5 \cdot 10^{-9}}{2} \cdot 3 \cdot 10^{8} \text{ (m).} \end{aligned} \tag{B-1}$$

With the correct code, however,

$$\begin{aligned} t_{2-way,corr} &= 719 \cdot 1.0 \cdot 10^{-9} + RBN \cdot 0.5 \cdot 10^{-9} \text{ (s)} \\ r_{1-way,corr} &= \frac{719 \cdot 1.0 \cdot 10^{-9} + RBN \cdot 0.5 \cdot 10^{-9}}{2} \cdot 3 \cdot 10^{8} \\ &= \frac{719 \cdot 1.0 \cdot 10^{-9}}{2} \cdot 3 \cdot 10^{8} + \frac{RBN \cdot 0.5 \cdot 10^{-9}}{2} \cdot 3 \cdot 10^{8} \\ &= 107.850 + \frac{RBN \cdot 0.5 \cdot 10^{-9}}{2} \cdot 3 \cdot 10^{8} \text{ (m).} \end{aligned} \tag{B-2}$$

These calculations show that ranges previously used to generate three-dimensional point clouds would be off by a constant value of 107.85 – 53.925 = 53.925 meters. Small errors in coding techniques can produce large-scale errors in range calculation. This leads into the ramifications of local oscillator variation and resulting range bin stability.

Oscillator Variation

The accuracy of range event timing is dictated by the stability of a 2.00 GHz system clock, which is directly related to the RBN recorded in data files. Any significant variation about the central frequency requires modification of the aforementioned equations, and correspondingly modification of data processing software.

This significance of this idea was illustrated during system construction. Concern about the reliability of this main clock was raised after the manufacture of a new control board, which consolidated the function of the external GPS box and eliminated the need for its use. A PLL Control chip (controlled by an FPGA) together with a 1.95-2.15GHz VCO (Z-Comm V610ME04) generates the system clock source of 2.00 GHz.

In the process of finishing the new control board, receiver assembly, and system verification, the clock frequency was discovered to be about 1.90 GHz. The problem source was traced back to the FPGA design, which did not provide an appropriate startup reset. A new control board fixed the problem. It was speculated that the system at some point in the past had the correct clock frequency, but there is no way of knowing at exactly what point in time the skew began. Since the problem was traced back to original design files, however, it is assumed that the problem presides over most of the files collected with the old system.

The old control board at this point in time has not been re-integrated to get a measure of the presumed incorrect frequency. Estimating that the clock reached a minimum value of 1.90 GHz, the Range Bin length would be lengthened to 1 / 1.90 [GHz] = 0.5263 [ns]. Ranges would then be calculated as,

$$r_{1\text{-way}} = \frac{(\mathrm{RGS})\cdot\left(1.1246\cdot 10^{-9}\right)+(\mathrm{RBN})\cdot\left(0.5263^{-9}\right)}{2}\cdot 3\cdot 10^{8}\ (\mathrm{m})\,. \tag{B-3}$$

Processing for previous data collections were altered to accommodate this value. The PLL chip used has since been replaced and verified at 2.00 GHz. It is instructive to note the importance of this central component; any drift over time is difficult to identify in point cloud data without calibration ranging for known distances.

Scan Synchronization

Image Generation: Early Steps

The first attempts to synchronize laser shot time tags to scanner index mark time tags from test data sets exposed some potential errors in both laser and scanner timetag outputs. For example, the consistency of the observed scan periods using the recorded absolute GPS time was checked. To do this, scanner time tags from T000024.STD (a horizontal building scan at 2100 V) were imported into MATLAB.

In this particular file there were 596 entries of scanner index times. This scan was run for 30 seconds, resulting in 30/596 or 0.05034 s per revolution; roughly 19.86 Hz. Observing the rotational period recorded from each scanner wedge, i.e., IndexTime2-IndexTime1, IndexTime3-IndexTime2, etc. produces the plots in Fig. B-1.

Notable in the bottom image are large deviations in what should be a relatively constant period of approximately 20 Hz. The calculated differential times occasionally spike to negative values. Looking at these spikes more closely in the actual data revealed a possible explanation: the microsecond counter not rolling over correctly. For example, consider the raw data from the scanner index times of file T000024.STD at entries 256 to 262, shown in Fig. B-2.

Entry 257 should read 18:38:24.010854, instead of 18:38:23.1010854. There was a problem with the carry flag in the rollover calculation; the GPS seconds eventually were updated correctly from xx:xx:23 → xx:xx:24, but not until entry 261. This counter error explains the large discontinuities in the observed scan period.

Assuming that these spikes were due to this error in time tag production and not an error in scanner motion, the time outputs were filtered to what the maximum range of the scan period should have been for this small interval. During testing it was observed that the laser pulse rate deviated from anywhere between 7800 and 8100 shots/second. Given that the scanner was correctly syncing 400 laser shots to one cycle of revolution, this yields a potential data window of 19.5 to 20.25 Hz,

$$\frac{19.50}{20.25}\,(\mathrm{Hz}) \;\rightarrow\; \frac{0.05128}{0.04938}\,(\mathrm{s}),\ \text{per period}\ . \tag{B-4}$$

The resulting filtered data contains 578 of the 597 total time tag outputs (97% of data retained), so it appears to be a reasonable window of data to look at given that there are around 20 errors in tag generation on rollovers. This filtered data is plotted in Fig. B-3. The images indicate that the scanner working as expected given that the laser fire rate was slightly wandering around 8 kHz.

These observations about scanner index time tags were corroborated by analyzing several more datasets; the motion controller appeared to be working per the design specification. Unfortunately because of problems with shot time tag generation, it was not possible to observe the position of the scanner in relation to successive periods of laser fire unless the laser was assumed to be perfectly slaved to the scanner via the motion control system. Other data collection runs were made without the benefit of time

tag information, however, so several previously developed techniques were employed to try and view the test ranges from that day regardless of accurate timing records.

Point Cloud Results from a Building: Problems

The procedure for creating a point cloud from early CATS test data began by simply plotting the recorded ranges about a 400 shot period. In order to compensate for deviant non-uniform behavior in the receiver channels (i.e. multiple returns in certain channels and zero returns in others) only the per-shot range average was plotted, rather than plotting individual returns from all 96 independent channels. These averages were then staggered across 400 angular intervals a projected relative to a fixed origin. Fig. B-4 (left) shows a top view of a point cloud created from a single horizontal scan line.

The right side of Fig. B-4 shows an image resulting from overlay of 400 shot intervals in a 10,000 shot dataset. The image of the bank building wall is expected to look similar to the image on the left with some deviation about the general structure. The right image, however, shows a cloud that cannot be attributed to excessive noise effects. Possible explanations for the garbled image included dropped synchronization pulses, incorrect prism starting locations, or data overflow issues. The importance of having a diagnostic tool to pinpoint the problem – namely a correctly functioning timetag structure – is evident here.

Shot-By-Shot Analysis of Early Data

Methods for point cloud production resulting in the distorted image assumed that the data was distributed evenly according to a 400-shot period (i.e. shots N to N+399 comprise one scan period). If, however, there happened to be an error in laser sync pulse detection, there would be no correction to shift the period. The resulting data would then have “missing shots” where no shot time tag was recorded. Initial plots of

accumulated 400-shot data indicated that this was a plausible theory given that were problems with the repeatability of the period.

Manual analysis of 400-shot segments identified a repeated set of features, shown in the Fig. B-5(A). This image is a top view of a point cloud generated using average ranges from a single 400-shot window distributed across angular intervals from a fixed origin point. Fig. B-5(B) shows a zoom-in of a pattern contained within a single 400-shot set. When average ranges from three sets of 400-shot increments (blue, red, and green points in the bottom image) are plotted on top of each other as a function of footprint number, they should depict the same geometric features—being that they correspond to multiple repeated scans of the same building face. Fig. B-5(C) illustrates how the geometric patterns for three 400-shot increments did not align, however. From this image, it is likely that the scanner rotation rate was changing significantly across these three data windows.

It was later discovered that the electronics used to detect the synchronization pulses from the laser pulse train and the scanner index marks was not sampling at a high enough rate. As a result, slight deviations in pulse width were causing “dropouts” in pulse detection, which led to such errors as the perceived wandering scan period. These types of hardware malfunctions could have been easily identified with a correctly operating timetag structure.

Data processing operations such as these, however, solidify the importance of the fifth data field – data time tagging – and motivate its further development. Further data collection was put on hold until a new timetag structure was implemented.

Data Time Tagging

Timetag Theory Re-Evaluation

Analysis of scan data had shown that data processing was not able to reliably predict the shot number corresponding to the start of a scan period. It was necessary to re-evaluate the timetag structure. Each individual data collection resulted in the output of four timing files. They were as follows:

- *A.STD*: the time at which the A-scan wedge index mark was detected. This is recorded as a coarse time (seconds) and a fine time (microseconds).
- *B.STD*: the time at which the B-scan wedge index mark was detected. This is recorded as a coarse time (seconds) and a fine time (microseconds).
- *Ranges.SPR*: all relevant ranging information (channel #, range bin, etc.). This file also contains the output value of a 1 MHz microsecond counter which is reset every 100 Hz. This is the only time information individually recorded for every shot.
- *I.STD*: an internal system clock that is updated when a 100 Hz reset signal is fired. This file also contains information about coarse time read from a GPS 1 Hz signal.

It is possible to calculate the timetag of each shot number through combination of a local 1 MHz counter value in the range file and the current time value in the I file. This involved matching the microsecond counter value in the *Ranges.SPR* file to the appropriate time in the *I.STD* file. The resulting shot time tag would be:

$$\begin{aligned} t_{coarse} &= \mathrm{I.STD}_{\mathrm{coarse}} \\ t_{fine} &= \mathrm{I.STD}_{\mathrm{fine}} + \mathrm{Ranges.SPR}_{\mathrm{fine}}. \end{aligned} \tag{B-5}$$

The position in the *I.STD* file is incremented when a 100 Hz reset in the *Ranges.SPR* file is detected. Shot timetags are matched up with either the *A.STD* or *B.STD* times to get the shot corresponding to the start of a scan period (hereon be called shot0). The shot time tag occurring closest to the first A-index time is labeled as shot0.

Problems with Previous Timetag Implementation

A direct comparison to the timetag of the scanner index wedge times should then yield the shot number that corresponds to the start of a scan period. This did not turn out to be true. The point clouds derived from these predicted shot0 had the forescans and backscans mis-aligned, shown in Fig. B-6. Only when shot0 was manually shifted (by anywhere from 20 to 350 shots) was the proper point cloud generated. This procedure is illustrated in Fig. B-7.

A number of issues identified in the individual timing files could have contributed to the difficulties of predicting shot0. A series of data showed that the 100 Hz micro-second counter reset was often missed, causing gaps in the *I.STD* data as well as microsecond counter values in the range data file that exceeded 10000. The microsecond counter must be reset before rolling over to 10000 or an error results. There were also aberrations in the microsecond counter value where the increment from one shot to the next was 2-3 times the normal value (implying dropped shots). Additionally, the number of entries in the *I.STD* data file did not match the number of resets detected from the 1 MHz counter in the range data file. Because of the issues plaguing the I-file and detection of the corresponding 100-Hz signal, this part of the timetag structure was eliminated. Shot timetag operations were moved onboard the FPGA, as described in the next section.

Restructuring of Timetag Generation

The logic for timetag operations was stored onboard a Xilinx FPGA. Index mark timetags were produced as a result of four input pins tied to the following signals: (1) 1 Hz GPS signal, (2) a free running counter based on a local 1 MHz oscillator, (3) A index mark signal, and (4) B index mark signal. The leading edge of a pulse detected on pins

3 or 4 generated an interrupt which latched in data from the stored GPS time (updated every second via a signal on the first pin) plus the current value of the free-running counter. The files *A.STD* and *B.STD* were generated by this process. The I/O is expressed graphically in Fig. B-8(A).

Shot timetags were created by essentially the same method, but using a different fine precision counter. This method used a different 1 MHz local oscillator from inside the main electronics “cube” rather than index mark oscillator, which was found on the controller board itself. The microsecond counter was reset by a 100 Hz internal signal, found in *I.STD*. The value of the counter was matched to the appropriate time in the *I.STD* file to create the shot timetag as previously described.

In reference to the problem of determining shot0, questions were raised about the synchronization between the two different local oscillators. It was theorized that the accuracy of the sync might be related to the throughput capacity of the USB link versus the Ethernet link due to the control loops routing certain signals. High load conditions could produce an offset that would create a disparity producing a calculated shot0 offset. To solve this potential problem, laser fire pulse train was directly input into the FPGA used to tag the index mark signals, shown in Fig. B-8(B). A new output file in the same format as the index mark files was then created to record the shot timetags. This required modification of the FPGA programming and signal routing.

Testing of Timetag Restructuring

The new structure was tested in Fairfax, VA. Data collections with the sensor pointed at a building edge in the distance provided point cloud data with distinct geometries, allowing for characterization of scanner behavior for consecutive 400 shot periods. Timetag files were analyzed to determine shot0 for each data set. Out of 11

data sets, 9 registered the correct value of shot0, allowing for the scan pattern to be correctly rectified in the point cloud.

During system testing to evaluate the new timetag structure, the scanner exhibited some movement errors visible to the eye. For example, during night operation of a static horizontal line scan, the observed output pattern began to slowly rotate such that the pattern eventually became vertical. These rotations did not occur throughout all conducted trials, so a second round of tests was conducted. The same large-scale scanner error was observed, and further post-processing of timing data collected during aberrant scanner behavior showed the B wedge rotational period varying slowly from trial to trial.

It was theorized that a physical malfunction of the B wedge was causing the system to produce inconsistent scan patterns. The system was brought into a laboratory for observations of diagnostic signals on an oscilloscope. The width of the A index pulse was consistent at about 1.5 μs, but the width of the B index pulse fluctuated between 1 and 3 μs. This pointed to a malfunction in the optical encoder associated with the B wedge. Upon opening the sensor head for visual inspection of the encoders, a large crack was found on the B encoder plate. Without timetag processing, this issue may have not been explored for an unacceptable amount of time.

Correctly operating timetags are a significant part of the CATS instrument design. Without accurate knowledge of when the start of a scan occurs, it would be difficult to align recorded return events to scanner behavior without distinct point cloud geometry. Since intended targets for airborne operation are expected to not be ideally symmetric, it is essential that a correct shot0 is calculated. Timetag comparison also allows for the

diagnosis of potential problems with individual system components. For example, laser double pulsing can be identified and corrected via post-processing of event time histories.

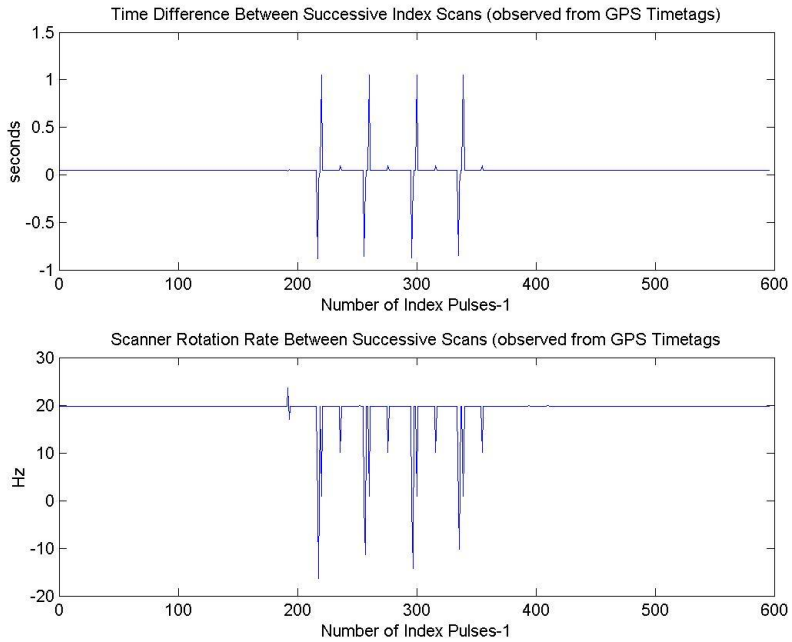

A

B

Figure B-1. Differential measurements of CATS scanner periods. A) Time difference between successive index scans. B) Scanner rotation rate between successive scans. Possible errors in scanner timetags are indicated by large discontinuities.

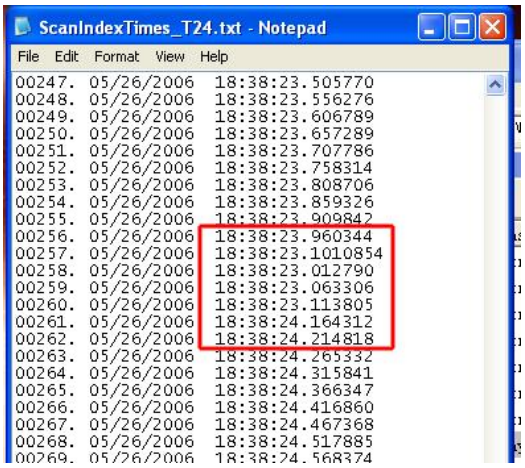

ScanIndexTimes_T24.txt - Notepad

File Edit Format View Help

```
00247. 05/26/2006  18:38:23.505770
00248. 05/26/2006  18:38:23.556276
00249. 05/26/2006  18:38:23.606789
00250. 05/26/2006  18:38:23.657289
00251. 05/26/2006  18:38:23.707786
00252. 05/26/2006  18:38:23.758314
00253. 05/26/2006  18:38:23.808706
00254. 05/26/2006  18:38:23.859326
00255. 05/26/2006  18:38:23.909842
00256. 05/26/2006  18:38:23.960344
00257. 05/26/2006  18:38:23.1010854
00258. 05/26/2006  18:38:23.012790
00259. 05/26/2006  18:38:23.063306
00260. 05/26/2006  18:38:23.113805
00261. 05/26/2006  18:38:24.164312
00262. 05/26/2006  18:38:24.214818
00263. 05/26/2006  18:38:24.265332
00264. 05/26/2006  18:38:24.315841
00265. 05/26/2006  18:38:24.366347
00266. 05/26/2006  18:38:24.416860
00267. 05/26/2006  18:38:24.467368
00268. 05/26/2006  18:38:24.517885
00269. 05/26/2006  18:38:24.568374
```

Figure B-2. Time data file associated with possible scanner timetag errors. A segment of the data is windowed to demonstrate rollover errors in timetag generation.

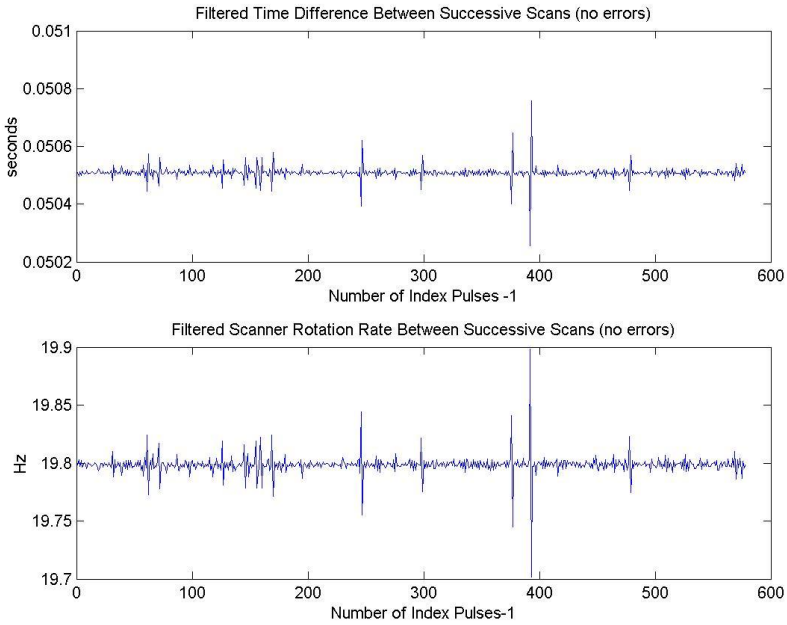

A

B

Figure B-3. Filtered differential measurements of CATS scanner periods. A) Time difference between successive scans. B) Scanner rotation rate between successive scans. The large-scale discontinuities are notably not present, and high-frequency characteristics are consistent with laser repetition rate fluctuation.

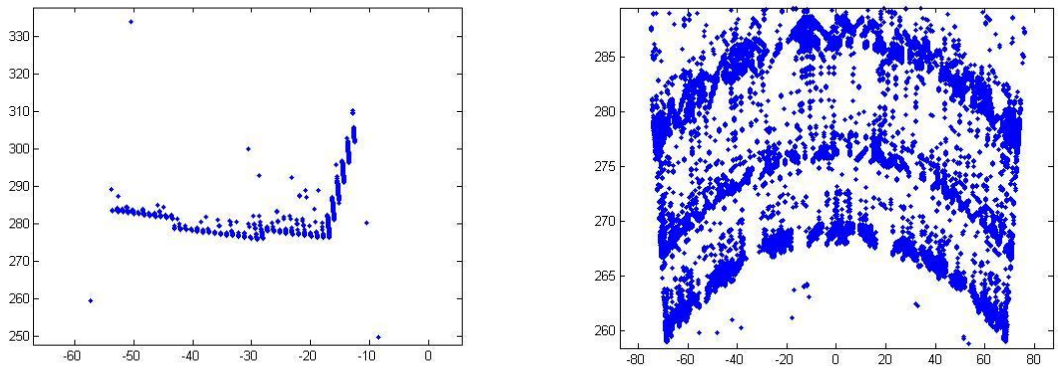

A B

Figure B-4. Point clouds created from preliminary CATS sensor data. A) Top view of a point cloud created from a single horizontal scan line of a bank building face approximately 300 m away. B) Top view of a point cloud created from a horizontal scan of bank building face, resulting from overlay of 400 shot intervals in a 10,000 shot dataset.

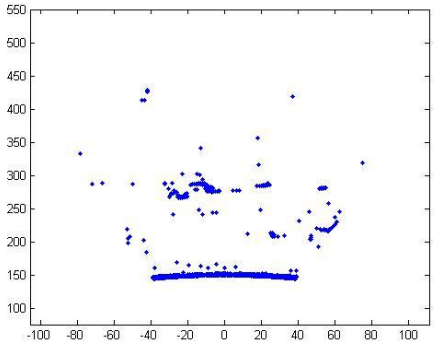

A

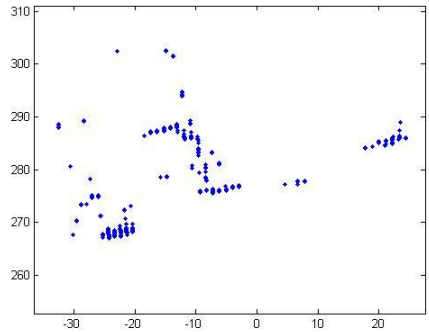

B

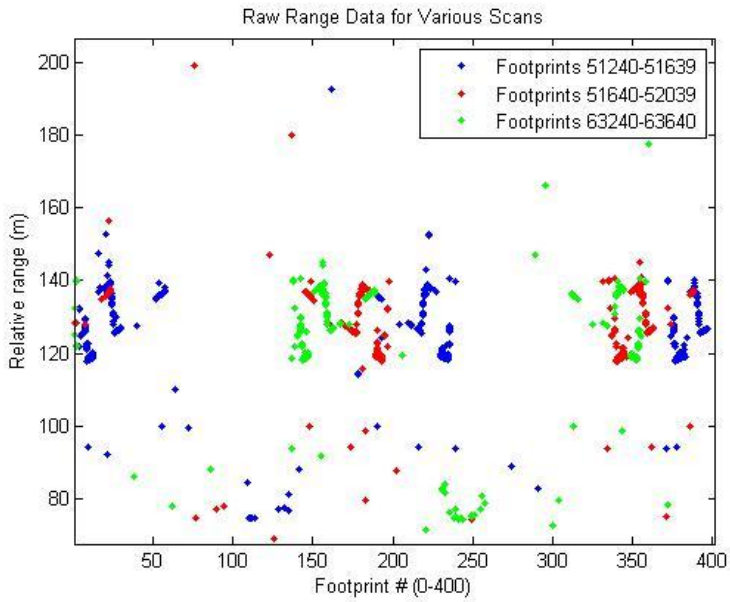

C

Figure B-5. Illustration of scan period wandering. A) Top view of a point cloud generated using average ranges from a single 400-shot window distributed across angular intervals from a fixed origin point. Ranges from one scan period corresponding to 400 laser shots are plotted with constant angular intervals. B) Zoom-in of geometric pattern contained within a 400-shot window. C) Average ranges for three 400-shot windows are plotted on top of each other as a function of footprint number to illustrate wandering scan period.

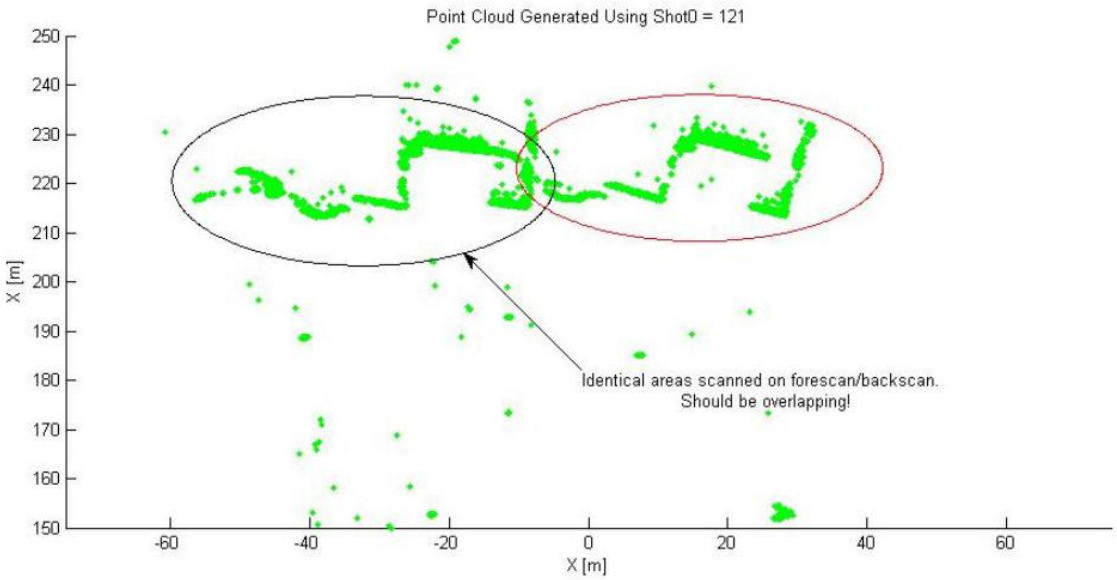

Figure B-6. Point cloud for horizontal profile scan of bank building. Figure was generated using shot0 calculated from GPS timetags. The two highlighted areas represent the same building structure and should overlap, but do not because of the error in shot0 calculation.

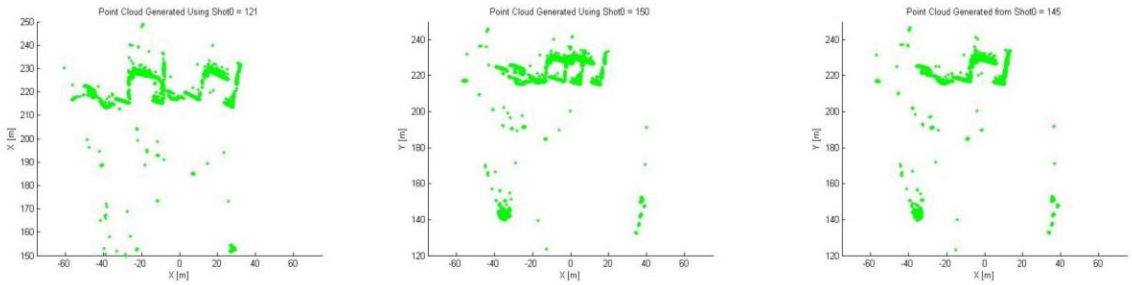

A B C

Figure B-7. Effect of sho0 variation in generated image. As shot0 is varied, the forescan (the image produced from the first 200 shots) and the backscan (the image produced from the last 200 shots) begin to align and merge. The point clouds are generated using predicted shot0 (A), shot0 = 150 (B), and shot0 = 145 (C). 145 is the value of shot0 that results in the best point cloud.

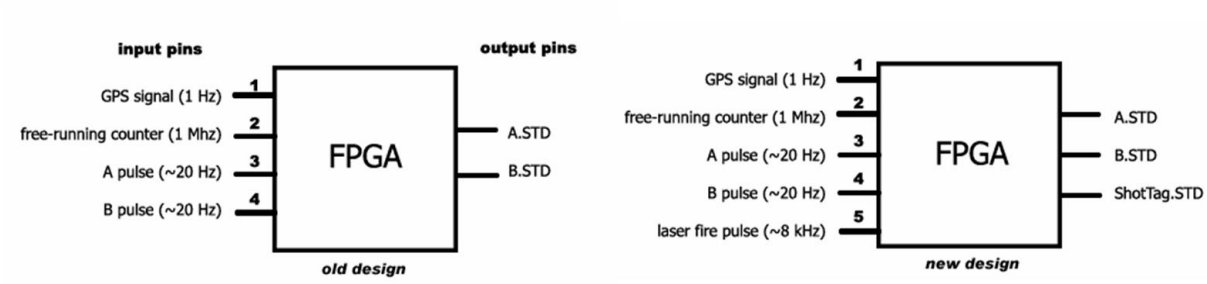

A B

Figure B-8. FPGA block diagram showing redesign of CATS timetag structure to improve calculation of start of scan periods. A) Original structure. B) New structure.

LIST OF REFERENCES

[1] J. B. Campbell, *Introduction to Remote Sensing*, 4th ed.: Taylor and Francis Ltd, 2007.

[2] "The Imaging and Geospatial Information Society," Bethesda, MD: American Society for Photogrammetry and Remote Sensing, 2009.

[3] D. Satale and M. Kulkarni, "LiDAR in Mapping," 2003.

[4] H. Lee, K. Kampa, and K. C. Slatton, "Segmentation of ALSM point data and the prediction of subcanopy sunlight distribution," in *Geoscience and Remote Sensing Symposium, 2005, IGARSS '05 Proceedings, 2005 IEEE International*, p.4, 2005.

[5] B. J. Luzum, K. C. Slatton, and R. L. Shrestha, "Identification and analysis of airborne laser swath mapping data in a novel feature space," *Geoscience and Remote Sensing Letters, IEEE,* vol. 1, pp. 268-271, 2004.

[6] B. J. Luzum, K. C. Slatton, and R. L. Shrestha, "Analysis of spatial and temporal stability of airborne laser swath mapping data in feature space," *Geoscience and Remote Sensing, IEEE Transactions on,* vol. 43, pp. 1403-1420, 2005.

[7] N. Haala and C. Brenner, "Extraction of buildings and trees in urban environments " *ISPRS Journal of Photogrammetry and Remote Sensing,* vol. 54, pp. 130-137, 1999.

[8] Yu, Yang, and Chen, "Automatic feature extraction and stereo image processing with genetic algorithms for LiDAR data," in *International Conference on Computer Graphics, Imaging and Vision: New Trends*, 2005.

[9] A. Alharthy and J. Bethel, "Heuristic Filtering and 3D Feature Extraction From LIDAR Data," in *ISPRS Technical Commission III*, Graz, Austria, 2002.

[10] S. C. Popescu, R. H. Wynne, and J. A. Scrivani, "Fusion of Small-Footprint Lidar and Multispectral Data to Estimate Plot-Level Volume and Biomass in Deciduous and Pine Forest in Virginia, USA," *Forest Science,* vol. 50, 2004.

[11] M. Lee and G. Tuell, "A Technique for Generating Bottom Reflectance Images from SHOALS Data," in *U.S. Hydro 2003 Conference*, Biloxi, MI, 2003.

[12] K. C. Slatton and W. E. Carter, "A Primer for Airborne LIDAR," 2008.

[13] W. Wagner, A. Ullrich., T. Melzer, C. Briese, and K. Kraus, "From single-pulse to full waveform airborne laser scanners: Potential and practical challenges," in *International Society for Photogrammetry and Remote Sensing XXth Congress, Commission 3* Istanbul, Turkey, vol. XXXV, part B3: pp. 6. , July 2004.

[14] R. Gutierrez, A. Neuenschwander, and M.M. Crawford, "Development of Laser Waveform Digitization for Airborne LIDAR Topographic Mapping Instrumentation," in *Geoscience and Remote Sensing Symposium*, IGARSS, 2005.

[15] J. J. Degnan, "Unified Approach to Photon-Counting Microlaser Rangers, Transponders, and Altimeters," *Surveys in Geophysics,* vol. 22, pp. 431-447, 2001.

[16] J. Degnan, "Photon-Counting Multikilohertz Microlaser Altimeters for Airborne and Spaceborne Topographic Measurements," *Journal of Geodynamics (Special Issue on Laser Altimetry),* 2002.

[17] U. Stilla and B. Jutzi, "Waveform analysis for small-footprint pulsed laser systems," in: Shan J, Toth CK (Eds), *Topographic Laser Ranging and Scanning: Principles and Processing*, CRC Press, Boca Raton, pp. 215-234, 2008.

[18] K. Albright, R. C. Smith, C. Ho, S. K. WIlson, J. Bradley, A. Bird, D. E. Casperson, M. Hindman, R. Whitaker, J. Theiler, R. Scarlett, and W. C. Priedhorsky, "RULLI: A Photon Counting Imager," in *International Advanced Studies Institute (IASI) Symposium on Detection and Analysis of Sub-surface Objects and Phenomena*, Monterey, CA, 1998.

[19] B. F. Aull, A. H. Loomis, D. J. Young, R. M. Heinrichs, B. J. Felton, P. J. Daniels, and D. J. Landers, "Geiger-Mode Avalanche Photodiodes for Three-dimensional Imaging," *Lincoln Laboratory Journal,* vol. 12, pp. 383-396, 2000.

[20] J. J. Degnan, R. Machan, E. Leventhal, D. Lawrence, G. Jodor, and C. Field, "Inflight performance of a second generation, photon counting, 3D imaging lidar," *Laser Radar Technology and Applications XIII, Proceedings of SPIE*, vol. 6950, 2008.

[21] T. Cossio, "Prediction of Topographic and Bathymetric Measurement Performance of Airborne Low-SNR Lidar Systems" (Ph.D. dissertation, University of Florida, 2009).

[22] M. Flood, "LIDAR Activities and Research Priorities in the Commercial Sector," in *Land Surface Mapping and Characterization Using Laser Altimetry*, Annapolis, MD, 2001.

[23] J. Degnan, McGarry, Zagwodzki, Dabney, Geiger, Chabot, Steggerda, Marzouk, and Chu, "Design and Performance of an Airborne MultiKilohertz Photon-Counting, Microlaser Altimeter," in *Land Surface Mapping and Characterization Using Laser Altimetry* Annapolis, Maryland, 2001.

[24] P. Cho, H. Anderson, R. Hatch, and P. Ramaswami, "Real-Time 3D Ladar Imaging," *Lincoln Laboratory Journal,* vol. 16, 2006.

[25] O. Svelto, *Principles of Lasers*, 4th ed. (trans. David Hanna), Springer, 1998.

[26] A. Einstein, "On the quantum theory of radiation," *Physikalische Zeitschrift*, vol. 18, issue 121, 1917.

[27] A. E. Seigman, *Lasers*, University Science Books, 1986.

[28] T. H. Maiman, "Stimulated Optical Radiation in Ruby," *Nature*, vol. 187, issue 4736, pp. 493-494, 1960.

[29] G. R. Gould, "The LASER, Light Amplification by Stimulated Emission of Radiation," *The Ann Arbor Conference on Optical Pumping*, June 1959.

[30] W. Koechner, *Solid-state laser engineering*, 2nd ed. Springer Verlag, 1988.

[31] R. Paschotta, "*Q* Factor," *Encyclopedia of Laser Physics and Technology*, RP Photonics, 2003.

[32] F. J. McClung and R. W. Hellwarth, "Giant optical pulsations from ruby," *Journal of Applied Physics*, vol. 33, issue 828, pp. 103-105, 1962.

[33] J. J. Degnan, “Optimization of Passively Q-Switched Lasers," *IEEE Journal of Quantum Electronics*, vol. 31, no. 11, pp. 1890-1901, 1995.

[34] R. Daly and S. D. Sims, "An Improved Method of Mechanical Q-Switching Using Total Internal Reflection," *Applied Optics*, vol. 3, issue 9, pp. 1063-1066, 1964.

[35] A. Szabo and R. A. Stein, "Theory of Giant Pulsing by a Saturable Absorber," *Journal of Applied Physics*, vol. 36, no. 5, May 1965.

[36] J. J. Degnan, "Theory of the optimally coupled Q-switched laser," *IEEE Journal of Quantum Electronics*, vol. 25, pp. 214-220, 1989.

[37] J. J. Zayhowski and P. L. Kelley, "Optimization of Q-switched lasers," *IEEE Journal of Quantum Electronics*, vol. 27, pp. 2220-2225, 1991.

[38] P. Peterson, A. Gavrielides, M. P. Sharma, and T. Erneux, "Dynamics of Passively Q-Switched Microchip Lasers," *IEEE Journal of Quantum Electronics*, vol. 35, no. 8, pp. 1247-1256, August 1999.

[39] J. J. Zayhowski and A. L. Wilson, "Pump-Induced Bleaching of the Saturable Absorber in Short-Pulse Nd:YAG / Cr^{4+}:YAG Passively Q-Switched Microchip Lasers," I*EEE Journal of Quantum Electronics*, vol. 39, no. 12, pp. 1588-1593, December 2003.

[40] ISO Standard 11146, “Lasers and laser-related equipment – Test methods for laser beam widths, divergence angles and beam propagation ratios,” 2005.

[41] Segelstein, Hale, Querry, Wielickza, and Weng, "Absorption Spectra of Water Compendium," 1973, 1981, 1989.

[42] P. B. Russel, T. J. Swissler, and M. P. McCormick, "Methodology for error analysis and simulation of lidar aerosol measurements," *Applied Optics,* vol. 18, pp. 3783-3797, 1979.

[43] Z. Liu, W. Hunt, M. Vaughan, C. Hostetler, M. McGill, K. Powell, D. Winkler, and Y. Hu, "Estimating random errors due to shot noise in backscatter lidar observations," *Applied Optics,* vol. 45, pp. 3783-3797, 2006.

[44] T. Cossio, C. Slatton, W. Carter, K. Shrestha, and D. Harding, “Predicting topographic and bathymetric performance for LSNR airborne lidar,” *IEEE Transactions on Geosciences and Remote Sensing*, Vol. 47, No. 7, Part II, pp. 2298-2315, 2009.

[45] Hamamatsu-Photonics, "Characteristics and use of Si APD (Avalanche Photodiode)," 2004.

[46] Perkin-Elmer, "Avalanche Photodiode: A User Guide. Understanding Avalanche Photodiodes for improving system performance," 2006.

[47] G. C. Guenther, A. G. Cunningham, P. E. LaRocque, and D. J. Reid, "Meeting the Accuracy Challenge in Airborne LIDAR Bathymetry," in *EARSeL-SIG Workshop on LIDAR*, 2000.

[48] R. Nairn, "Royal Australian Navy Laser Airborne Depth Sounder: The first year of operations," in *International Hydro Rev.*, Monaco, 1994.

[49] B. Billard and P. J. Wilsen, "Sea surface and depth detection in the WRELADS airborne depth sounder," *Applied Optics,* pp. 2059-2066, 1986.

[50] Hamamatsu-Photonics, "Photon Counting Using Photomultiplier Tubes," 2001.

[51] Hamamatsu-Photonics, "Photomultiplier Tubes: Basics and Applications." vol. 2, 1999.

[52] H. R. Hertz, "Ueber sehr schnelle electrische Schwingungen," *Annalen der Physik,* vol. 267, 1887.

[53] I. Moreno, "Jones Matrix for Image-Rotation Prisms," *Applied Optics,* vol. 43, pp. 3373-3381, 2004.

[54] R. M. Marino and W. R. Davis, "Jigsaw: A Foliage-Penetrating 3D Imaging Laser Radar System," *Lincoln Laboratory Journal*, Vol. 15, No. 1, 2005.

[55] B. Jutzi and U. Stilla, "Range determination with waveform recording laser systems using a Wiener Filter," *ISPRS Journal of Photogrammetry & Remote Sensing 61*, pp. 95-107, 2006.

[56] K. Y. Shrestha, K. C. Slatton, W. E. Carter, T. K. Cossio, "Performance Metrics for Single-Photon Laser Ranging," *IEEE Geoscience and Remote Sensing Letters*, vol. 7, issue 2, pp. 338-342, 2010.

[57] W. Carter, R. Shrestha., C. Slatton, and W. Dietrich, "Research Quality Airborne Laser Swath Mapping: The Defining Factors," in *A White paper issued by NCALM*, 2007.

[58] Y. Shao, R. W. Silverman, S. R. Cherry, "Evaluation of Hamamatsu R5900 series PMTs for readout of high-resolution scintillation arrays," *Nuclear Instruments and Methods in Physics Research*, A 454, pp. 379-388, 2000.

[59] K. Francis, P. LaRocque, L. Gee, and M. Paton, "Hydrographic Lidar Processing Moves into the Next Dimension," *Proc. of U.S. Hydro*, 2003.

[60] R. W. Pope, P. Johnson, U. Lejdebrink, and J. W. Lilycrop, "Airborne Lidar Hydrography: Vision for Tomorrow," *Proc.*, 2001.

[61] P. E. LaRocque and E. Yang, “Enhancements to the New SHOALS 3000 System,” *International Lidar Mapping Forum*, Denver CO, March 3-5, 2010.

[62] J. M. Wozencraft, “Complete coastal mapping with airborne lidar,” *Oceans 2002 MTS / IEEE*, vol. 2, pp. 1194-1198, 2002.

[63] G. C. Guenther, P. E. LaRocque, and J. W. Lillycrop, "Multiple surface channels in SHOALS airborne lidar," *Proc. SPIE*, vol. 2258, pp. *422-430*, 1994.

[64] S. Pe'eri and W. Philpot, "Increasing the Existence of Very Shallow-Water LIDAR Measurements Using the Red-Channel Waveforms," *IEEE Transactions on Geoscience and Remote Sensing*, vol. 45, no. 5, May, 2007.

[65] A. Collin, P. Archambault, and B. Long, "Mapping the Shallow Water Seabed Habitat With the SHOALS," *IEEE Transactions on Geoscience and Remote Sensing*, vol. 46, no. 10, October 2008.

[66] R. A. O’Neil, L. Buja-Bijunas, and D.M. Rayner, “Field performance of a laser fluorosensor for the detection of oil spills,” *Appl. Opt.*, vol. 19, no. 6, pp. 863–870, Mar., 1980.

[67] M. R. Bristow, D. Nielsen, D. Bundy, and R. Furtek, “Use of water Raman emission to correct airborne laser fluorosensor data for effects of water optical attenuation,” *Appl. Opt.*, vol. 20, no. 17, pp. *2889–2906*, Sep., 1981.

[68] L. W. Harding Jr., E. C. Itsweire, and W. E. Esaias, “Determination of phytoplankton chlorophyll concentrations in the Chesapeake Bay with aircraft remote sensing,” *Remote Sensing of Environment*, vol. 40, issue 2, May, 1992.

[69] G. C. Guenther, "Airborne Laser Hydrography: System Design and Performance Factors," *NOAA Prof. Paper Ser.*, Rockville, MD: NOS, NOAA, March, 1985.

[70] G.C. Guenther, *Digital Elevation Model Technologies and Applications: The DEM Users Manual*, 2nd Edition, D. Maune, ed., American Society for Photogrammetry and Remote Sensing, Chapter 8: Airborne Lidar Bathymetry, pp. 253-320, 2007.

[71] J. C. Brock, C. W. Wright, T. D. Clayton, and A. Nayegandhi, "LIDAR optical rugosity of coral reefs in Biscayne National Park, Florida," *Coral Reefs*, vol. 23, no. 1, April, 2004.

[72] C. Hug, A. Ullrich, and A. Grimm, "Litemapper-5600- A Waveform-Digitizing LIDAR Terrain and Vegetation Mapping System," International Archives of Photogrammetry, Remote Sensing and Spatial Information Sciences, Vol. XXXVVI, part 8/W2, pp. 24-29, 2005.

[73] T. Cossio, C. Slatton, W. Carter, and K. Shrestha, "Predicting small target detection performance of low-SNR airborne lidar," *Journal of Selected Topics in Applied Earth Observations and Remote Sensing* (in press), 2010.

[74] G.A. Morton, H.M. Smith, R. Wasserman, “Afterpulses in Photomultipliers,” *IEEE Trans. Nucl. Sci.*, NS-14, no. 1, pp. 443-448, 1967.

[75] R. Staubert, E. Bohm, K. Hein, K. Sauerland, and J. Trumper, “Possible effects of photomultiplier-afterpulses on scintillation counter measurements,” *Nuclear Instruments and Methods*, vol. 84, issue *2*, April, 1970.

[76] P.B. Coates, “The origins of afterpulses in photomultipliers,” *J. Phys. D: App. Phys*., vol. 6, 1973.

[77] M. P. Bristow, “Suppression of afterpulsing in photomultipliers by gating the photocathode,” *Applied Optics*, vol. 41, no. 24, August, 2002.

[78] Y. Kanaya and H. Akimoto, “Gating a channel photomultiplier with a fast high-voltage switch: reduction of afterpulse rates in a laser-induced fluorescence instrument for measurement of atmospheric OH radical concentrations,” *Applied Optics*, vol. 45, no. 6, February, 2006.

[79] N. Akchurin and H. Kim, “A study on ion initiated photomultiplier afterpulses,” *Nuclear Instruments and Methods in Physics Research*, pp. 121-126, 2007.

[80] H. Johnson and M. Graham, *High-Speed Digital Design– A Handbook of Black Magic*, pp. 160-165, 1993.

[81] J. J. Degnan, "Photon-Counting Lidars for Airborne and Spaceborne Topographic Mapping", *OSA 2010 Optics and Photonics Congress*, Applications of Lasers for Sensing and Free Space Communications (LS&C) Topical Meeting, Paper LSWA4, San Diego, CA, January 31 - February 4, 2010.

BIOGRAPHICAL SKETCH

Kristofer Y. Shrestha was born in Madison, Wisconsin and raised in Gainesville, Florida. He graduated from Eastside High School in 2000 with International Baccalaureate diploma and went on to study electrical engineering at the University of Florida. Kristofer received the Bachelor of Science degree in December 2004, and is currently a Ph.D. student in the department of Civil and Coastal Engineering. He was awarded the Alumni Fellowship in 2005, and now works as a research assistant as a member of the Adaptive Signal Processing Lab under Dr. K. Clint Slatton. He continues to search for improvements in applied science by exploring new technologies.